ISSN en trámite

Geofísica Internacional

Revista Trimestral Publicada por el Instituto de Geofísica de la Universidad Nacional Autónoma de México

México
Volume 61 Number 3
July - September
2022

— Geofísica Internacional —

GEOFÍSICA INTERNACIONAL, Año 61, Vol. 61, Núm. 3, julio - septiembre de 2022 es una publicación trimestral, editada por la Universidad Nacional Autónoma de México, Ciudad Universitaria, Alcaldía Coyoacán, C.P. 04150, Ciudad de México, a través del Instituto de Geofísica, Circuito de la Investigación Científica s/n, Ciudad Universitaria, Alcaldía Coyoacán, C.P. 04150, Ciudad de México, Tel. (55)56 22 41 15. URL: http://revistagi.geofisica.unam.mx, correo electrónico: revistagi@igeofisica.unam.mx. Editora responsable: Andrea Rostan Robledo. Certificado de Reserva de Derechos al uso Exclusivo del Título: 04-2022-081610251200-102, ISSN: en trámite, otorgados por el Instituto Nacional del Derecho de Autor (INDAUTOR). Responsable de la última actualización Saúl Armendáriz Sánchez, Editor Técnico. Fecha de la última modificación: 30 de junio 2022, Circuito de la Investigación Científica s/n, Ciudad Universitaria, Alcaldía Coyoacán, C.P. 04150, Ciudad de México.

Geofísica Internacional
Vol. 61, Núm. 3, julio-septiembre de 2022

Contents

Original paper

https://doi.org/10.22201/igeof.00167169p.2022.61.3.2043

Use of Artificial Neural Networks to predict strong ground motion duration of Interplate and Inslab Mexican Earthquakes for Soft and Firm Soils

R. Flores-Mendoza[1], J. U. Rodríguez-Alcántara[1], A. Pozos-Estrada[1*] and R. Gómez[1]

Received: March 2, 2020; accepted: March 28, 2022; published on-line: July 1, 2022.

Resumen

Se desarrollan modelos de red neuronal artificial para predecir la duración del movimiento fuerte del terreno de eventos de subducción en suelos firme y blando. Para entrenar la red neuronal artificial se emplea una base de datos con un total de 3153 registros sísmicos con dos componentes horizontales para eventos de interplaca e intraslab. El método de componente principal es usado para realizar una reducción dimensional de los parámetros de entrada para desarrollar los modelos de red neuronal artificial. Los valores predichos de la duración del movimiento fuerte del terreno por la red neuronal entrenada son comparados con aquellos estimados con expresiones empíricas. En general, la duración del movimiento fuerte del terreno predicha con la red neuronal artificial sigue la misma tendencia que la calculada con las ecuaciones empíricas, aunque en algunos casos, ésta presenta cambios repentinos en su comportamiento. Por esta razón, es recomendado llevar a cabo varias verificaciones de los modelos entrenados de la red neuronal artificial antes de usarlos para más aplicaciones ingenieriles, por ejemplo, la simulación de registros sintéticos o la evaluación de índices sísmicos de daño.

Palabras Clave: Red neuronal artificial, duración del movimiento fuerte del terreno, eventos de subducción, expresiones empíricas y México.

Editorial responsibility: Arturo Iglesias Mendoza

**Corresponding author at mdiazv@imp.mx*
[1]Instituto de Ingeniería, Universidad Nacional Autónoma de México, Ciudad Universitaria, 04510, Ciudad de México, México.

Abstract

Artificial neural network models are developed to predict strong ground motion duration of subduction events for soft and firm soils. To train the artificial neural network a database with a total of 3153 seismic records with two horizontal components for interplate and inslab earthquakes is employed. The principal component method is used to carry out a dimensionality reduction of the input parameters to develop the artificial neural network models. The predicted values of the strong ground motion duration trained by the artificial neural network models are compared with those estimated with empirical expressions. In general, the strong ground motion duration predicted with the artificial neural networks follows the same tendency of that calculated with the empirical equations, although in some cases, the strong ground motion duration predicted by using the artificial neural network models presents sudden changes in its behavior. For this reason, it is recommended to carry out several verifications of the trained artificial neural network models before using them for further engineering applications, for example the simulation of synthetic records or the evaluation of seismic damage indices.

Key words: Artificial neural network, strong ground motion duration, subduction events, empirical expressions and Mexico.

Introduction

An artificial neural network (ANN) is an effective tool that has been used to solve a great variety of engineering problems due to its flexibility to cope highly nonlinear problems. It is worth mentioning that ANN models as any other prediction technique have advantages and disadvantages (Pande and Shin, 2004). Some advantages of using ANN models include the storage information of the ANN with multidimensional inputs, the prediction of multiple outputs with a single ANN model, the ability to work with incomplete knowledge and machine learning. Perhaps two of the major drawbacks of ANN models are the loss of transparency and the unexpected behavior of the ANN model that may produce erroneous results.

The employ of ANNs in seismic engineering is vast, for example, García *et al.* (2007), used ANNs to estimate peak ground accelerations (PGA) for Mexican subduction earthquakes. Hong *et al.* (2012), employed 39 California earthquakes to predict pseudospectral accelerations (SA) and PGA. More recently, Pozos-Estrada *et al.* (2014) developed ANNs models to predict PGA and SA for Mexican inslab and interplate earthquakes. They showed that the predicted PGA and SA values by the trained ANN models, in general, follow a similar trend to those predicted by ground motion prediction equations (GMPEs). ANNs have also been used to estimate strong ground motion duration (SGMD) of earthquakes. Alcántara *et al.* (2014), developed ANNs to predict SGMD by using information compiled from the Mexican states of Puebla and Oaxaca. The prediction of SGMD has also been applied to other tectonic regions, for example Arjun and Kumar (2011), used ANN models to estimate the SGMD by using Japanese earthquake records, and more recently, Yaghmaei-Sabegh (2018), used a general regression neural network to estimate earthquake ground-motion duration recorded at the Iranian plateau.

The study of SGMD to estimate the structural damage has also been carried out by several researchers (Housner *et al.* 1952; Salmon *et al.*, 1992; Bommer and Martínez, 1999; Strasser and Bommer 2009; and Lindt and Goh, 2004). The general agreement among these studies is that the structural

damage not only depend on the maximum intensity or frequency content of the ground motion, but also on the SGMD. For the estimation of the seismic-induced structural response, the amplitude and frequency content of the ground motions are of paramount importance; however, if the cumulative structural damage or structural degradation of systems with hysteretic behavior is of interest, SGMD should be integrated as design parameter (Reinoso and Ordaz, 2001). More recently, Bhargavi and Raghukanth (2019), carried out a statistical analysis of several ground motion parameters, including SGMD, to rate damage potential of ground motion records.

The main objective of this study is to develop ANN models to estimate SGMD of interplate and inslab ground motion records of Mexican earthquakes from a broad network of stations. Ground motion records from 1985 up to 2017 are employed. Multilayer perceptron ANN models with back-propagation training were considered. The input parameters considered in the development of the ANN models include the moment magnitude (Mw), closest distance to the fault (R_C), focal depth (H), the vibration period of the soil (T), the seismic moment (M_0), as well as the strike (ϕ), dip (δ) and rake (λ) angles. The principal component method is used to carry out a dimensionality reduction of the input parameters to evaluate the ability of ANN models with different number of input parameters to predict the SGMD. The predicted SGMD values by the trained ANN models are compared with those estimated with empirical equations for comparison purposes.

Strong Ground Motion Database and SGMD Calculation

The strong ground motion database employed integrates information from different networks. A total of 3153 strong ground motion records, each one with two horizontal components from 71 earthquakes were used to develop the ANN models. Table 1 and 2 summarize the interplate and in-slab seismic events considered, respectively. The database for interplate includes 50 events with Mw from 5.0 to 8.1, while de database for intermediate-depth normal-faulting inslab events considers 21 with Mw within 5.1 and 7.1. It is noted that the seismic event occurred on September 7, 2017 was not included in the inslab database since it did not cause important damage in Mexico City (Pozos-Estrada *et al.*, 2019) and because the peak ground acceleration registered in Mexico City at lake-bed was below 4 Gal, which was the threshold recommended by Reinoso and Ordaz (2001) as selection criterion of records to calculate SGMD. However, the inslab event occurred on September 19, 2017, which was, together with the interplate event occurred on September 19, 1985, one of the deadliest for Mexico City (Singh *et al.*, 2018, Franke *et al.*, 2019) was included. A map showing the epicenters and recording stations considered is presented in Figure 1. Also in Figure 1, the geotechnical zones (i.e., firm, transition and lakebed) according to the Mexico City design code (2017) are presented. It is worth mentioning that the Mexico City design code (2017) includes rock in the firm soil zone. Figure 2 presents the distribution of Mw, H and M_0 with respect to R_C for the seismic events used.

For the analyses, only two type of soils were considered (soft and firm soil). The transition zone was included in the classification of soft soil on the basis that the dominant period of the soil at such zone is greater than 0.5 s, which is the limiting value used in the Mexican design code to separate firm soil from the rest, and that no evidence that duration is affected by amplification effects on strong ground motion (Singh and Ordaz, 1993). It is worth mentioning that the soft soil of Mexico City consists of lacustrine deposits with saturated clays and sand lenses, the transition soil is composed by alluvial deposits and the firm soil consists of basaltic and andesitic lava, ashes and epiclastic deposits (Marsal and Mazari, 1959; Flores-Estrella *et al.*, 2007). The firm soil of Mexico City can be classified

as class B according to NEHRP Recommended provisions for seismic regulations for new buildings and other structures (2004).

Table 1. Interplate events used in training the ANN models

Event No.	No. of Rec.	Date (dd/mm/yy)	M_w	Lat. °N	Long °W	H (km)	Institution*
1	9	19/09/85	8.1	18.081	102.94	15	CFE-GIEC, II**, IG**
2	22	21/09/85	7.6	18.021	101.48	15	CFE-GIEC, II**, IG**
3	8	29/10/85	5.4	17.583	102.64	20.3	CFE-GIEC, II**, IG**
4	19	30/04/86	7.0	18.024	103.06	20	CFE-GIEC, II**, IG**
5	8	05/05/86	5.5	17.765	102.80	19.9	CFE, II**, IG**
6	60	08/02/88	5.8	17.494	101.16	19.2	CFE, CIRES, FICA, II**, IG**
7	114	25/04/89	6.9	16.603	99.4	19	CFE, CIRES, FICA, II**, IG**
8	112	31/05/90	5.9	17.106	100.89	16	CENAPRED, CIRES, FICA, GIEC, II**, IG**
9	50	01/04/91	5.4	16.044	98.39	25.6	CENAPRED, CIRES, FICA, II**, IG**
10	22	31/03/92	5.1	17.233	101.30	11	CENAPRED, CFE, FICA, II**, IG**
11	74	15/05/93	5.5	16.47	98.72	15	CIRES, II**, IG**
12	200	24/10/93	6.6	16.54	98.98	5	CENAPRED, RIIS, GIEC, CIRES, II**, IG**
13	6	13/11/93	5.4	15.63	99.02	15	CIRES, II**, IG**
14	240	10/12/94	6.3	18.02	101.56	20	CENAPRED, RIIS, GIEC, CIRES, II**, IG**
15	149	14/09/95	7.3	16.31	98.88	22	CENAPRED, CIRES, RIIS, II**, IG**
16	138	09/10/95	7.3	18.74	104.67	5	CENAPRED, CIRES, GIEC, RIIS, II*, IG**
17	55	12/10/95	5.5	19.04	103.70	11	CENAPRED, CIRES, IG**
18	62	25/02/96	6.9	15.83	98.25	5	CENAPRED, CIRES, II**, IG**
19	186	15/07/96	6.5	17.45	101.16	20	CENAPRED, CIRES, GIEC, RIIS, II**, IG**
20	196	11/01/97	6.9	17.9	103.04	16	CPRED, CIRES, GIEC, RIIS, II**, IG**
21	18	21/01/97	5.4	16.44	98.15	18	CENAPRED, CIRES, II**, IG**
22	32	19/07/97	6.3	15.86	98.35	5	CENAPRED, CIRES, II**, IG**
23	18	16/12/97	5.9	15.7	99.04	16	CIRES, II*, IG**
24	22	22/12/97	5.0	17.14	101.24	5	CENAPRED, CIRES, II**, IG**
25	82	03/02/98	6.2	15.69	96.37	33	CENAPRED, CIRES, II**, IG**
26	12	05/07/98	5.0	16.83	100.12	5	CENAPRED, II**, IG**
27	246	30/09/99	7.5	15.95	97.03	16	CENAPRED, CIRES, II**, IG**, RIIS
28	149	09/08/00	6.1	17.99	102.66	16	CIRES, II**, IG**
29	48	08/10/01	5.4	16.94	100.14	10	II**, IG**
30	68	18/04/02	5.4	16.77	101.12	22	CIRES, II*, IG**
31	32	22/01/03	7.5	18.6	104.22	9	II**, IG**
32	67	01/01/04	5.6	17.34	101.42	6	CIRES, II**, IG**
33¥	186	13/04/07	6.3	17.09	100.44	41	CIRES, II**, IG**
34	46	06/11/07	5.6	17.08	100.14	9	II**, IG**
35	74	27/04/09	5.7	16.9	99.58	7	CIRES, II, IG
36	48	09/02/10	5.8	15.9	96.86	37	II, IG
37	124	30/06/10	6.0	16.22	98.03	8	CIRES, II, IG
38	176	20/03/12	7.4	16.251	98.521	16	CIRES, II, UAP, IG
39	162	02/04/12	6.0	16.27	98.47	10	CIRES, II, UAP, IG
40	17	11/04/12	6.4	17.9	103.06	16	CIRES, II, IG
41	48	22/09/12	5.4	16.23	98.30	10	CIRES, II

42	36	22/04/13	5.8	17.87	102.19	10	II
43	60	21/08/13	6.0	16.79	99.56	16	II
44	193	18/04/14	7.2	17.18	101.19	10	CIRES, II
45	190	08/05/14	6.4	17.11	100.87	17	CIRES, II
46	50	10/05/14	6.1	17.16	100.95	12	CIRES, II
47	46	11/10/14	5.6	15.97	95.61	10	II
48	58	23/11/15	5.8	16.86	98.94	10	II
49	78	08/05/16	6.0	16.25	97.98	35	II
50	38	27/06/16	5.7	16.2	97.93	20	II

Notes: * II: Institute of Engineering from UNAM (http://aplicaciones.iingen.unam.mx/AcelerogramasRSM/Consultas/Filtro.aspx); IG: Institute of Geophysics from UNAM (http://www2.ssn.unam.mx:8080/catalogo/); CENAPRED: National Center for Disaster Prevention (http://geografica.cenapred.unam.mx:8080/reporteSismosGobMX/BuscarAcelerograma); CIRES: Instrumentation and Seismic Record Center (http://www.cires.org.mx/racm_historico_es.php); RIIS: Interuniversity Network of Seismic Instrumentation; FICA: ICA Foundation; GIEC: Experimental Engineering and Control Management; UAP: Autonomous University of Puebla. ** Some of the records used were compiled by García (2005) and García et al. (2006). ¥Interplate event according to Franco *et al.*, (2007).

Table 2. Inslab events used in training the ANN models.

Event No.	No. of Rec.	Date (dd/mm/yy)	M_w	Lat. °N	Long. °W	H (km)	Institution*
1¥	10	05/08/93	5.1	17.08	98.53	32	CENAPRED, II**, IG**
2¥	16	23/02/94	5.4	17.82	97.30	5	II**, IG**, CENAPRED
3¥	166	23/05/94	5.6	18.03	100.57	23	CENAPRED, CIRES, RIIS, II**, IG**
4¥	130	10/12/94	6.4	18.02	101.56	20	CIRES, II**, IG**
5¥	124	11/01/97	6.9	17.9	103.00	16	CIRES, II**, IG**
6¥	4	03/04/97	5.1	17.98	98.33	30	II**, IG**
7	144	22/05/97	6.0	18.41	101.81	59	CENAPRED, CIRES, RIIS, II**, IG**
8	38	20/04/98	5.1	18.37	101.21	66	CENAPRED, CIRES, RIIS, II**, IG**
9	254	15/06/99	6.5	18.18	97.51	69	CENAPRED, CIRES, RIIS, II**, IG**
10	172	21/06/99	5.8	17.99	101.72	54	CENAPRED, CIRES, II**, IG**
11	202	13/04/07	6.3	17.37	100.14	42	CIRES, II**, IG**
12	88	12/02/08	6.5	16.35	94.51	87	CIRES, II**, IG**
13	52	22/05/09	5.7	18.13	98.44	45	II**, IG**
14	40	21/07/00	5.4	18.09	98.97	48	II**, IG**
15	80	07/04/11	6.7	17.2	94.34	167	CIRES, II
16	210	11/12/11	6.5	17.89	99.84	58	CIRES, II, UAP
18	156	15/11/12	6.1	18.17	100.52	40	CIRES, II, UAP
19	50	29/07/14	6.4	17.7	95.63	117	CIRES, II
20	148	19/09/17	7.1	18.4	98.72	57	CIRES, II, UAP
21	68	23/09/17	6.1	16.48	94.90	75	CIRES

Notes: * II: Institute of Engineering from UNAM (http://aplicaciones.iingen.unam.mx/AcelerogramasRSM/Consultas/Filtro.aspx); IG: Institute of Geophysics from UNAM (http://www2.ssn.unam.mx:8080/catalogo/); CENAPRED: National Center for Disaster Prevention (http://geografica.cenapred.unam.mx:8080/reporteSismosGobMX/BuscarAcelerograma); CIRES: Instrumentation and Seismic Record Center (http://www.cires.org.mx/racm_historico_es.php); RIIS: Interuniversity Network of Seismic Instrumentation; FICA: ICA Foundation; GIEC: Experimental Engineering and Control Management; UAP: Autonomous University of Puebla. **Some of the records used were compiled by García (2005) and García et al., (2006). ¥Cortical events Lowry *et al.*, (2001).

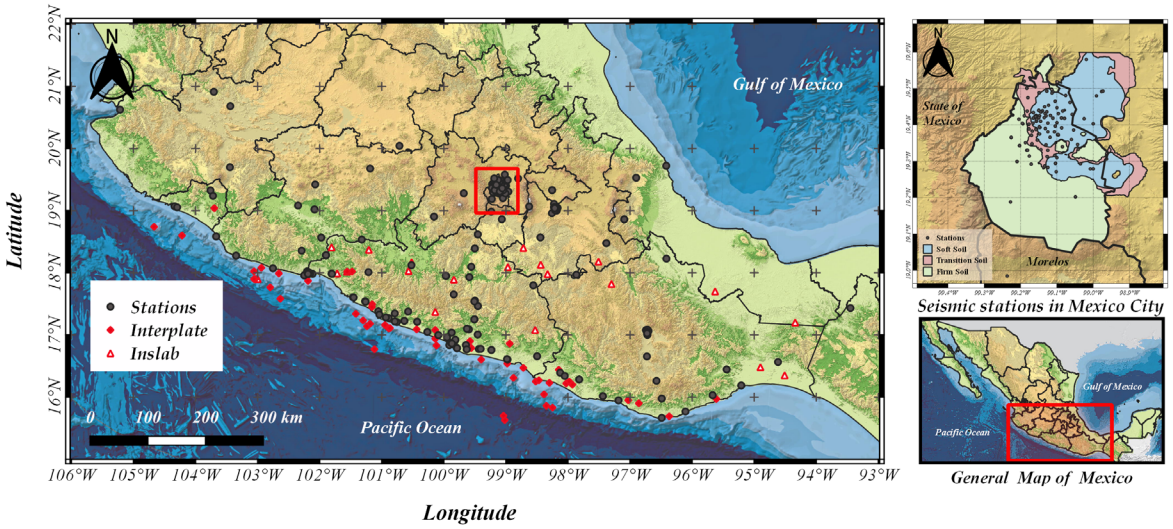

Figure 1. Location of events and recording stations employed.

The total number of records from interplate and inslab events were organized into three groups. The first group corresponds to seismic records registered at soft soil of Mexico City (SS-MC), the second group corresponds to seismic records registered at firm soil of Mexico City (FS-MC), and the third group includes the rest of records registered outside Mexico City at firm soil (i.e., rock) (FS-M). For the development of the ANN models and the empirical equations, a database with all horizontal components of motion without combining them was considered. Figure 3 presents a plot with the percentage of seismic records from interplate and inslab earthquakes used in each group as well as the type of soil. It is observed from Figure 3 that the distribution of records per group is similar between the interplate and inslab earthquakes, and that the records for sites with soft soil in Mexico City have the greatest percentage.

Data Processing

A program was developed in MATLAB (2019), to build a database of seismic records for each type of earthquake. The information considered for each record included the name of the file, station name, station coordinates, magnitude of the event, epicentral coordinates, date and hour of the seismic event, orientation of each sensor channel, peak ground acceleration and maximum seudoacceleration for each component for the soil period, strong ground motion duration and the acceleration values for each component. Bad quality records were discarded. A baseline correction of all the time histories of the records was carried out. Further, for events registered at firm soil (including rock) with Mw >6.5, a high-pass filter with a cut-off frequency of 0.05 Hz was used, for the rest events, a high-pass corner frequency 0.1 Hz was employed. This processing criterion was guided by the work of García *et al.* (2005) and García (2006). For events registered at soft soil, a band-pass filter with corner frequencies from 0.1 to 10 Hz was employed (Jaimes *et al.*, 2015).

SGMD Calculated from the Processed Data

The study of the SGMD has been carried out by several researchers in the past (Trifunac and Brady *et al.*, 1975; Trifunac and Westermo *et al.*, 1982). In this study the SGMD was calculated based on

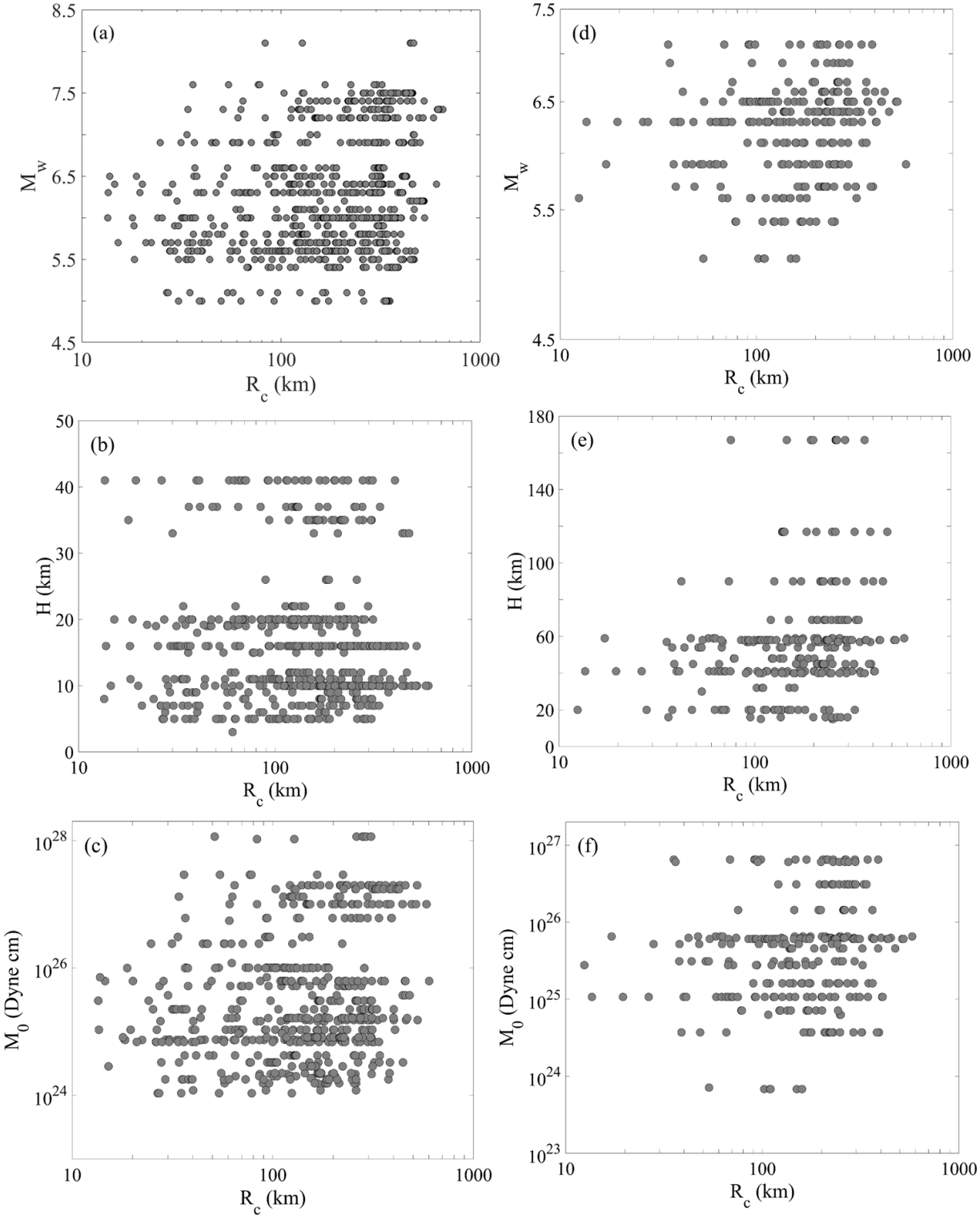

Figure 2. Distribution of Mw, H and M_0 with respect to R_C: (a), (b) and (c) for interplate events; (d), (e) and (f) for inslab events.

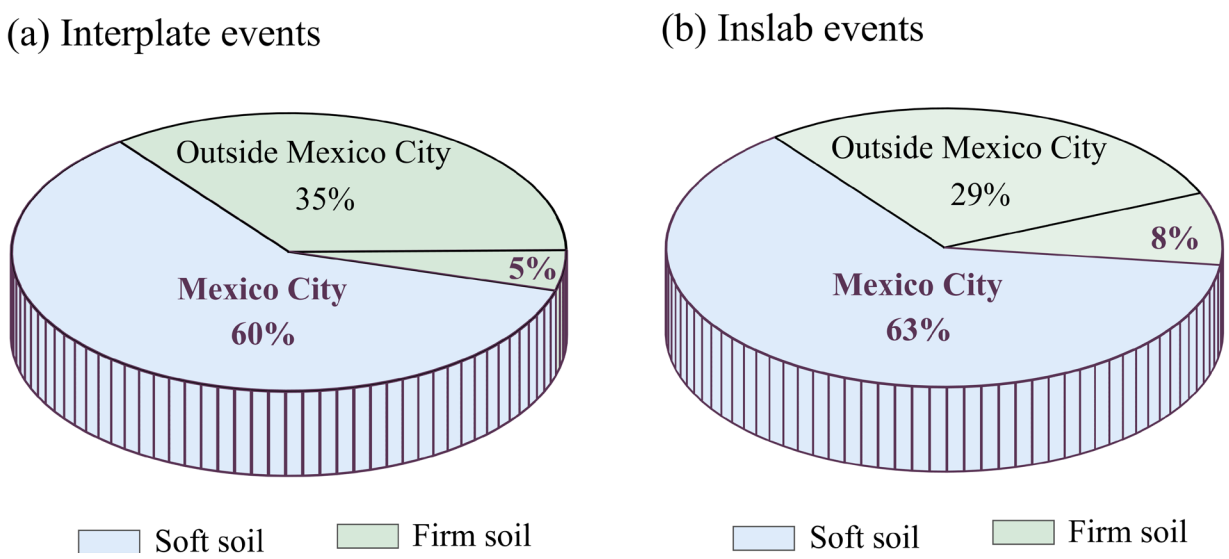

Figure 3. Distribution of percentage of seismic records at soft and firm soils.

the accumulation of energy along time of the strong ground motion records. Arias intensity (Arias, 1970) has been widely used to relate the SGMD with the acceleration time history energy, although it has also been used to study the damage patterns and principal direction of seismic excitations (Arias, 1996; Hong and Goda, 2007; and Hong *et al.*, 2009). In this study the SGMD is assessed based on the Arias intensity, defined as

$$I_A = \frac{2\pi}{g}\int_0^{t_0} a^2(t)\,dt\,, \tag{1}$$

where $a(t)$ is the acceleration time history, t_0 is the total duration of the strong ground motion and g is the acceleration due to gravity. Several procedures have been reported in the literature to determine the SGMD (Bommer and Martínez, 1999), based on lower and upper bounds of duration related to I_A. According to Reinoso and Ordaz (2001), SGMD for Mexican earthquakes can be obtained based on the duration of the strong ground motion between 2.5 and 97.5% of I_A, which is useful for engineering problems. These limits are adopted in the present study, since the records employed in the databases also include most of those used in Reinoso and Ordaz (2001).

Artificial Neural Network Modeling and Training

The ANN architecture with multiple hidden layers and neurons used in this study is shown in Figure 4, where three main layers can be identified: input, hidden and output layer. The flow of information starts from the input layer, this information is weighted to optimize the mapping between the input and the hidden layer(s), and finally transferred it into output value(s). The information transferred from the hidden layer(s) to the output layer is affected by biases that modified the output of the neuron. If an ANN model with a single output neuron and two hidden layers is considered, the mathematical expressions that relate the output neuron in the output layer with the neurons in input and hidden layers are given by,

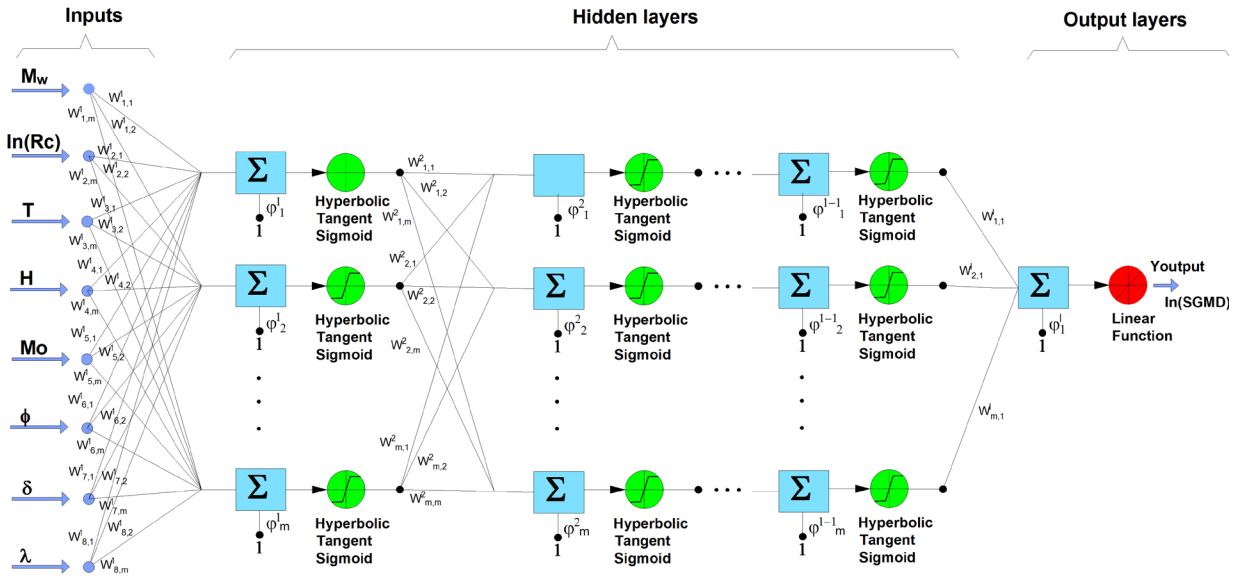

Figure 4. ANN architecture with multiple hidden layers and neurons.

$$y_{output} = f_3\left(\sum_{k=1}^{m}\left[w_3\right]_{k,1} O_{HL1-HL2} + \left(\phi_3\right)_1\right), \tag{2a}$$

$$O_{HL1-HL2} = f_2\left(\sum_{j=1}^{m}\left(\left[w_2\right]_{j,k} O_{HL1-HL2} + \left(\phi_2\right)_k\right)\right), \tag{2b}$$

$$O_{IL-HL1} = f_1\left(\sum_{i=1}^{n}\left(\left[w_1\right]_{i,j} x_i + \left(\phi_1\right)_j\right)\right), \tag{2c}$$

where y_{output} is the value of the output neuron, $O_{IL\text{-}HL1}$ is the outcome obtained when the information given in the input layer has passed through the first hidden layer, $O_{HL1\text{-}HL2}$ is the outcome obtained when the information from the first hidden layer has passed through the second hidden layer, m is the total number of neurons in the hidden layers, n is the total number of neurons in the input layer, $f_1(\,)$, $f_2(\,)$ and $f_3(\,)$ are activation functions between the input and the first hidden layer, the first and the second hidden layer and between the second hidden layer and the output layer, respectively; $[w_1]_{i,j}$, $[w_2]_{j,k}$ and $[w_3]_{k,1}$ are the weights that map the information between the input and the first hidden layer, between the first and second hidden layer and between the second hidden layer and output layer, respectively; $(\phi_1)_j$, $(\phi_2)_k$ and $(\phi_3)_1$ are the biases associated with the hidden and output layers and x_i is the i-th neuron in the input layer.

The optimization of the weights and biases of the ANN model is carried out during the training process. Although a variety of algorithms is available in the literature (Swingler, 1996; Principe and Euliano, 1999; and Haykin, 1999), the back-propagation algorithm (Rumelhart *et al.*, 1986) is one of the most popular. The back-propagation algorithm employs a predefined error function, which is minimized to evaluate the weights and biases. The back-propagation algorithm is adopted in the present study to train the ANN models. Aside from the back-propagation algorithm, in the last

decade the constant improvement of Machine Learning techniques has allowed the development of deep learning that employs the deep neural network. The use of deep neural networks has gained much attention due to their ability to solve complex problems. The use of deep neural networks is outside of the scope of the present study.

Estimation of Strong Ground Motion Duration Using Ann

Application of Principal Component Analysis to Identify the Inputs of the ANNs Models

Dimensionality reduction methods have been widely used to reduce the number of input parameters to develop ANN models (Yuce *et al.*, 2014). One of the classical dimensionality reduction methods is the principal component analysis (PCA), which transforms a set of observations of correlated variables into a set of principal components, which are linearly uncorrelated. Based on the identified principal components, the amount of total variance contributed by each component is assed to select a reduced number of principal components which cumulative variance is within predefined acceptable values. Once a reduced number of principal components is selected, the relative importance of each input parameter to a particular component is evaluated by using correlation coefficients that relate the reduced set of principal components and input parameters. The reduced number of input parameters is selected based on predefined thresholds of correlation coefficients.

To illustrate the use of PCA in the dimensionality reduction of the input neurons for the development of the ANN models, we use the data for inslab events for firm soil for places outside Mexico. To proceed with the calculation of the principal components, the correlation coefficient matrix between the input variables is given in Table 3.

The correlation coefficient matrix is then decomposed by using the singular value decomposition to calculate the amount of total variance contributed by each principal component. Table 4 summarizes the percentage of variance associated with each principal component and its corresponding eigenvalue.

It is noted that there are different criteria to select the reduced number of principal components. According to Lovric (2011), the reduced number of principal components can be selected when they account for a cumulative variance within 70 to 90%. A simpler criterion, which is adopted in this study, is to select those principal components whose eigenvalues are greater than one. Based on the afore-mentioned criterion, from Table 4, the reduced number of principal components is equal to 4.

Table 3. Correlation coefficient matrix for input variables for inslab events for firm soil for places outside Mexico.

	$\mathbf{R_C}$	$\mathbf{M_w}$	**T**	**H**	$\mathbf{M_0}$	ϕ	δ	λ
R_C	1	0.220	0.347	0.242	0.124	0.215	-0.028	-0.101
M_w	0.220	1	0.087	0.397	0.659	0.123	0.384	-0.002
T	0.347	0.087	1	0.119	0.033	0.099	-0.056	-0.015
H	0.242	0.397	0.119	1	0.046	0.457	0.200	-0.284
M_0	0.124	0.659	0.033	0.046	1	0.160	0.124	-0.210
ϕ	0.215	0.123	0.099	0.457	0.160	1	-0.308	-0.053
δ	-0.028	0.384	-0.056	0.200	0.124	-0.308	1	0.326
λ	-0.101	-0.002	-0.015	-0.284	-0.210	-0.053	0.326	1

Table 4. Percentage of variance associated with each principal component and its corresponding eigenvalue.

Principal component	**1**	**2**	**3**	**4**	**5**	**6**	**7**	**8**
Eigenvalue	2.24	1.64	1.19	1.03	0.87	0.63	0.29	0.11
Variance (%)	27.99	20.46	14.84	12.90	10.89	7.82	3.66	1.41
Cumulative variance (%)	27.99	48.46	63.30	76.20	87.10	94.92	98.59	100

By using the first 4 principal components, the correlation coefficients that relate the reduced set of principal components and input parameters is presented in Table 5.

It is observed in Table 5 that there are considerable variation in the correlation coefficients. To identify the reduced input parameters, we use two thresholds of correlation coefficients (Moore *et al.*, 2013), the first one equals 0.7 and the second one equals 0.55. It is noted that strong relation between variables is associated with correlation coefficients greater than 0.7, while moderate relation is associated with correlation coefficients greater than 0.55. Table 6 presents the reduced number of input parameters when the correlation thresholds are adopted. Also in Table 6, the reduced number of input parameters for the rest of the database are summarized. It is observed from Table 6 that the number of input parameters with strong correlation for interplate events ranges from 2 to 3, while for inslab it varies from 2 to 6. For the input parameters with strong correlation, the greater number of input parameters are related to the SS-MC case. If moderate correlation is considered, the number of input parameters is within 6 to 7 and 5 to 7 for interplate and inslab events, respectively. Based on the PCA results, ANN models are developed by using the identified input parameters based on the type of relation (i.e., strong and moderate relation). Furthermore, for the sake of comparison, ANN models by using the complete set of input parameters, referred to as 'all inputs', was included. One more ANN model with predefined input parameters is considered, this model includes Mw, natural logarithmic of R_c, H and T as input neurons and is referred to as 'original case'. This last ANN model is considered as much of the information available in applications of engineering include those parameters. It should be pointed out that all the ANN models employ the natural logarithmic of R_C instead of the R_C. The output layer of the ANN models consists of a single neuron that represents the natural logarithmic of the SGMD for a considered earthquake and soil type.

The activation functions as well as the setups used during the training process are presented in Table 7. Some authors have suggested rules to identify the number of hidden neurons and their relation

Table 5. Correlation coefficients that relate the reduced set of principal components and input parameters.

Input parameter	1	2	3	4
R_C	0.531	-0.261	0.466	-0.255
M_w	0.784	0.476	-0.114	-0.069
T	0.321	-0.254	0.638	-0.414
H	0.688	-0.153	0.046	0.582
M_0	0.635	0.289	-0.437	-0.424
ϕ	0.495	-0.511	-0.017	0.420
δ	0.193	0.823	0.242	0.225
λ	-0.284	0.483	0.546	0.211

Table 6. Reduced number of input parameters after applying the PCA method.

Earthquake Type	Case	Type of relation	
		Strong	Moderate
Interplate	SS-MC	M_w, R_C, δ	M_w, R_C, T, M_0, δ, λ
	FS-MC	M_w, M_0	M_w, R_C, H, M_0, δ, ϕ
	FS-M	M_w, λ	M_w, R_C, H, T, M_0, δ, λ
Inslab	SS-MC	M_w, R_C, H, M_0, δ, λ	M_w, R_C, T, M_0, δ, λ, ϕ
	FS-MC	M_w, δ	M_w, R_C, H, M_0, δ, λ, ϕ
	FS-M	M_w, δ	M_w, H, T, M_0, δ

with the hidden layers (Masters, 1993; Swingler, 1996; Berry and Linoff, 1997), yet no closed-form expression is available to indicate the total number of hidden layers and neurons, a trial and error scheme is adopted to determine the structure of the ANN model (Shahin *et al.*, 2004).

During the trial and error process, ANN models with one and two hidden layers with 3 and up to 50 hidden neurons in each hidden layer were considered. The former was carried out to avoid potential overfitting of the ANN model.

It is noted that different metrics as the mean square error (MSE) or the mean absolute error (MAE) are available to evaluate the performance of the ANN models, each metric has advantages and disadvantages depending of the problem at hand. According to Twomey and Smith (1995), there is no consensus as to which measure should be reported, and thus, comparisons among techniques and results of different researchers are practically impossible. In this study we adopted the MSE to evaluate the performance of the ANN models.

To evaluate the impact of the number of hidden neurons and layers on the trained ANN models by using both: the samples used for training and those not employed for training, the average MSE based on 300 trials (Pozos-Estrada *et al.*, 2014), is presented in Figure 5. It is observed in Figure 5 that, in general, when the data used for training is employed, the average MSE decreases as the number of hidden neurons increases. It is also observed from Figure 5 that the average MSE when the samples used for testing are employed is greater than that observed when the samples used for training are considered. This can be explained by noting that the trained ANN models are tested with input parameters that are different than those used during the training process. This trend is

Table 7. Activation functions and training setups.

Layer	**Activation function**
Input to hidden layer Hidden to hidden layer	Tan-Sigmoid
Hidden to output layer	Linear
Training and testing	$f(x) = \frac{e^x - e^{-x}}{e^x + e^{-x}}$
Training data	80% of the complete database (randomly selected)
Testing data	20% of the complete database not selected for training
Error function	Mean square error (MSE)
Minimization algorithm	Levenberg-Marquardt (Marquardt (1963)), Press et al. (1992))

observed for the ANN models with different number of input neurons (i.e., all inputs, strong relation, moderate relation and original case) with one and two hidden layers, irrespective of the type of earthquake or soil considered. It is also observed from Figure 5 that the lowest average MSE associated with the testing stage is obtained for ANN models with 3 to 50 hidden neurons, and that the best ANN models for interplate and inslab are associated with 1HL and 2HL, respectively. Based on

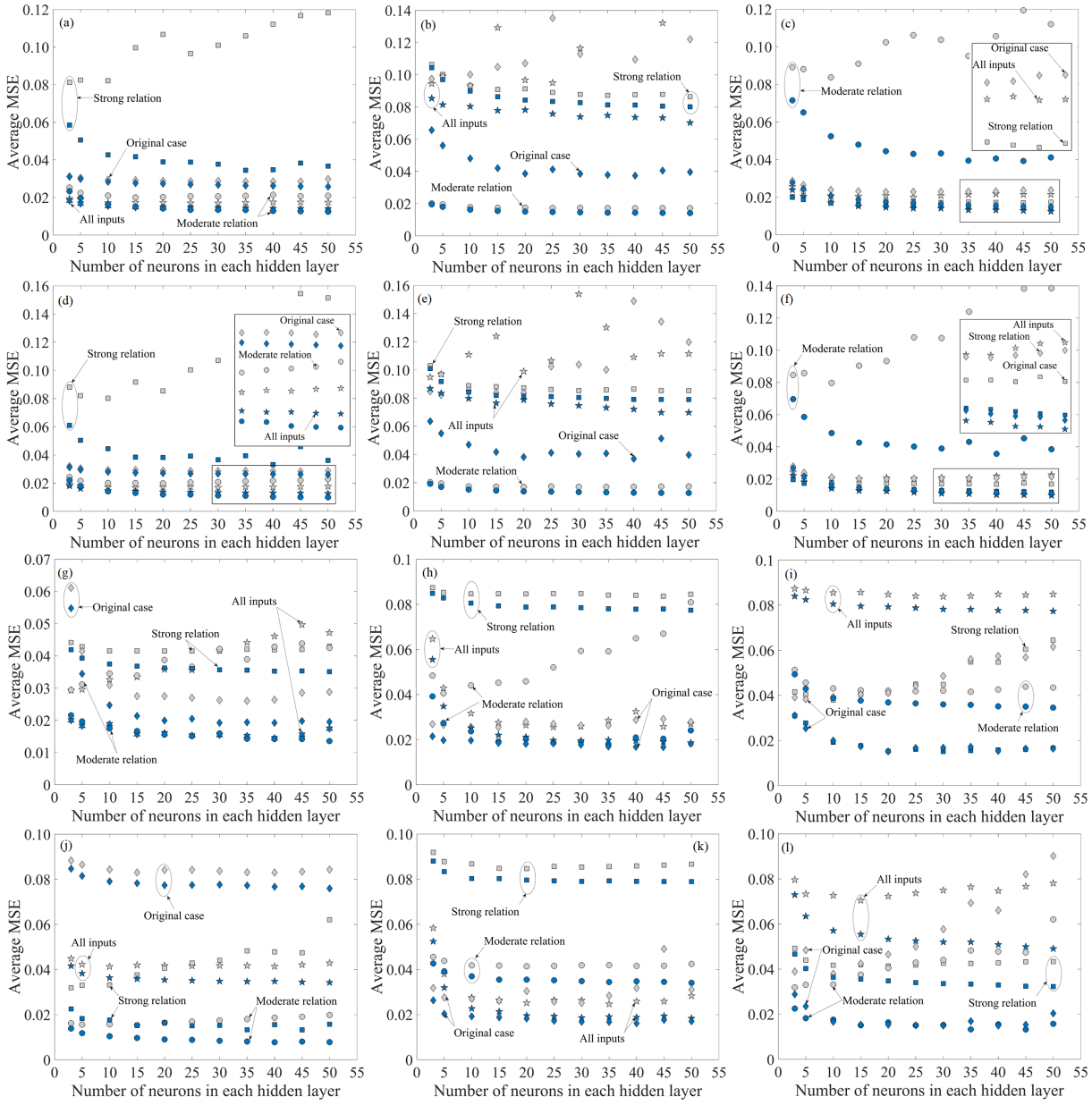

Figure 5. Average MSE for the developed ANN models by using the samples employed for training (in blue) and testing (in gray). Interplate events with one hidden layer: (a) Mexico City soft soil, (b) Mexico City firm soil, (c) Outside Mexico City firm soil. Interplate events with two hidden layers: (d) Mexico City soft soil, (e) Mexico City firm soil, (f) Outside Mexico City firm soil. Inslab events with one hidden layer: (g) Mexico City soft soil, (h) Mexico City firm soil, (i) Outside Mexico City firm soil. Inslab events with two hidden layers: (j) Mexico City soft soil, (k) Mexico City firm soil, (i) Outside Mexico City firm soil.

these observations, the parameters of the optimum ANN models (those associated with the minimum average MSE) are summarized in Table 8. It is observed in Table 8 that the number of hidden layers for the cases with different number of input neurons (i.e., all inputs, strong relation, moderate relation and original case) for interplate events ranges from 3 to 30, while that for inslab ranges from 3 to 50. This observation indicates that the selection of the inputs neurons is of paramount importance. Based on the identified optimum models with different number of input neurons, a further selection was carried out to employ a single ANN model (i.e., a single ANN model among all inputs, strong relation, moderate relation and original case) to predict the SGMD for SS-MC, FS-MC and FS-M. The criterion used to identify a single ANN model was based on selecting the ANN model which exhibits the best prediction behavior under several case scenarios. The ANN models selected to predict the SGMD for SS-MC, FS-MC and FS-M are indicated in Table 8 in italics. The obtained weights and biases for the selected trained ANN models for interplate and inslab, summarized in Table 8, are presented in Appendix A.

Comparison Between the Observed and the Predicted SGMD by Using Trained ANN

Figure 6 presents a comparison between the observed and the predicted SGMD by using the trained ANN models with the datasets used for training and testing to those obtained from the actual records. It is observed from Figure 6 that there is good agreement between the observed and predicted values in most of the cases, with a correlation coefficient, ρ, ranging from 0.50 to 0.92 when the dataset used for testing is considered, and from 0.74 to 0.96 when the dataset used for training is employed. It is also observed from Figure 6 that the highest ρ values are associated the ANN models for inslab.

Table 8. Summary of the minimum MSE of ANN models for interplate and inslab events.

Soil type	Case	Interplate		Inslab	
		MSE	ANN model	MSE	ANN model
SS-MC	All inputs	0.013	*3N-1HL*	0.032	*15N-2HL*
	Strong relation	0.024	5N-1HL	0.065	15N-2HL
	Moderate relation	0.013	30N-1HL	0.032	45N-2HL
	Original case	0.014	5N-1HL	0.031	50N-2HL
		0.014	3N-1HL*	0.031	30N-2HL*
FS-MC	All inputs	0.028	*3N-1HL*	0.010	50N-2HL
		-	-	0.032	15N-2HL*
	Strong relation	0.034	20N-1HL	0.011	5N-2HL
	Moderate relation	0.020	3N-1HL	0.011	3N-2HL
	Original case	0.036	5N-1HL*	0.015	*3N-2HL*
FS-M	All inputs	0.013	3N-1HL	0.010	*5N-2HL*
		-	-	0.009	10N-2HL*
	Strong relation	0.064	3N-1HL	0.054	30N-2HL
	Moderate relation	0.014	3N-1HL	0.046	15N-2HL
	Original case	0.017	*20N-1HL**	0.016	30N-2HL

Notes: SS-MC = Soft soil Mexico City; FS-MC = Firm soil Mexico City; FS-M = Firm soil for places outside Mexico City; N = Neurons; HN = Hidden neurons; * ANN models employed in Figure 9.

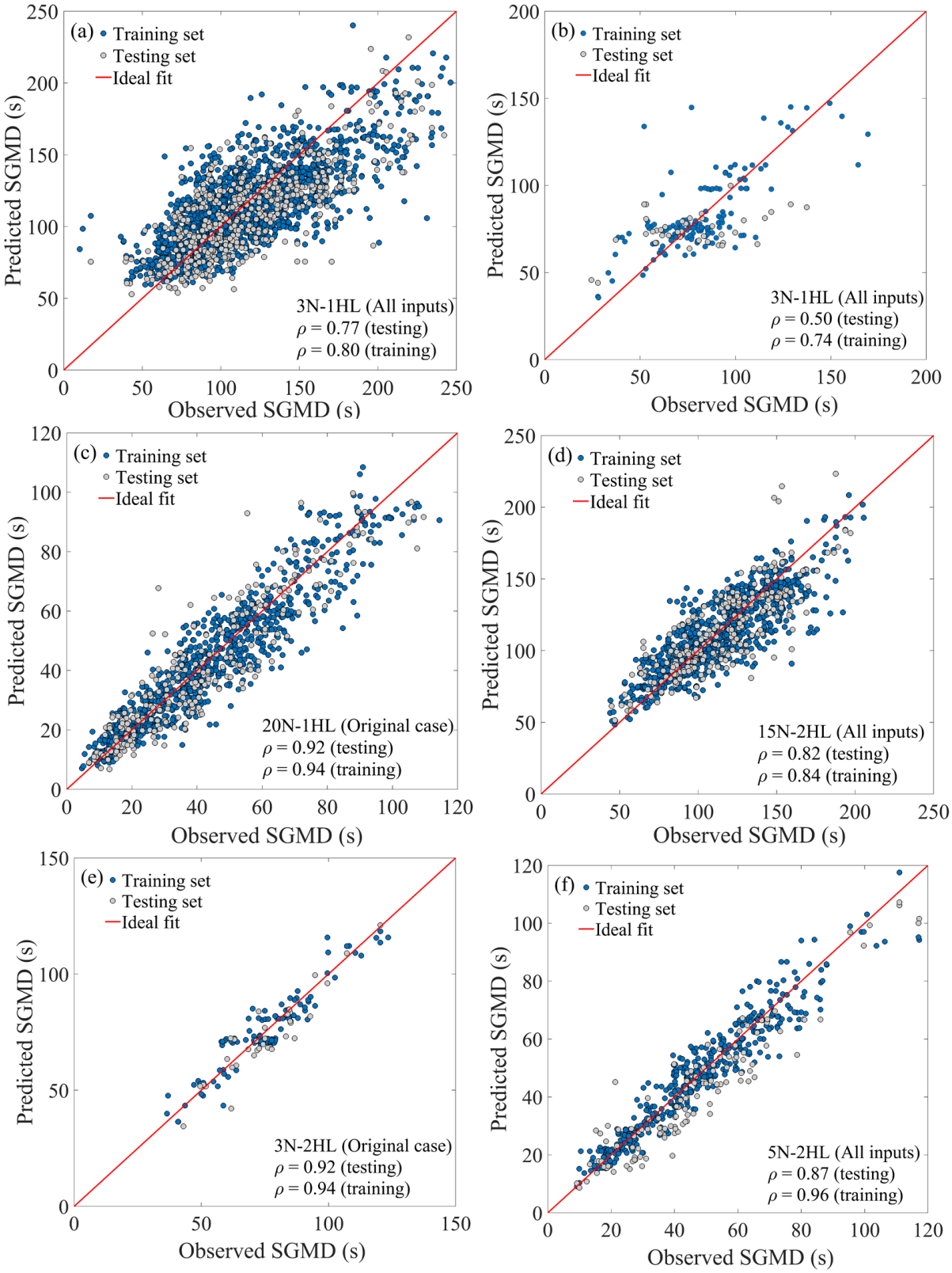

Figure 6. Comparison of the predicted SGMD with the trained ANN models and the observed values. Interplate events: (a) Mexico City soft soil, (b) Mexico City firm soil, (c) Outside Mexico City hard soil. Inslab events: (d) Mexico City soft soil, (e) Mexico City firm soil, (f) Outside Mexico City firm soil.

Among all the ANN models developed, those that predict the SGMD for sites outside Mexico City present the highest ρ values for interplate and inslab events. Further, the ANN model developed for soft soil in Mexico City for interplate events is similar to the ANN model for inslab events. On the other hand, the ANN model developed for hard soil in Mexico City for inslab events showed better predicting results that the ANN model for interplate events.

Comparison of the Predicted SGMD Using Trained ANN and Empirical Equations

Empirical Models to Estimate SGMD for Interplate and Inslab Events

The functional form of the empirical equation adopted in this study for soft and hard soils is the one proposed in Reinoso and Ordaz (2001), which is shown in Table 9, where D denotes the SGMD, in s, M_w is the moment of magnitude, R_C is the closest distance to the fault, in km, and T is the soil period, in s. In this study the model coefficients were estimated using a least-squares regression algorithm, implemented in MATLAB (2019). It is noted that that more accurate regression methods are available in the literature (Joyner and Boore, 1993; Boore *et al.*, 1997; Bommer *et al.*, 2010) and that the use of the traditional least-squares method is an oversimplification; however, for simplicity, and since the main focus of this work is on the development and discussion of the ANN models to predict the SGMD, we adopted the traditional least-squares method.

The estimated coefficients for each type of earthquake and soil are summarized in Table 9. Figure 7 presents a comparison of the predicted SGMD with the fitted empirical models and the observed values for interplate and inslab events for soft and firm soils. Similar conclusions to those draw from Figure 6 are applicable to Figure 7, except that the correlation coefficients between the observed and predicted values are in general slightly smaller than those obtained when the ANN models are used. This difference is related to the number of data used to fit the empirical models, which is greater than that employed to test the ANN models.

Comparison Between Predicted SGMD Using Trained ANN and Empirical Equations

Figure 8 presents a comparison of the variation of the SGMD predicted with the trained ANN models and that obtained with the empirical equations as a function of M_w and modal values of R_c, T, H,

Table 9. Coefficients of the empirical equation.

$$D = c_1 \exp(M_w) + (c_2 M_w + c_3) R_C + (c_4 M_w + c_5)(T + c_6) + \varepsilon$$

Interplate events					
Case	c_1	c_2	c_3	c_4	c_5
SS-MC	0.0237	-0.0212	0.3063	6.345	-25.013
FS-MC	0.0332	0.0035	0.1528	-	-
FS-M	0.0160	-0.0090	0.2361	-	-
Inslab events					
Case	c_1	c_2	c_3	c_4	c_5
SS-MC	0.0684	-0.0852	0.6722	-2.6447	38.11
FS-MC	0.0501	-0.0931	0.764	-	-
FS-M	0.027	-0.0233	0.3278	-	-

Notes: $c_{i,\ i}$ = 1,2,3,4,5, are regression coefficients; c_6 = 0.5; T is set equal to 0.5 s for firm soils (Reinoso E. Ordaz M (2001), NTC-SISMO (2017)); ε is the error term.

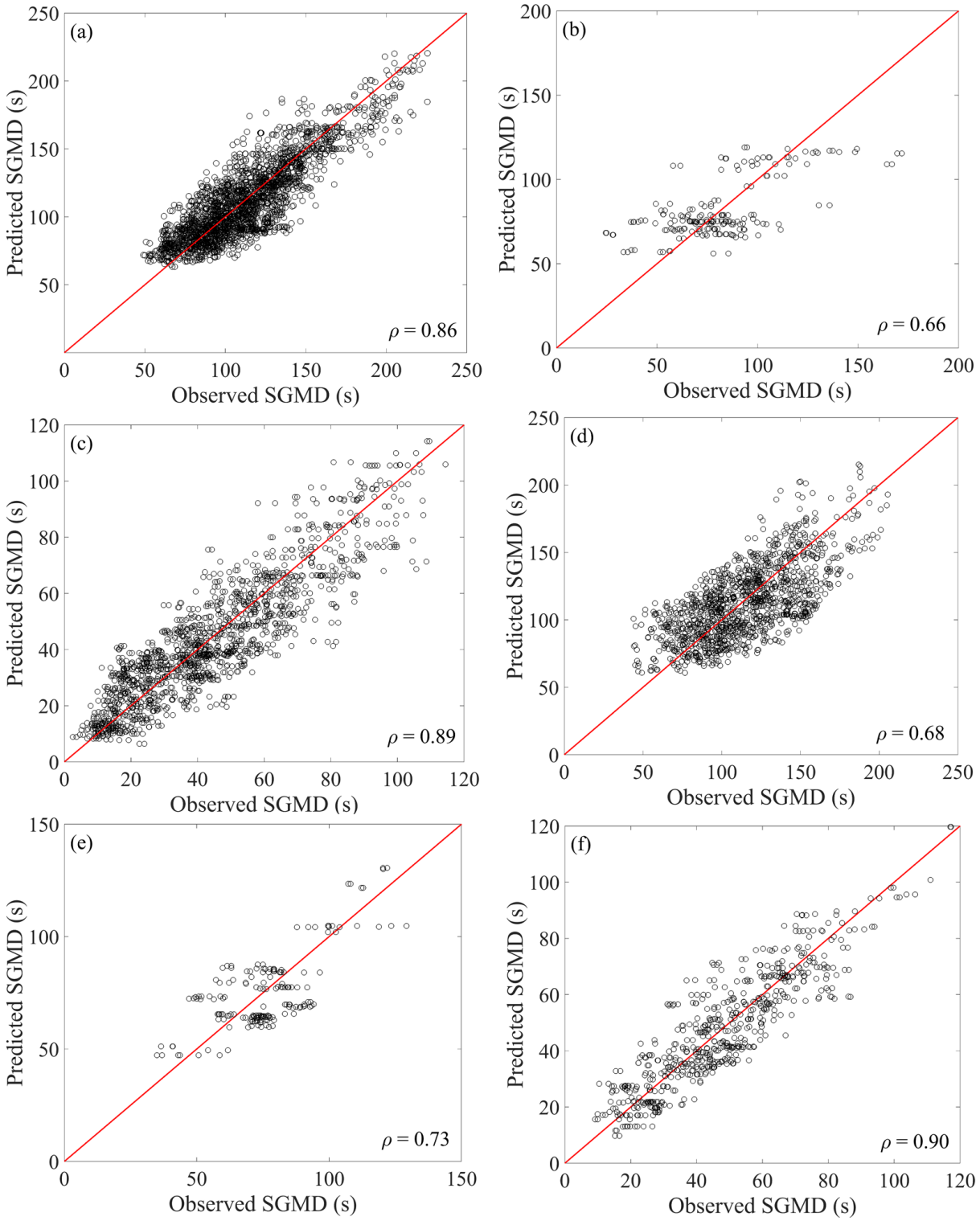

Figure 7. Comparison of the predicted SGMD with the fitted empirical models and the observed values. Interplate events: (a) Mexico City soft soil, (b) Mexico City firm soil, (c) Outside Mexico City firm soil. Inslab events: (d) Mexico City soft soil, (e) Mexico City firm soil, (f) Outside Mexico City firm soil.

M_0, ϕ, δ and λ for soft soil and modal values of Rc, H, M0, ϕ, δ and λ and T = 0.5 (s) for firm soil. It is noted that the use of H, M_0, ϕ, δ and λ are input parameters of the trained ANN models; however, they were not considered as input parameter in the empirical expressions. In Figure 8, the empirical model developed in Reinoso and Ordaz (2001), is also included for comparison purposes. It is observed from Figure 8, that in general, the predicted values by using the ANN models follow those predicted by the developed empirical equations. It is also observed that, for interplate events, the SGMD predicted with the trained ANN models oscillates within those predicted with the empirical equations. It is further observed that, for inslab events, the SGMD predicted with the trained ANN models follows the trend of the SGMD predicted with the empirical equation developed in this study. For case 8c that corresponds to the SGMD for inslab events for firm soil for places outside Mexico, the SGMD predicted by using the ANN model presents a bump for M_W within 5.5 and 6.5. The rest of the cases showed a smoother behavior. In practically all the cases presented in Figure 8, the model proposed in Reinoso and Ordaz (2001), predicted smaller SGMD values with respect to those predicted by the trained ANN models and the empirical equations developed in this study. The differences between the SGMD values predicted by the ANN models and those with the empirical equation given in Reinoso and Ordaz (2001), was also observed in the study by Alcántara *et al.* (2014).

Figure 9 presents a comparison of the variation of the SGMD predicted with the trained ANN models and that obtained with the empirical equations as a function of R_C and selected values of Mw and modal values of T, H, M_0, ϕ, δ and λ. Similar conclusions to those drawn for Figure 8 are applicable to Figure 9, except that a better behavior of the predictions made with the ANN models are observed for both inteplate and inslab events. It is noted that the ANN models used to predict the SGMD for Figure 8, were also employed for Figure 9; however, it was observed that better predictions could be obtained if ANN models with different number of neurons were used. The ANN models employed in Figure 9 are also reported in Table 8. The previous observation indicates that the trained ANN models for the considered records are not very robust because the trained models with almost identical mean square errors do not always lead to the same predicted SGMD.

To further compare the trained ANN models and the empirical equations, a probabilistic characterization of the error, defined as the difference of the logarithmic of the predicted values of SGMD by using the trained ANN models or the empirical equations for the results presented in Figure 8, and the logarithmic of the observed values is carried out. Figure 10 presents a comparison of the calculated errors in Normal probability paper. It is observed from Figure 10 that the error could be modeled as a normal variate. This was also verified with the Kolmogorov-Smirnov goodness-of-fit test (Benjamin and Cornell, 1970), which indicates that the normality hypothesis could not be rejected at a significance level of at least 1% for both type of seismic events. The mean and standard deviation of the errors presented in Figure 10 are summarized in Table 10. It is observed from Table 10 that the trained ANN models and the empirical equations are only slightly biased and that the statistics of the error for the developed ANN models are similar to those of the empirical equations. Similar results were observed for the ANN models and the empirical equations presented in Figure 9 and for that reason they are not shown.

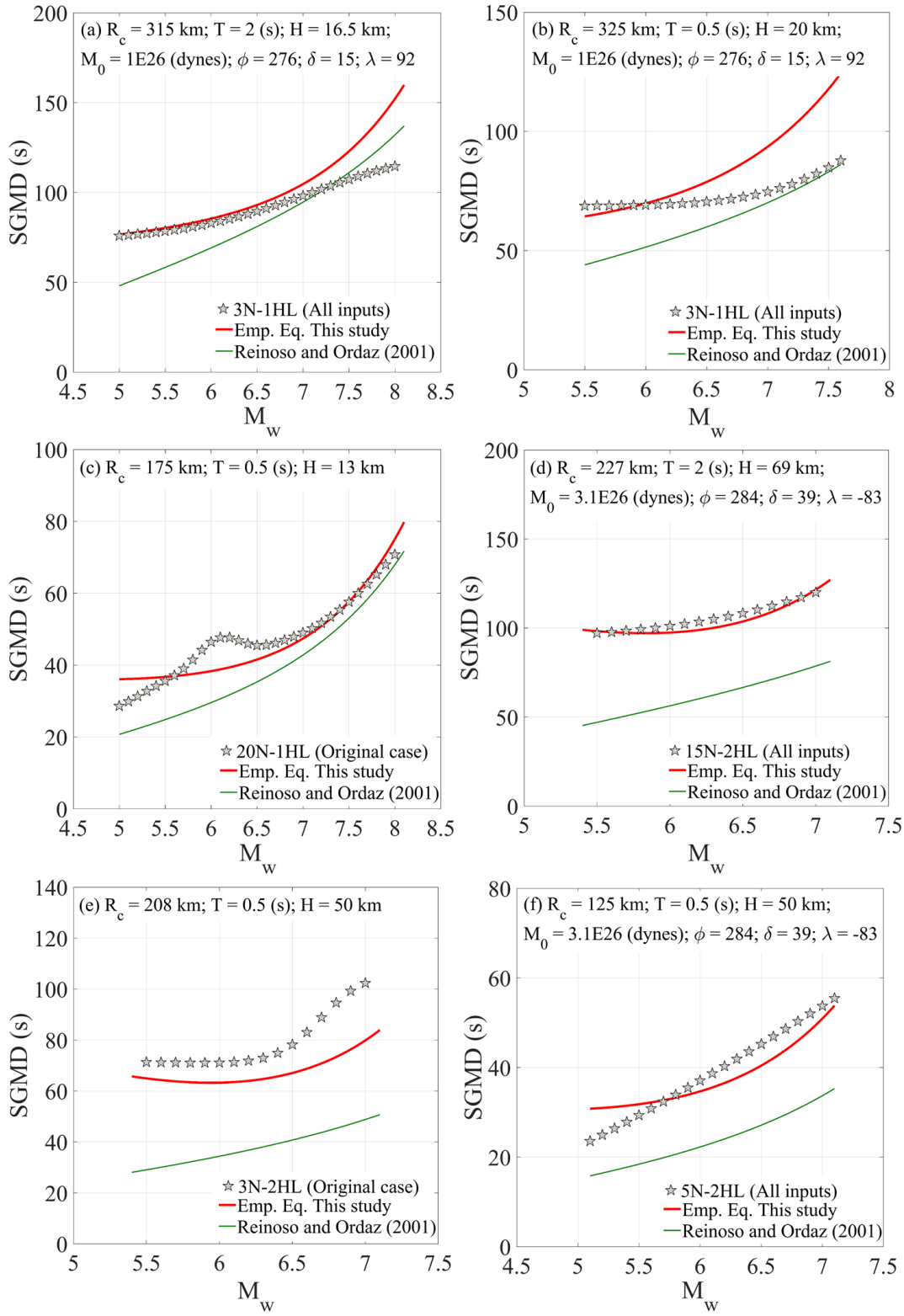

Figure 8. Comparison of SGMD predicted by the trained ANN models and by the empirical models with variation in Mw. Interplate events: (a) Mexico City soft soil, (b) Mexico City firm soil, (c) Outside Mexico City firm soil. Inslab events: (d) Mexico City soft soil, (e) Mexico City firm soil, (f) Outside Mexico City firm soil.

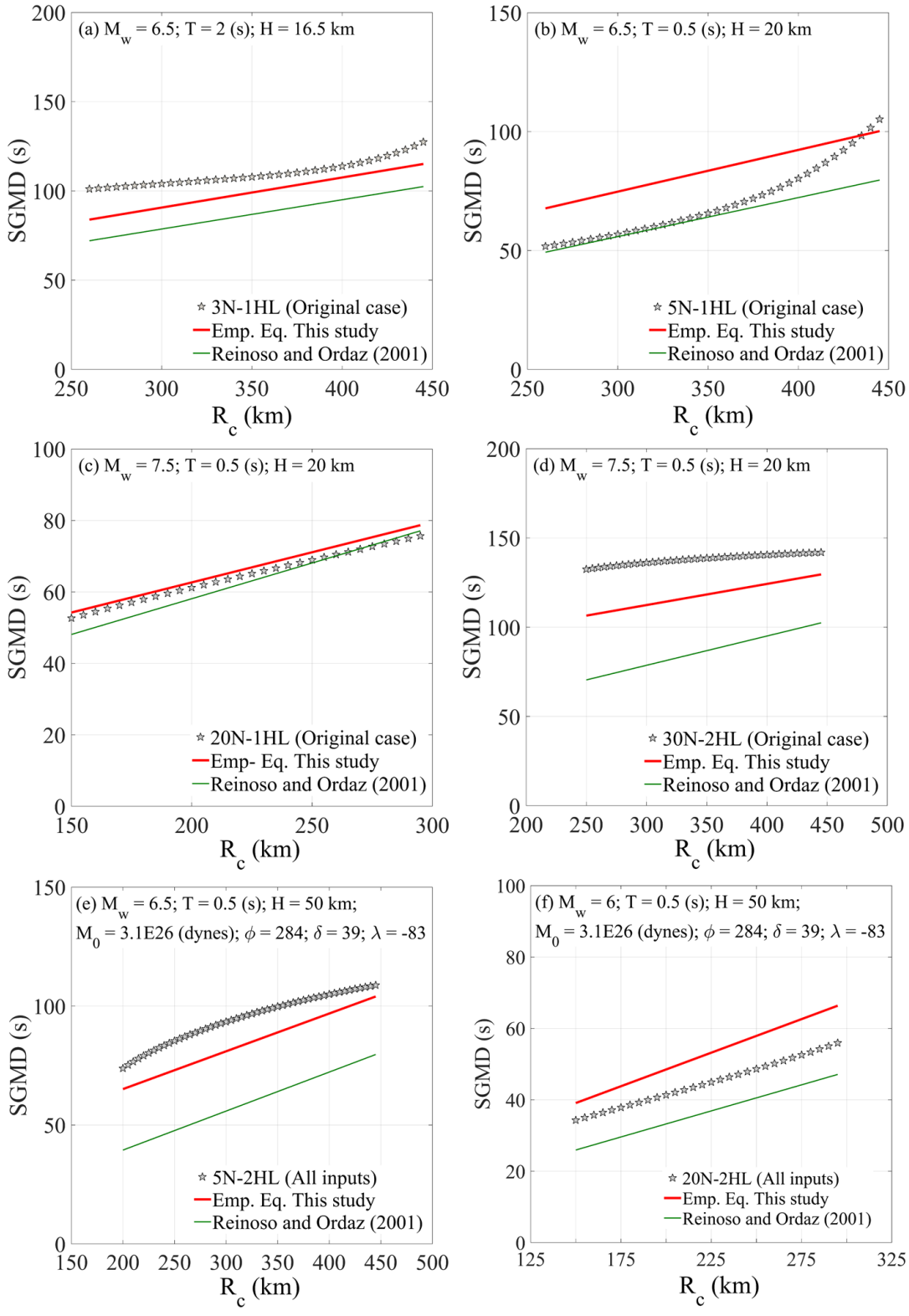

Figure 9. Comparison of SGMD predicted by the trained ANN models and by the empirical models with variation in R_C. Interplate events: (a) Mexico City soft soil, (b) Mexico City firm soil, (c) Outside Mexico City firm soil. Inslab events: (d) Mexico City soft soil, (e) Mexico City firm soil, (f) Outside Mexico City firm soil.

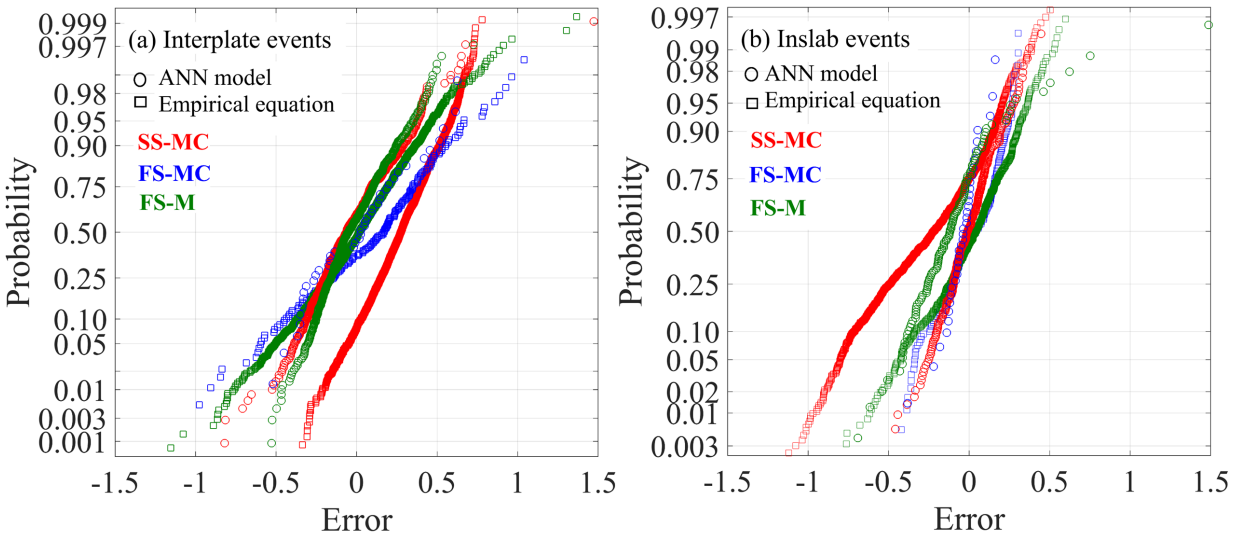

Figure 10. Normal probability paper of the error.

Table 10. Statistics of the error.

Type of earthquake	Type of soil	ANN models			Empirical equations	
		Case	Mean	Std. Dev.	Mean	Std. Dev.
Interplate	SS-MC	All inputs	-3.98E-02	0.24	2.70E-01	0.19
	FS-MC	All inputs	1.07E-02	0.31	1.01E-01	0.38
	FS-M	Original case	-2.03E-02	0.21	6.39E-03	0.3
Inslab	SS-MC	All inputs	-5.50E-03	0.16	-2.51E-01	0.32
	FS-MC	Original case	-4.14E-02	0.10	1.22E-02	0.18
	FS-M	All inputs	-1.05E-01	0.26	1.58E-02	0.24

Conclusions

Mexican records from interplate and inslab events were employed to develop Artificial Neural Network models to predict the strong ground motion duration. The principal component method was used to carry out a dimensionality reduction of the input parameters to develop the artificial neural network models. Several ANN architectures were tested. For the training of the ANN models, the input layer considered four different cases (i.e., all inputs, strong relation, moderate relation and original case), while the logarithmic of the SGMD is used to represent the output neuron.

The model tested considered up to 50 hidden neurons with one and two hidden layers. Additionally, new regression coefficients to fit empirical equations to estimate the strong ground motion duration were also obtained. The main observations that can be drawn from the analysis results are:

1. The analyses results indicated that the best prediction of the SGMD is obtained with ANN models with one hidden layer and 3, 5 and 20 hidden neurons when interplate events are considered; however, when inslab events are considered, the ANN models with two hidden layers and 3, 5, 15, 20 an 30 hidden neurons provide the best predictions.

2. The best ANN models for interplate and inslab events are associated with the cases referred to as all inputs and original case, which considered 8 and 4 input neurons, respectively. The later indicates that the selection of the inputs neurons is of paramount importance and that the ANN models could improve their prediction ability if the number of input neurons is increased.
3. The number of neurons per hidden layer of the ANN models that presented the smallest average MSE during the testing process were within 3 to 50.
4. In general, the predicted values by using the ANN models follow those predicted by the developed empirical equations. This indicates that the ANN models represent a good alternative to the empirical equations in some applications if one does not have to understand the causality to apply the ANN model.
5. In some cases, the SGMD predicted by using the ANN models presented physically unrealistic trends in its behavior. For this reason, caution is warranted when the model is extrapolated and it is recommended to carry out several verifications of the trained ANN models before using them for further engineering applications, for example the simulation of synthetic records or the evaluation of damage indices.

Acknowledgments

We thank the Coordinación de Instrumentación Sísmica del Instituto de Ingeniería de la UNAM for providing some of the records used in this work. We also thank the Instituto de Geofísica, UNAM, the Centro de Instrumentación y Registro Sísmico (CIRES), the Centro Nacional de Prevención de Desastres (CENAPRED), Red de Instrumentación Sísmica Interuniversitaria (RIIS), Fundación ICA (FICA), the Gerencia de Ingeniería Experimental y Control de la CFE (GIEC-CFE), and the Universidad Autónoma de Puebla (UAP) for the distribition of the seismic records.

References

Alcántara L., Garcia S., Ovando E., Macias C., 2014, Neural estimation of strong ground motion duration. *Geofisica Internacional*, 56 (3): 221-239. https://doi.org/10.1016/S0016-7169(14)71502-8.

Arias A., 1970, A measure of earthquake intensity, Seismic Design of Nuclear Power Plants. *R. Hansen*, Editor, MIT Press, Cambridge, Mass., pp 438-483.

Arias A., 1996, Local directivity of strong ground motion. *In Proc. 11th World Conference on Earthquake Eng.*, Acapulco, Mexico, Paper No. 1240.

Arjun C.R., Kumar A., 2011, Neural network estimation of duration of strong ground motion using Japanese earthquake records. *Soil Dynamics and Earthquake Engineering*, 31, 866–872. https://doi.org/10.1016/j.soildyn.2011.01.001.

Benjamin J.R., Cornell C.A., 1970, Probability, Statistics and Decision for Civil Engineers. McGraw-Hill, New York.

Bhargavi P., Raghukanth S.T.G., 2019, Rating damage potential of ground motion records. *Earthquake Engineering and Engineering Vibration*, 18, 233-254. https://doi.org/10.1007/s11803-019-0501-1.

Bommer J.J., Martínez-Pereira A., 1999, The effective duration of earthquake strong motion. *Journal of Earthquake Engineering*, 3(2): 127–172. https://doi.org/10.1080/13632469909350343

Bommer, J.J., Douglas, J., Scherbaum, F., Cotton, F., Bungum, H., Fah. D. (2010), On the selection of ground-motion prediction equations for seismic Hazard analysis, *Seism. Res. Lett.*, 81(5) 783 – 793. https://doi.org/10.1785/gssrl.81.5.783.

Boore, D.M., Joyner, W.B., and Fumal, T.E. (1997). Equations for estimating horizontal response spectra and peak acceleration from western North America, *Seism. Res. Lett.*, 68(1) 128 – 153. https://doi.org/10.1785/gssrl.68.1.128.

BSSC, NEHRP Recommended provisions for seismic regulations for new buildings and other structures, FEMA 450, 2004 Edition.

CMT 2013, Centroid Moment Tensor Catalog, https://www.globalcmt.org/CMTsearch.html.

Cruz J., Arredondo C., Jaimez M., 2020, New source duration relationships for Mexican earthquakes: Practical application to stochastic summation methods. *Pure Appl. Geophys.* 177, 4775-4796.

Flores-Estrella H., Yussim S., Lomnitz C., 2007, Seismic response of the Mexico City Basin: A review of twenty years of research. *Natural Hazards*, 40(2): 357-372. https://doi.org/10.1007/s11069-006-0034-6.

Franco I., Cruz C., Estrada C., 2007, Reporte preliminar del sismo del 13 de abril de 2007, Guerrero, México. *Boletín de la Sociedad Geológica Mexicana*. 59(1): 71-81.

Franke K.W., Candia G., Mayoral J.M., Wood C.M., Montgomery J., Hutchinson T., Morales-Velez A., 2019, Observed building damage patterns and foundation performance in Mexico City following the 2017 M7.1 Puebla-Mexico City earthquake. *Soil Dynamics and Earthquake Engineering*, 125, 105708. https://doi.org/10.1016/j.soildyn.2019.105708

García D., 2006, Estimación de parámetros del movimiento fuerte del suelo para terremotos interplaca e intraslab en México Central. PhD Tesis, Universidad Complutense de Madrid, Madrid, España. (In Spanish).

García D., Singh S.K., Herraiz M., Ordaz M., Pacheco J.F., 2004, Inslab earthquakes of Central Mexico: Q, source spectra, and stress drop. *Bull. Seism. Soc. Am.*, 94, 3; 789-802.

García D., Singh S.K., Herraiz M., Ordaz M., Pacheco J.F., 2005, Inslab earthquakes of Central Mexico: Peak ground-motion parameters and response spectra. *Bull. Seism. Soc. Am.*, 95, 2272-2282. https://doi.org/10.1785/0120050072.

García D., Singh S.K., Herraiz M., Ordaz M., Pacheco J.F., Cruz J. H., 2009, Influence of subduction zone structure on coastal and inland attenuation in Mexico. *Geophys. J. Int.*, 179, 215-230. https://doi: 10.1111/j.1365-246X.2009.04243.x.

Garcia J. D., 2006, Estimación de parámetros del movimiento fuerte del suelo para terremotos interplaca e intraslab en México central. Facultad de ciencias físicas, Universidad complutense de Madrid, Tesis de doctorado.

García S.R., Romo M.P., Mayoral J.M., 2007, Estimation of peak ground accelerations for Mexican subduction zone earthquakes using neural networks. *Geofisica Internacional*, 46, 1: 51 – 63.

Haykin S., 1999, Neural Networks: A Comprehensive Foundation. Prentice-Hall, Englewood Cliffs, NJ, USA, 2nd edition, 156–255.

Hong H.P., Goda K., 2007, Orientation-dependent ground-motion measure for seismic-hazard assessment. *Bull. Seism. Soc. Am.*, 97(5):1525-1538. https://doi.org/10.1785/0120060194.

Hong H.P., Liu T.J., Lee C.S., 2012, Observation on the application of artificial neural network for predicting ground motion measures. *Earthq Sci.*, 25, 161–175. https://doi.org/10.1007/s11589-012-0843-5.

Hong H.P., Pozos-Estrada A., Gomez R., 2009, Orientation effect on ground motion measure for Mexican subduction earthquakes. *Earthquake Engineering and Engineering Vibration*, 8(1): 1-16. https://doi.org/10.1007/s11803-009-8155-z.

Housner G.W., 1952, Intensity of ground motion during strong earthquakes. Calif. Inst. of Tech., Earthquake Eng. Res. Lab., Pasadena. . http://resolver.caltech.edu/CaltechEERL:1952.EERL.1952.001

Jaimes M.A., Ramirez A., Reinoso E., 2015, Ground-Motion Prediction Model From Intermediate-Depth Intraslab Earthquakes at the Hill and Lake-Bed Zone of Mexico City. *Journal of Earthquake Engineering*, 19, 1260-1278. https://doi.org/10.1080/13632469.2015.1025926.

Joyner, W.B. and Boore, D.M. (1993), Methods for regression analysis of strong-motion data, *Bull. Seism. Soc. Am.*, 83(2), 469-487. https://doi.org/10.1785/BSSA0830020469.

Kamatchi P., Rajasankar J., Ramana G.V., Nagpal A.K., 2010, A neural network based methodology to predict site-specific spectral acceleration values. *Earthquake Engineering and Engineering Vibration*, 9(4): 459-472. https://doi.org/10.1007/s11803-010-0041-1

Lindt J.W., Goh G., 2004, Earthquake Duration Effect on Structural Reliability. *Journal of Structural Engineering*, 130(5): 821-826. https://doi.org/10.1061/(ASCE)0733-9445(2004)130:5(821)

Lovric, M. 2011. International Encyclopedia of Statistical Science. Springer, Berlin, Heidelberg, p.p. 636. DOIhttps://doi.org/10.1007/978-3-642-04898-2

Lowry A.R., Larson K.M., Kostoglodov V., Bilham R., 2001. Transient fault slip in Guerrero, southern Mexico. *Geophys. Res. Lett.*, 28, 3753–3756. https://doi.org/10.1029/2001GL013238

Marquardt D.W., 1963, An algorithm for least squares estimation of non-linear parameters. *Journal of the Society for Industrial and Applied Mathematics*, 11(2):431-41. https://doi.org/10.1137/0111030

Marsal R.J., Masari M., 1959, El subsuelo de la ciudad de México, Contribución al primer Congreso Panamericano de Mécanica de Suelos e ingeniería de Cimentaciones. Facultad de Ingeniería, UNAM, México D.F. (In Spanish).

MATLAB 2019a, The MathWorks, (2019).

Moore, D. S., Notz, W., Fligner, M. A. 2013. The basic practice of statistics, New York: W.H. Freeman and Co. p.p. 654.

Normas Técnicas Complementarias para Diseño por Sismo, Reglamento de Construcciones para el Distrito Federal, Gaceta Oficial del Departamento del Distrito Federal, México. (2004). (In Spanish).

Normas Técnicas Complementarias para Diseño por Sismo, Reglamento de Construcciones para la Ciudad de México, Gaceta Oficial de la Ciudad de México (2017), México. (In Spanish).

Pande, G. N. and Shin, H.S. (2004). *Proceedings of ICE Civil Engineering 157*, February 2004 Pages 39–42 Paper 13242.

Pozos-Estrada A., Chávez M.M., Jaimes M.Á., Arnau O., Guerrero H., 2019, Damages observed in locations of Oaxaca due to the Tehuantepec Mw8.2 earthquake, Mexico. *Natural Hazards*, 97(2): 623-641. https://doi.org/10.1007/s11069-019-03662-9.

Pozos-Estrada A., Gómez R., Hong H.P., 2014, Use of neuronal network to predict the peak ground accelerations and pseudo spectral accelerations for Mexican inslab and interplate earthquake. *Geofísica Internacional*, 53(1): 39-57. https://doi.org/10.1016/S0016-7169(14)71489-8.

Press W.H., Teukolsky S.A., Vetterling A.W.T., Flannery B.P., 1992, Numerical Recipes in C: The Art of Scientific Computing. Cambridge University Press, New York. 683–688.

Principe C., Euliano N.R., Lefebvre W.C., 1999, Neural and Adaptive Systems: Fundamentals through Simulation. John Wiley and Sons, New York, NY, USA.

Reinoso E., Ordaz M., 2001, Duration of strong ground motion during Mexican earthquakes in terms of magnitude, distance to the rupture area and dominant site period. *Earthquake engineering and structural dynamics*, 30, 653-673. https://doi.org/10.1002/eqe.28.

Rodríguez P. Q., 2016, Seismic source parameters of normal faulting inslab earthquake in central Mexico. *Pure Appl. Geophys.*, 173, 2587-2619.

Rumelhart D.E., Hinton G.E., Williams R.J., 1986, Learning Internal Representation by Error Backpropagation, in Parallel Distributed Processing: Explorations Microstructure of Cognition, MIT Press, Cambridge, Mass, USA,1, 318–362.

Salmon M.W., Short S.A., Kennedy R.P., 1992, Strong motion duration and earthquake magnitude relationships. Lawrence Livermore National Laboratory, https://dx.doi.org/10.2172/67453

Shahin M., Maier H.R., Jaksa M.B., 2004, Data division for developing neural networks applied to geotechnical engineering. *Journal of Computing in Civil Engineering*, 18(2): 105 – 114. https://doi.org/10.1061/(ASCE)0887-3801(2004)18:2(105).

Singh S.K., Ordaz M., 1993, On the origin of long coda observed in the lake-bed strong-motion records of Mexico City. *Bull. Seism. Soc. Am.*, 83, 1298-1306.

Singh S.K., Reinoso E., Arroyo D., Ordaz M., Cruz-Atienza V., Pérez-Campos X., Iglesias A., Hjörleifsdóttir V., 2017, Deadly Intraslab Mexico Earthquake of 19 September 2017 (Mw 7.1): Ground Motion and Damage Pattern in Mexico City. *Seism. Res. Lett.*, 89(6) 2193 – 2203. https://doi.org/10.1785/0220180159.

Singh, S. K., Pacheco, J. F., Ordaz, M., Kostoglodov, V. 2000, Source Time Function and Duration of Mexican Earthquakes, *Bull. Seism. Soc. Am.*, 90(2), 468-482. https://doi:10.1785/0119990081.

Strasser F.O., Bommer J.J., 2009, Review: Strong Ground Motions—Have We Seen the Worst?, *Bull. Seism. Soc. Am.*, 99(5): 2613 2637. https://doi.org/10.1785/0120080300

Trifunac M.D., Brady A.G., 1975, A study on the duration of strong earthquake ground motion. *Bull. Seism. Soc. Am.*, 65(3) 581-626.

Trifunac M.D., Westermo B.D., 1982, Duration of strong earthquake shaking. *Soil Dynamics and Earthquake Engineering*, 1(3) 117–121. https://doi.org/10.1016/0261-7277(82)90002-X.

Twomey J.M., Smith, A.E. 1995. Performance measures, consistency, and power for artificial neural network models. *Mathl. Comput. Modelling*, Vol: 21(1/2), pp. 243-258.

Yaghmaei-Sabegh S., 2018, Earthquake ground-motion duration estimation using general regression neural network. *Scientia Iranica*, 25(5), 2425–2439. https://dx.doi.org/10.24200/sci.2017.4217

Yuce, B., Mastrocinque, E., Packianather, M. S., Pham D., Lambiase, A., Fruggiero, F. (2014). Neural network design and feature selection using principal component analysis and Taguchi method for identifying wood veneer defects. *Production and manufacturing research*, Vol. 2(1), 291-308. Doi: 10.1080/21693277.2014.892442

Appendix A. Weights and Biases for the Trained Models

The coefficients of the ANN models summarized in Table 8 in italics are given in the following table.

Table A1. Trained ANN models for interplate events.

Case	Weights			
	$[W_1]_{i,j}$	$[W_2]_{j,k}$	$[\phi_1]_j$	$[\phi_2]_k$
SS-MC	$\begin{bmatrix} -0.839 & 1.011 & 0.971 & -0.008 & -1.890 & -0.592 & 0.365 \\ 0.455 & -1.239 & -0.313 & -0.717 & 0.796 & 1.647 & 0.098 \\ -0.584 & 0.991 & 0.456 & -1.158 & -0.380 & -9.768 & -1.484 \end{bmatrix}$	$\begin{bmatrix} -0.614 \\ 0.999 \\ -1.442 \end{bmatrix}^T$	$\begin{bmatrix} 1.830 \\ 1.348 \\ -1.086 \end{bmatrix}$	$\begin{bmatrix} -0.693 \end{bmatrix}$
FS-MC	$\begin{bmatrix} 0.265 & -0.259 & 0.245 & -0.219 & -1.224 & 0.591 & 0.550 \\ 1.231 & 0.070 & 0.032 & 1.209 & 0.303 & 0.346 & -0.617 \\ 1.447 & 0.440 & -0.205 & 1.669 & 0.151 & 0.604 & 0.383 \end{bmatrix}$	$\begin{bmatrix} -0.278 \\ -0.447 \\ 0.385 \end{bmatrix}^T$	$\begin{bmatrix} -1.608 \\ -0.336 \\ 1.765 \end{bmatrix}$	$\begin{bmatrix} -0.344 \end{bmatrix}$
FS-M	$\begin{bmatrix} -2.460 & 1.128 & -1.598 & 0.679 \\ -1.169 & 1.676 & -2.565 & -0.437 \\ 0.125 & 2.481 & -0.627 & 0.674 \\ 1.532 & -1.421 & -0.608 & 1.836 \\ 1.039 & 0.037 & -2.611 & 0.449 \\ 0.182 & -2.277 & 0.936 & -1.718 \\ -2.107 & 0.495 & -0.785 & 1.543 \\ -2.949 & 1.083 & 1.394 & 0.851 \\ 1.833 & -1.087 & 1.115 & -1.125 \\ -2.168 & -0.932 & -0.587 & -0.039 \\ 0.166 & 2.162 & -0.441 & 0.812 \\ -3.503 & -1.550 & -0.533 & -0.057 \\ 0.751 & -0.498 & 0.358 & -2.794 \\ -0.213 & 1.587 & 2.650 & 0.335 \\ 1.931 & 1.533 & 0.941 & -1.366 \\ 0.703 & -0.945 & 2.787 & 0.533 \\ -3.326 & -0.361 & -1.196 & 0.465 \\ -2.907 & -0.053 & -1.008 & 0.658 \\ -1.962 & -1.879 & 0.812 & 1.068 \\ 0.505 & 0.771 & 1.969 & 0.885 \end{bmatrix}$	$\begin{bmatrix} -0.944 \\ 1.075 \\ 0.261 \\ 0.000 \\ -0.125 \\ -0.241 \\ 0.448 \\ 0.162 \\ 0.495 \\ -1.193 \\ 0.495 \\ 0.784 \\ 0.161 \\ -0.177 \\ 0.124 \\ -0.117 \\ 1.064 \\ -0.935 \\ 0.535 \\ 0.168 \end{bmatrix}^T$	$\begin{bmatrix} 2.484 \\ 2.975 \\ -2.181 \\ -2.023 \\ -1.952 \\ -1.489 \\ 1.363 \\ 0.523 \\ -0.394 \\ -0.505 \\ -0.536 \\ -0.354 \\ -1.315 \\ 0.855 \\ 1.120 \\ 0.683 \\ -2.630 \\ -2.448 \\ -2.600 \\ 3.408 \end{bmatrix}$	$\begin{bmatrix} 0.136 \end{bmatrix}$

Table A2. Trained ANN models for inslab events.

Case	Weights				
	$[W_1]_{i,j}$	$[W_2]_{j,k}$	$[W_3]_{k,j}$	$[\phi_2]_k$	$[\phi_2]_k$ / $[\phi_3]_1$
SS-MC	-0.594 0.392 -1.109 0.757 0.672 -0.829 0.123 0.599 0.640 0.142 -0.738 0.437 0.871 -0.585 0.620 0.906 -0.333 0.828 1.272 -1.303 -0.376 -0.534 0.398 0.681 0.536 0.728 0.462 -1.067 0.400 -0.343 1.378 0.498 0.138 0.043 -0.249 -0.514 0.373 -0.514 -0.001 1.034 0.237 0.779 1.362 -0.687 0.616 -0.291 0.121 -0.376 0.643 -0.940 -0.500 -0.486 0.868 0.564 0.383 0.157 0.420 -0.085 1.128 0.607 0.359 -0.719 -0.223 -0.763 -0.158 -0.958 0.239 -0.764 -0.774 0.986 0.351 -0.031 0.560 -0.922 -0.065 0.533 0.608 0.363 0.524 -0.793 -0.821 -0.462 0.948 0.397 -0.191 0.897 0.337 -0.532 0.341 0.247 -0.324 -0.831 0.622 0.585 0.677 -0.981 1.507 -1.054 0.689 0.032 0.943 -0.509 -0.140 -0.140 -0.633 -0.905 -0.332 0.040 -0.403 -0.436 -0.439 0.418 -0.707 0.739 -0.700 0.256 0.721 0.095 0.693 0.151	-0.296 0.417 -0.019 -0.523 -0.108 -0.077 0.486 0.587 0.384 -0.142 0.853 -0.527 0.437 -0.446 -0.642 -0.485 -0.313 -0.569 -0.141 0.613 0.390 0.267 -0.726 0.127 -0.473 0.414 -0.474 -0.122 0.502 0.025 -0.522 0.372 -0.366 -0.471 0.142 -0.073 0.576 -0.891 0.522 -0.092 0.657 -0.716 -0.441 -0.111 0.588 0.139 0.522 0.981 0.444 0.180 -0.771 0.297 -0.407 0.180 -0.049 -0.524 -0.303 0.584 -0.393 -0.223 0.391 -0.076 0.345 -0.885 0.270 0.528 0.813 -0.141 -0.331 0.301 0.061 0.672 -0.712 0.132 -0.367 -0.210 0.217 0.983 0.430 0.329 -0.849 0.215 0.472 0.612 0.113 0.247 0.534 0.002 0.080 0.303 0.279 0.105 -0.419 0.417 0.066 -0.254 -0.231 0.451 0.625 -0.899 -0.956 -0.121 0.265 0.665 0.586 0.132 0.614 -0.393 -0.318 -0.035 0.529 0.021 0.422 -0.344 -0.301 -0.605 0.324 0.146 0.327 0.528 -0.463 0.191 0.339 0.219 -0.304 0.260 -0.687 0.240 -0.505 -0.268 0.605 -0.018 0.534 0.228 -0.533 -0.115 -0.764 0.454 -0.156 -0.514 0.813 0.024 -0.070 0.103 0.252 -0.460 0.468 -1.160 -0.288 0.355 0.740 0.210 0.739 0.120 -0.181 0.741 -0.067 0.509 0.250 -0.105 0.026 0.306 -0.026 0.243 -0.925 0.602 -0.674 -0.900 0.040 -0.645 0.814 0.375 -0.159 -0.529 0.147 -0.374 0.289 0.431 0.414 -0.162 -0.294 0.236 0.698 0.641 -0.460 0.281 -0.023 -0.028 -0.319 0.808 -0.483 0.390 0.217 0.122 -0.632 -0.437 0.352 -0.612 -0.390 -0.372 -0.391 0.121 -0.237 -0.060 0.736 -0.004 0.076 0.634 -0.449 0.685 -0.545 0.348 0.364 0.391 0.368 -0.032 -0.351 -0.256 0.099 -0.436 0.233 -0.515 -0.495 -0.455 0.238	0.635 0.044 -0.652 0.809 -0.472 -0.713 -0.872 0.341 -0.064 0.923 -0.652 -0.999 0.313 0.095 -0.004	1.755 -1.708 1.022 -0.995 -0.719 -0.375 -0.094 0.275 -0.188 0.413 -0.759 1.157 1.229 -1.699 -1.969	1.694 1.276 1.091 -0.990 -0.741 0.522 -0.197 0.003 -0.271 -0.488 0.861 0.987 -1.166 -1.398 -1.798 / 0.770
FS-MC	1.079 -1.056 0.830 -0.093 -0.792 -0.215 1.328 0.986 0.026 -1.370 0.584 -0.091 -0.091 -0.395 0.659 0.938 -1.103 1.314 -1.258 0.181 0.492 1.342 -1.064 0.234	0.000 -1.105 -2.284 -1.594 -0.911 0.233 1.669 -1.603 1.891	1.061 -0.653 1.032	-1.475 0.522 -2.212	-1.417 0.072 1.520 / 0.667
FS-M	0.540 -3.950 1.335 -0.837 -0.419 -0.677 1.435 0.278 0.156 0.403 0.135 -0.015 -0.072 -0.075 0.067 -0.019 -0.944 -2.716 2.295 -0.692 0.496 -1.447 -1.252 -2.580 2.182 3.261 -2.212 0.813 -0.183 2.232 -0.173 0.959 -0.294 -1.913 0.601 -0.282 0.497 1.827 2.503 -0.006	1.453 -1.713 -1.065 -0.690 2.435 -0.304 0.699 0.204 -0.425 0.297 -0.893 1.304 -1.802 0.760 0.616 -1.843 0.751 1.287 0.765 0.812 1.013 -1.205 0.243 1.581 1.613	-0.457 2.043 0.119 -0.677 -1.227	2.029 0.160 -0.668 2.556 -1.283	-2.161 0.187 -0.630 -0.209 2.070 / 1.137

Original paper

https://doi.org/10.22201/igeof.00167169p.2022.61.3.2129

Simulation of Stress Tests Using a Poroelastic Model to Estimate the Permeability Behavior of Bedford Limestone Samples

Mario E. Vadillo-Sáenz[1], Martín A. Díaz-Viera*, Aarón Domínguez-Torres[1], Enrique Serrano-Saldaña[1] and Manuel Coronado[1]

Received: March 5, 2021; accepted: May 27, 2022; published on-line: July 1, 2022.

Resumen

Por su relevancia en Geociencias, el efecto de los esfuerzos sobre las propiedades de flujo de fluido en rocas ha sido estudiado experimental y teóricamente por varias décadas. Los trabajos se han orientado principalmente a rocas tipo arenisca, y relativamente poco, a pesar de su relevancia, en rocas carbonatadas. Por otro lado, la descripción del fenómeno es matemática y numéricamente complejo, ya que involucra el acoplamiento no lineal del flujo de fluido con la deformación de la roca. En este trabajo se busca incursionar en esa parte poco explorada de pruebas experimentales en carbonato y su simulación numérica. En él se presentan pruebas experimentales realizadas en núcleos de caliza Bedford, y se analiza el efecto de los esfuerzos de confinamiento y de la presión del fluido (presión de poro) sobre la permeabilidad a través de dos tipos de pruebas, conocidas como hidrostáticas (bajos esfuerzos de corte) y no hidrostáticas (altos esfuerzos de corte). En este trabajo se presenta un modelo matemático para describir el fenómeno, considerando un fluido monofásico, una respuesta elástica de la roca, y su implementación numérica en elementos finitos. El acoplamiento del flujo de fluido con los esfuerzos se modela utilizando relaciones algebraicas de porosidad y permeabilidad en función del esfuerzo. La relación permeabilidad-esfuerzo utilizada en este trabajo depende linealmente de la deformación volumétrica y la presión de poro. Los resultados experimentales muestran que en general la permeabilidad se incrementa con la presión del fluido y se reduce con el esfuerzo de confinamiento. La reducción con el esfuerzo de confinamiento en el rango de esfuerzos de confinamiento analizado es relativamente pequeña, pero es notoriamente más importante en las pruebas no-hidrostáticas (8%) que en las hidrostáticas (2%). El ajuste del modelo a los resultados experimentales, específicamente a la caída de presión en el núcleo en función del tiempo, se realiza mediante la variación de los parámetros de la relación permeabilidad-esfuerzo. El valor de estos parámetros de ajuste difiere del valor reportado para areniscas, lo cual puede ser indicativo de la diferencia en la estructura porosa y las propiedades mecánicas de las rocas.

Palabras Clave: simulación, poroelasticidad, prueba de esfuerzo y permeabilidad.

Editorial responsibility: Ana Teresa Mendoza Rosas

**Corresponding author at mdiazv@imp.mx*
[1]Instituto Mexicano del Petróleo (IMP)Eje Central Lázaro Cárdenas Norte 152, San Bartolo Atepehuacan, Gustavo A. Madero, Ciudad de México.

Abstract

Due to its relevance in Geosciences, the stress effect on the dynamic rock properties has been studied experimentally and theoretically for several decades. These works have been oriented mainly to sandstones, and relatively few to carbonate rocks, despite its relevance. On the other hand, the description of the phenomenon is mathematically and numerically complex since it involves the non-linear coupling of the fluid flow with the rock deformation. This work seeks to analyze that little-explored part of experimental tests in carbonates com bined with its numerical simulation. It presents experimental tests carried out on Bedford limestone cores and analyzes the effect of confinement stress and fluid pressure (pore pres sure) on its permeability, by two test types, known as hydrostatic (low shear stress) and not hydrostatic (high shear stress) tests. In this work, a mathematical model is presented to describe the phenomenon, considering a single-phase fluid, an elastic rock response, and its numerical implementation in finite elements. The coupling of fluid flow with stress is regularly modeled by algebraic relationships of porosity and permeability as a function of stress. A permeability-stress relationship used in this work depends linearly on volumetric strain and pore pressure. The experimental results show that in general, the permeability increases with fluid pressure and decreases with confinement stress. The reduction with the confinement stress is small in the range of confinement stresses analyzed, but it is noticeably more important in the non-hydrostatic tests (8%) than in the hydrostatic ones (2%). The model fitting to experimental data, specifically to the core pressure drop as a function of time, is carried out through the variation of the permeability-stress relationship parame ters. The fitting parameters value differs from the reported value for sandstones, which may be indicative of the difference in the porous structure and mechanical properties of the rocks.

Key words: simulation, poroelasticity, stress test and permeability

Nomenclature

A	Core cross-sectional area [L^2]
c_o	Storage coefficient [$M^{-1}\ LT^2$]
c_f	Fluid compressibility [$M^{-1}\ LT^2$]
c_s	Solid grain compressibility [$M^{-1}\ LT^2$]
D	Core diameter [L]
E	Drained Young modulus [$ML^{-1}\ T^{-2}$]
g	Gravity acceleration [LT^2]
G	Shear modulus [$ML^{-1}\ T^{-2}$]
k	Permeability [L^2]
k_o	Initial permeability [L^2]
$\boldsymbol{k}$	Permeability tensor [L^2]
K	Drained bulk modulus [$ML^{-1}\ T^{-2}$]
K_s	Bulk modulus solid [$ML^{-1}\ T^{-2}$]
L	Core length [L]
Δp	Pressure drop [$ML^{-1}\ T^{-2}$]
p	Fluid pressure [$ML^{-1}\ T^{-2}$]
p_∂	Pressure at the boundary [$ML^{-1}\ T^{-2}$]
p_0	Initial pressure [$ML^{-1}\ T^{-2}$]
p_{in}	Inlet pressure [$ML^{-1}\ T^{-2}$]
p_{out}	Outlet pressure [$ML^{-1}\ T^{-2}$]
q_f	Fluid source term [T^{-1}]
Q_{max}	Maximum flow rate [$L^3\ T^{-1}$]
R	Core radius [L]
R_e	Reynolds number [-]
t	Time [T]
t_S	Time to reach steady state flow [T]
$\boldsymbol{T}$	Traction [$ML^{-1}\ T^{-2}$]
$\boldsymbol{T}_\partial$	Traction at the boundary [$ML^{-1}\ T^{-2}$]
$\boldsymbol{u}$	Fluid velocity [LT^{-1}]
u_{in}	Injection flow rate [$L^3\ T^{-1}$]
$\boldsymbol{u}_\partial$	Fluid flow at the boundary [LT^{-1}]
V_r	Rock volume [L^3]
ω	Displacement [L]
ω_δ	Displacement at the boundary [L]
ω_0	Initial displacement [L]
W_d	Core dry weight [M]

Greek

α	Biot-Willis coefficient [-]
β_1, β_2	Permeability fitting parameters[-]
ε_v	Volumetric strain [-]
λ	First Lamé constant [$ML^{-1}\ T^{-2}$]
μ	Fluid viscosity [$ML^{-1}\ T^{-1}$]
ν	Drained Poisson ratio [-]
ϕ	Porosity [*fraction*]
ϕ_0	Initial Porosity [*fraction*]
ρ	Fluid density [ML^{-3}]
ρ_e	Effective density [ML^{-3}]
ρ_s	Solid density [ML^{-3}]
σ_1, σ_2 ,σ_3	Main stresses [$ML^{-1}\ T^{-2}$]
$\boldsymbol{\sigma}_c$	Confining stress [$ML^{-1}\ T^{-2}$]
$\boldsymbol{\sigma}_e$	Effective stress [$ML^{-1}\ T^{-2}$]
σ_T	Total stress [$ML^{-1}\ T^{-2}$]
Ω	Simulation domain

Introduction

The behavior of saturated rocks under stress changes has been a recurring issue in several areas given the importance of knowing and predicting, for example, future production scenarios of a reservoir, storage of residual gas, basin subsidence, etc. The importance lies in the fact that, the coupling between fluid flow and mechanical behavior impacts the flow capacity of the porous medium as a consequence of the stress on its porous structure, altering the porosity and permeability of the rock. In oil reservoirs, it has been found that oil recovery can be importantly overestimated if the geomechanical effects are neglected (Ojagbohunmi *et al.* (2012).

Diverse publications on rock geomechanics have been devoted to experimentally analyze the stress-fluid coupling due to stresses in poroelastic media under diverse conditions (among others, Brace (1965), Jones and Smart (2002), Ma *et al.* (2012), Huo and Benson (2016), Han *et al.* (2016) and Belmokhtar *et al.* (2017)), and to analyze the permeability dependence on applied stress (Zhu *et al.* (1997), Zhu and Wong (1997), Lion *et al.* (2004), Fortin *et al.* (2005), Al-Quraishi *et al.* (2010), Takahashi *et al.* (2013) and Wang *et al.* (2016)). Simultaneously, other works have developed poroelastic models to mathematiccally describe the stress effects on permeability (Mandel (1953), Abousleiman *et al.* (1996), Cui and Abousleiman (2001) and Lamb and Gorman (2010)), and have also proposed empirical and theoretical correlations of the porosity and permeability dependence on stress and pore pressure (Kozeny (1927), Carman (1956), Walder and Nur (1984), David *et al.* (1994),Touhidi-Baghini (1998), Mainguy and Longuemare (2002) and Ma (2015)). Also, some few numerical simulations of this flow-stress coupling in homogeneous and fractured rocks have also been published (Bai *et al.* (1997), Rinaldi and Rutqvist (2016), Roded and Holtzman (2017), Agheshlui *et al.* (2018), Goral *et al.* (2020) and Sasaki and Rutqvist (2021)). Some of the conclusions are in general, that permeability changes result from a competetion between two mechanisms, (i) rock structure compaction that increases tortuosity and causes a decrease in permeability, and (ii) dilation of voids, that increases pore volume and increments permeability (Jones and Smart, 2002; Han *et al.*, 2016). The presence of micro-fractures and large fractures in the rock can also importantly impact permeability response to stresses (Barthelemy, 2009).

Despite of its relevance, only few of the published experimental works consider carbonate rocks, and only few of them apply mathematical and numerical models to analyze and describe the observed permeability results as function of confinement stress. This work analyzes that little-explored part of experimental tests on carbonate rocks combined with their numerical simulation using a permeability-stress relationship linearly dependent on volumetric strain and pore pressure.

The paper is organized as follows. In the first section an introduction and a literature review is provided. In the second section a description of the experimental setup, the laboratory tests and the test results are given. In the third section, the poroelastic model is presented including the mathematical formulation, the initial and boundary conditions, the numerical discretization and its computational implementation. In the fourth section the application of the model to the hydrostatic and non-hydrostatic experimental tests is shown. In this section, also a comparison between the numerical simulation and the permeability experimental results is presented. The concluding remarks are shown in the last section.

Experimental Setup

The Bedford limestone samples employed in this study (see Fig. 1) were characterized by X-ray diffraction analysis (XDR), X-ray micro-tomography and geomechanical testing. Their composition is 97 %w calcium carbonate and 3 %w silicon oxide. They have an average effective porosity of 13.8 %, a pore throat size in the range of 40-52 μm, very irregular grain shapes with grain density of 2,711 kg/m^3, a drained Young modulus ($\boldsymbol{E}$) of 16.1 GPa, and a drained Poisson ratio ($\boldsymbol{\nu}$) of 0.15 (Coronado, 2019).

Figure 1. Bedford limestone sample used in this work.

The permeability study was performed in two cylindrical samples (A and B) which were cored from a Bedford limestone block. The dimensions and physical properties of the cores are shown in Table 1. The displacement fluid used in the test was distilled water in order to prevent pore obstruction due to scale formation and deposition, and also to avoid calcite dissolution.

Traditionally, Hoek and Hassler coreholders are used in laboratory to measure dynamical properties as function of the rock mechanical properties. Instrumented Hoek triaxial coreholders can handle independently axial and confining (radial) stress and allow strain measurements in both radial and axial directions (Hoek and Franklin, 1968). In contrast, Hassler coreholders used in SCAL testing (McPhee *et al.*, 2015) (Figure 2) can work in two possible test configurations: hydrostatic and non-hydrostatic. In the first case the radial confining stress equals the stress on the sample endfaces. On the other hand, in the second case, the radial confining stress differs from the endface stress. Sample A was employed in the non-hydrostatic tests, and sample B in the hydrostatic ones. Here, for evaluating stress effects on samples permeability a Hassler coreholder was used. The core is loaded in a Viton rubber sleeve and its endfaces are set in contact with the stainless steel difusser at each end. These are attached to the inlet and outlet fluid lines.

Table 1. Physical properties of the Bedford limestone samples.

Property	Dimensions	Bedford A	Bedford B
Core length (L)	m	0.127	0.123
Core diameter (D)	m	0.1016	0.1016
Porosity (ϕ)	%	13.6	14.0
Permeability (k)	m^2	1.51×10^{-13}	1.23×10^{-13}
Core cross-sectional area (A)	m^2	8.17×10^{-3}	8.17×10^{-3}
Rock volume (V_r)	m^3	1.03×10^{-3}	1.00×10^{-3}
Core dry weight (W_d)	kg	2.25	2.18

The fluid displacement system is composed by a Quizix pump Q5000, a back pressure regulator (BPR) controlled by a Teledyne Isco 260D syringe pump, pressure and temperature sensors and a National Instruments data acquisition unit. The pressure sensors measure the pressure at the sample endfaces, and the differential pressure transducer measures the pressure drop across the sample. The temperature sensor was set at coreholder body. The data adquisition system was programmed in LabVIEW 2018. A schematic view of the displacement system is shown in Figure 3.

The confining stress was applied by pressurizing the hydraulic fluid (distilled water) between the wall of the coreholder and the Viton sleeve. This confining stress was servo controlled by the Quizix pump. The Viton sleeve used to seal the sample was capable of withstanding a maximum confining pressure of 27.5 MPa without rupture. The sample pore pressure was set by pressurizing distilled water inside the sample, controlled by the BPR. A clean and dry sample covered by the viton rubber was set in the coreholder. After assembling the system and calibrating the pressure and temperature sensors, all the fluid lines together with the sample was air evacuated for 45 min.

Following the standard method, the sample was saturated at a confining stress (σ_c) of 13.8 MPa and at a room temperature (295 K). A constant flow rate of 0.1 ml/min was applied until the inlet pressure (p_{in}) reaches a plateau (approximately after 48 h) at 6.9 MPa. The resulting differential pressure (σ_c-p_{in}) of 6.9 MPa was enough to avoid core-sleeve interface flow and provides a seal between the sleeve and the coreholder.

The initial connected porosity was calculated from the saturated sample density, by considering distilled water and the rock matrix densities (Ramos da Silva *et al.* (2010). The resulting porosity values are 13.6 % and 14.0 % for A and B samples, respectively.

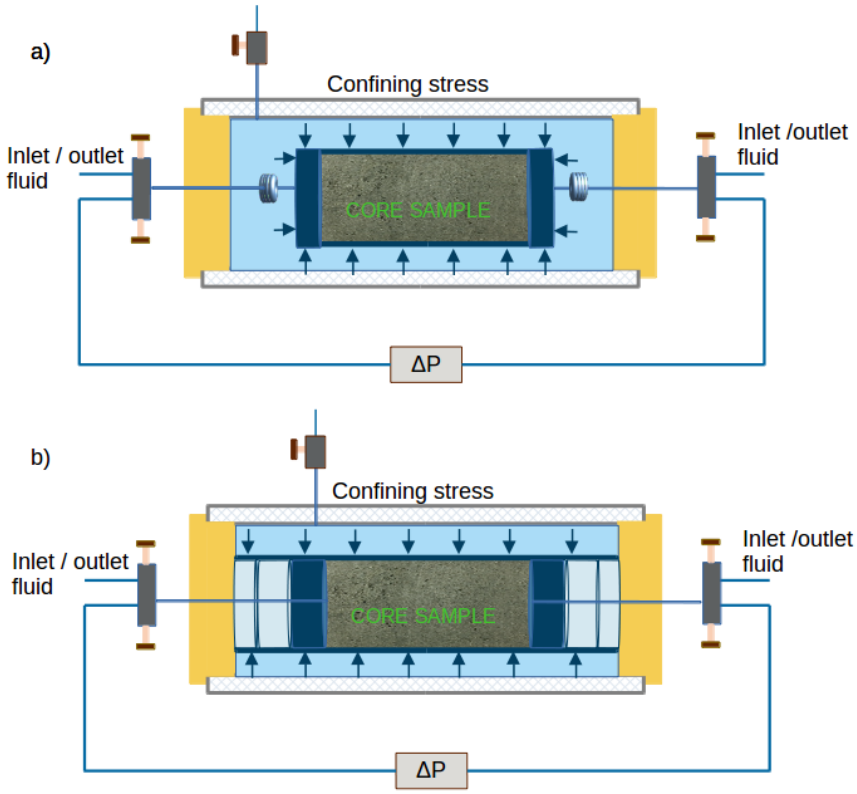

Figure 2. a) Hydrostatic and b) non-hydrostatic coreholder configurations.

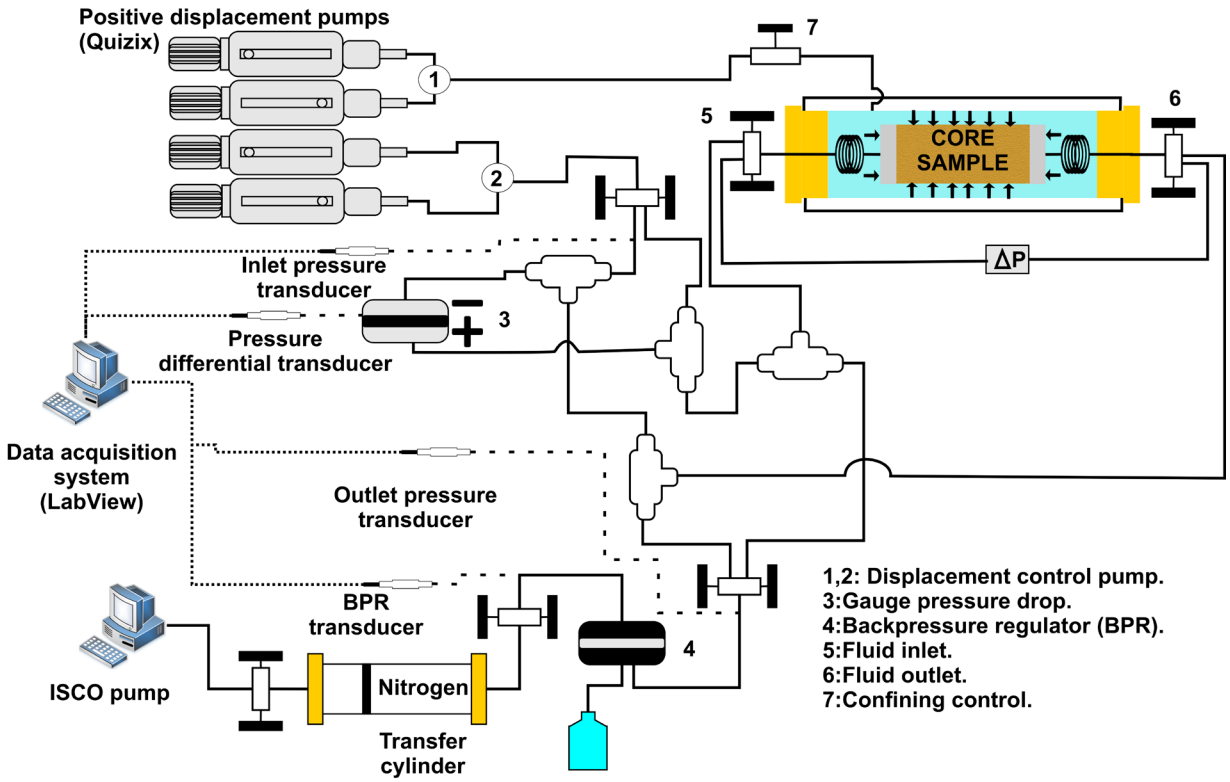

Figure 3. Displacement system scheme.

Four permeability tests on samples A and B were carried out using the steady state method at constant flow rate (1, 2, 3 and 4 ml/min). The pressure drop was used to evaluate the permeability by the Darcy's law. The laminar flow assumption behind Darcy's law (Glowacki and Seladurai (2016) Selvadurai and Selvadurai (2010) holds, since the estimated maximum interstitial fluid velocity is 5×10^{-5} m/s, which corresponds to a maximum Reynolds number (R_e) of 0.003, and satisfies the Philips (1991) condition $R_e<\phi$, and Bear (1972) condition $R_e<\phi$. The permeability values obtained at these confining stresses are 1.51×10^{-13} m^2 and 1.23×10^{-13} m^2 for A and B samples, respectively.

In the non-hydrostatic test, the outlet pressure was controlled by the BPR and the inlet pressure was set by the Quizix pump at constant pressure (6.9 MPa), that is achieved by adjusting its flow rate. The axial stress equals the atmosferic pressure and the boundary condition at the core sample axial faces is zero displacement (see Figure 4). The experiment starts with the application of a series of confining stress for a time period of 40 min. During this time, the inlet and outlet pressures, the pressure drop, the confining pressure, the injected and recovered fluid volumes and the temperature were recorded. These tests are carried out for eight confining stresses as shown in Table 2.

The hydrostatic tests have the same boundary conditions as the non-hydrostatic tests, with the only difference being that the axial confining stress and radial confining stress are the same. In a similar way, these tests are carried out for six confining stresses as shown in Table 3.

The permeability results for non-hydrostatic and hydrostatic tests are presented in Table 2 and Table 3, respectively.

Table 2. Mean and standard deviation of permeability ($\times 10^{-15}$ m^2) data for non-hydrostatic tests.

Pore Pressure	**Confining st ess (MPa)**							
(MPa)	9.7	11.0	12.4	13.8	19.3	22.1	24.8	27.6
6.9	111±0.3	139±0.2	138±0.2	138±0.3	133±0.2	134±0.2	130±0.2	127±0.3

Table 3. Mean and standard deviation of permeability ($\times 10^{-15}$ m^2) data for hydrostatic tests.

Pore Pressure	**Confining st ess (MPa)**					
(MPa)	3.4	6.9	10.3	13.8	20.7	27.6
2.1	108±0.3	109±0.3	108±0.3	108±0.3	107±0.4	106±0.3

Poroelastic Model

This model describes a single phase flow of a slightly compressible fluid in a porous medium with linear elastic deformation (Díaz-Viera *et al.* (2020)). The rock deformation is described by a quasi-steady state moment equilibrium equation. The influence of the fluid is explained through the concept of effective stress due to Terzaghi (1923, 1925) and Biot (1941, 1955). The total stress acting on a porous medium is supported by both the solid matrix and the saturating fluid. The effective stress represents the part of the total stress supported by the solid matrix and can be determined as a function of deformation.

The model considers an isothermal system composed by one fluid and one solid, each consisting of a single component. The solid phase is a deformable porous medium fully saturated by the fluid, which is assumed Newtonian. Both, fluid and solid are slightly compressible. The solid phase is at rest, only displacements caused by mechanical stresses are present. Also, the solid has a linear elastic behavior and satisfies the Hooke's law for its constitutive stress-strain relationship.

The poroelasticity equation system consist of a momentum and a mass balance equation derived by Biot (1941, 1955). Here the model formulation follows Showalter (2000) notation. The monophasic flow model corresponds to a deformable linear elastic porous medium and it is formulated by Biot (1955); Chen *et al.* (2004).

$$\frac{\partial}{\partial t}(c_0 p + \alpha \nabla \cdot \omega) - \nabla\left(\frac{k}{\mu}\cdot\nabla p + \rho g \nabla z\right) = q_f \quad , \tag{1}$$

where c_0 is the storage coefficient, p is the fluid pressure, also known as pore pressure, α is the Biot-Willis coefficient (Biot and Willis (1957)) with $0 \leq \alpha \leq 1$, $\boldsymbol{\omega}$ is the displacement vector, $\boldsymbol{k}$ is the permeability tensor, μ is the fluid viscosity, ρ is the fluid density, g is the gravity acceleration, z is the elevation and q_f is the fluid source term.

The storage coefficient c_0 is defined as

$$c_0 = (\alpha - \phi)\, c_r + \phi c_f \tag{2}$$

where ϕ is the porosity, c_r is the solid grain compressibility and c_f is de fluid compressibility.

The quasi-stationary momentum balance equation for a porous medium saturated with a fluid is

$$-\nabla\cdot(\sigma_e-\alpha p\boldsymbol{I})=\rho_e g\nabla z \tag{3}$$

where $\sigma_T=\sigma_e-\alpha p\boldsymbol{I}$ is the total stress tensor and σ_e is the effective stress tensor. While ρ_e is an effective density defined as $\phi\rho+(1-\phi)\rho_s$, being ρ_s the rock density.

In particular, the effective stress tensor according to Hooke's law for the linear homogenous and isotropic case can be expressed as

$$\sigma_e=(\lambda+G)\nabla(\nabla\cdot\omega)+G\nabla^2\omega \tag{4}$$

where G and λ are the shear modulus and first Lamè constant, respectively. Note that the porosity and the absolute permeability tensor can be function of pore pressure (p), displacements (ω), volumetric strain (ε_v) or other quantities. Here, the solid mechanics sign convention is considered, which means that compressive stresses are negative and tensile stresses are positive.

The poroelasticity problem consists in solving Eqs. (1) and (3), and the unknowns are pore pressure (p) and the displacement (ω). The initial and boundary conditions are

Initial conditions

$$p(x,t_0)=p_0(x),\quad \forall x\in\Omega,\quad t=t_0 \tag{5}$$

$$\omega(x,t_0)=\omega_0(x),\quad \forall x\in\Omega,\quad t=t_0 \tag{6}$$

where p_0 and w_0 are initial values for pore pressure and displacement, respectively.

Boundary conditions

$$\omega(x,t)=\omega_\partial(x,t),\quad \forall x\in\partial_D^{\omega}\Omega\quad t>t_0 \tag{7}$$

$$\sigma_T(x,t)\cdot n=T_\partial(x,t),\ \forall x\in\partial_D^{\omega}\Omega\ t>t_0 \tag{8}$$

$$p(x,t)=p_\partial(x,t),\ \forall x\in\partial_D^{p}\Omega\ t>t_0 \tag{9}$$

$$u(x,t)\cdot n=u_\partial(x,t)\cdot n,\quad \forall x\in\partial_N^{p}\Omega\quad t>t_0 \tag{10}$$

where ω_∂, T_∂, p_∂ and u_∂ are displacement, traction, pressure and fluid flow at the boundary, respectively. Here, Ω is a bounded domain with boundary $\partial\Omega$ formed by two parts, one with Dirichlet conditions $\partial_D\Omega$ and the other with Neumann conditions $\partial_N\Omega$, where $\partial\Omega=\partial_D\Omega\cup\partial_N\Omega$ and $\partial_D\Omega\cap\partial_N\Omega=\emptyset$.

The fluid flow is expressed by the Darcy's law

$$u = -\frac{k}{\mu}\cdot(\nabla p + \rho g \nabla z) \tag{11}$$

where $\boldsymbol{u}$ is the Darcy velocity.

The numerical model is implemented using the module *PDE, Coefficient Form* in COMSOL Multiphysics (2018).

Numerical simulations

In this section, the numerical simulations of two case studies corresponding to non-hydrostatic and hydrostatic compression tests are presented. In both cases, the effect of the stresses on the petrophysical properties (permeability and porosity) is studied. To this purpose the previous poroelastic model is applied together with constitutive relationships for porosity and permeability in term of stress.

Porosity-stress relationship

Here, the porosity as a function of stress, proposed by Mainguy and Longuemare (2002) and described by Coussy (2004) is used. It provides a porosity relationship in terms of the volumetric strain (ε_v) and pore pressure (p) as follows

$$\phi=\phi_0+\alpha(\varepsilon_v-\varepsilon_{v0})+c_s\,(\alpha-\phi_0)(p-p_0) \tag{12}$$

where ϕ_0, ε_{v0} and p_0 are initial porosity, volumetric strain and pore pressure, respectively.

Permeability-stress relationship

The permeability-stress relationship used in this work is given in terms of volumetric strain (ε_v) and pore pressure (p), as follows

$$k = k_0\,[1+\beta_1\,(\varepsilon_v-\varepsilon_{v0})+\beta_2\,(p-p_0)] \tag{13}$$

where $\boldsymbol{k_0}$, $\boldsymbol{\varepsilon_{v0}}$ and $\boldsymbol{p_0}$ are initial permeability, volumetric strain and pore pressure, respecttively, and β_1 and β_2 are fitting parameters as in the previous work by Vadillo-Sáenz *et al.* (2020a), where it was shown that the frequently used permeability relationships can be approximated by a linear stress relationship. Accordingly, porosity and permeability, in Eq. (12) and (13) are linear functions of volumetric strain and pore pressure, respectively.

It should be mentioned that the fluid compressibility ($\boldsymbol{c_f}$), fluid density ($\boldsymbol{\rho}$), solid density (ρ_s), maximum flow rate ($\boldsymbol{Q_{max}}$), bulk modulus solid ($\boldsymbol{K_s}$), drained Young modulus ($\boldsymbol{E}$), drained Poisson's ratio ($\boldsymbol{\nu}$), Biot-Willis coefficient (α), rock compressibility ($\boldsymbol{c_s}$), drained bulk modulus ($\boldsymbol{K}$), first Lamé constant ($\boldsymbol{\lambda}$) and shear modulus ($\boldsymbol{G}$) are all kept constant during the numerical simulation.

In the Figure 4 a schematic representation of the boundary conditions for the hydrostatic and non-hydrostatic tests are shown.

All equations are discretized using a standard finite element method in space, and the Euler's backward finite difference method for time discretization, what gives place to a fully implicit scheme.

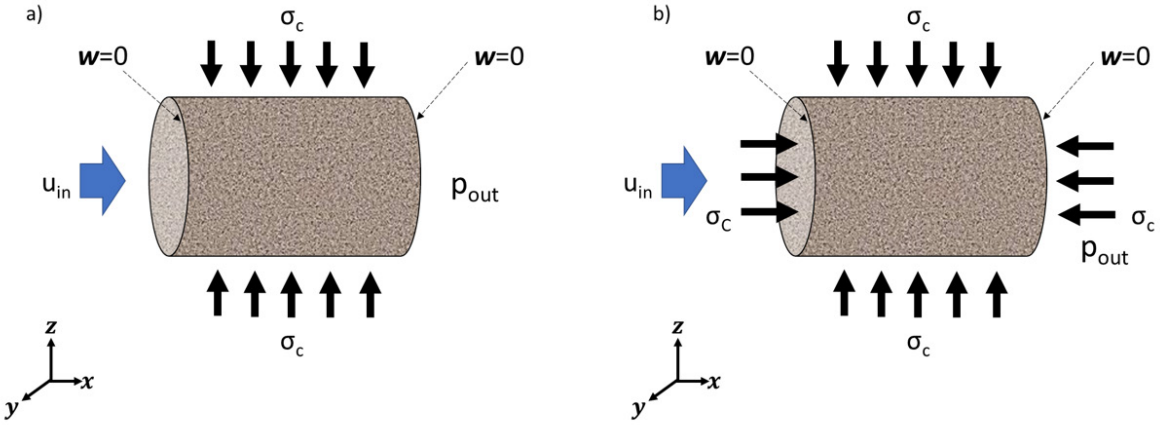

Figure 4. Schematic view of the boundary conditions: (a) the non-hydrostatic case, where $\omega_r = \omega_x = 0$ at the end faces and (b) the hydrostatic case, where ω_r=0 at the end face. Fluid is injected at constant flow rate from the left side, while pressure is set constant at the right side.

The finite element method is applied by using quadratic Lagrange elements in an unstructured triangular/tetrahedral mesh in 2D/3D. The resulting linear algebraic system is solved by the LU direct method UMFPACK for non symmetric and sparse matrices. The Newton-Raphson method is applied when the problem becomes non-linear.

The numerical model was implemented in COMSOL Multiphysics (COMSOL Multiphysics, 2018) and it was validated by comparing the numerical solution with the anaytical solution of the classical Mandel consolidation problem (Mandel, 1953; Abousleiman *et al.*, 1996). A more datailed description of the problem and its validation are given in Vadillo-Sáenz *et al.* (2020a).

Case study A: Non-hydrostatic Compression Tests Simulation.

The initial conditions for pore pressure is set equal to the outlet pressure ($p_0 = p_{out}$) and zero for displacement ($\omega_0 = 0$), respectively. The core is subjected to a constant pore pressure of 6.9 MPa and the radial confining stress sequence shown in Table 2, each for a time period of 40 min. The left and right sides are fixed, i.e. non-displacement in both radial and axial directions.

The problem is solved numerically by considering a 3D cylindrical domain with radius R = 0.051 m and length L=0.127 m as displayed in Figure 4 and Table 1. The domain is partitioned by an unstructured mesh of 2,420 tetrahedral elements. The simulation data for the non-hydrostatic compression tests are given in the Table 4.

On evaluating permeability by Eq. (13) each confinement stress, a fitting procedure to match the experimental pressure drop was carried out. The parameter β_1 best fit value is 30 with a very little variation in a range of ±5, while the parameter β_2 is practically insensitive with a best fitting value of 1×10^{-8} Pa^{-1} for all cases. Figure 9 in Appendix A shows the best fit obtained at each confining stress for non-hydrostatic compression tests.

The porosity and permeability simulation results for the non-hydrostatic compression tests are displayed in Figures 5 and 6, respectively. The porosity change (Figure 5) corresponds to the physically

expected behavior when subjecting a core to increasing confining stress. A reduction of approximately 1% of the porosity in the core is shown. It is important to notice that no measurements of porosity were made, it is only evaluated through Eq. (12). It could be observed in Figure 6 that the general trend shows the expected behavior of a core subjected to a increased confining stress except for the value at confining stress 19.3 MPa. It is also seen in Figure 6 that all numerical results (brown diamonds) fall within the boxplot of each test except in the aforementioned point. A core permeability reduction of approximately 8% at the end of the non-hydrostatic compression tests is observed. The simulated permeability values versus the experimental data give an acceptable RMS fitting error of 0.125.

Table 4. Non-hydrostatic compression tests data. Asterisk (*) means that the median value of the equilibrium flow rate was taken.

Parameter	Value	Unit
Fluid compressibility (c_f)	4×10^{-10}	1/Pa
Fluid density (ρ)	1000	kg/m^3
Solid density (ρ_s)	2530	kg/m^3
Confining stress (σ_c)	12.4	MPa
Maximum flow rate (Q_{max})	15	ml/min
Bulk modulus solid (K_s)	14.4	GPa
Drained Young modulus (E)	16.1	GPa
Initial porosity (ϕ_0)	13.63	%
Initial permeability (k_0)	1.39×10^{-13}	m^2
Outlet pressure (p_{out})*	6.67	MPa
Drained Poisson's ratio (ν)	0.15	-
Coreholder temperature	295.78	K
Time to reach flow steady state Q_{max} (t_s)	20	min
Fluid viscosity (μ)	9.4×10^{-4}	Pa·s
Biot-Willis coefficient (α)	0.47	-
Rock compressibility (c_s)	6.93×10^{-11}	1/Pa
Drained bulk modulus (K)	7.61	GPa
First Lam´e constant (λ)	2.98	GPa
Shear modulus (G)	6.95	GPa

Case Study B: Hydrostatic Compression Tests Simulation

In the hydrostatic case, the in Table 3 given confining stress sequence is applied for 50 min time period while keeping to all sample faces at a constant pore pressure of 2.1 MPa. Both left and right core sides are subjected to a non-displacement condition in the radial direction only ($\omega_r = 0$), the rest of the initial and boundary conditions are the same as in case A. The system domain is a 3D cylinder of radius R = 0.051 m and length L = 0.128 m.

Figure 4 and Table 1. The mesh is made up of 2,440 tetrahedral elements. The values of the parameters that are different from case A are given in the Table 5.

In the same way as in the non-hydrostatic compression tests Eq. 12 was used to estimate the dependence of rock porosity as a function of stress. The final results obtained for the non-hydrostatic

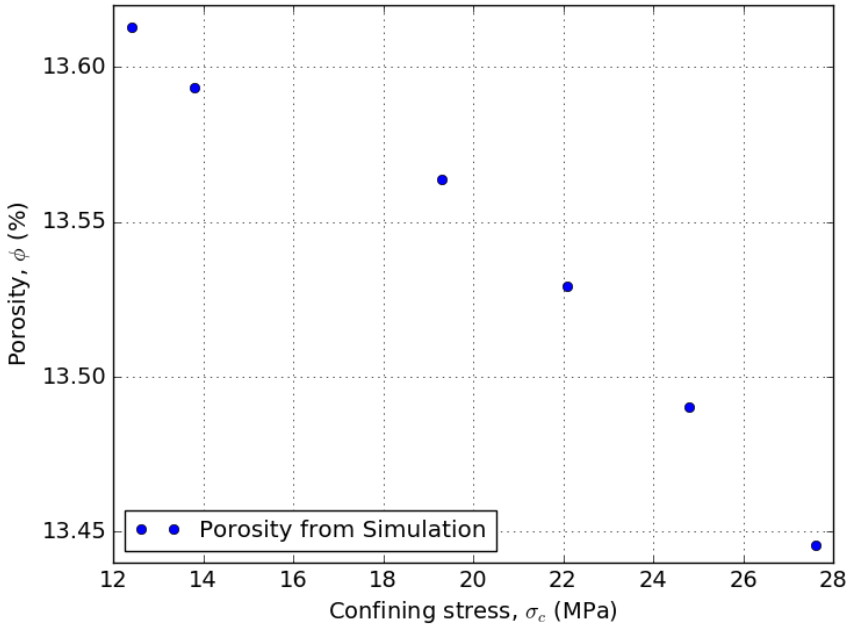

Figure 5. Porosity versus confining stress in case A non-hydrostatic tests.

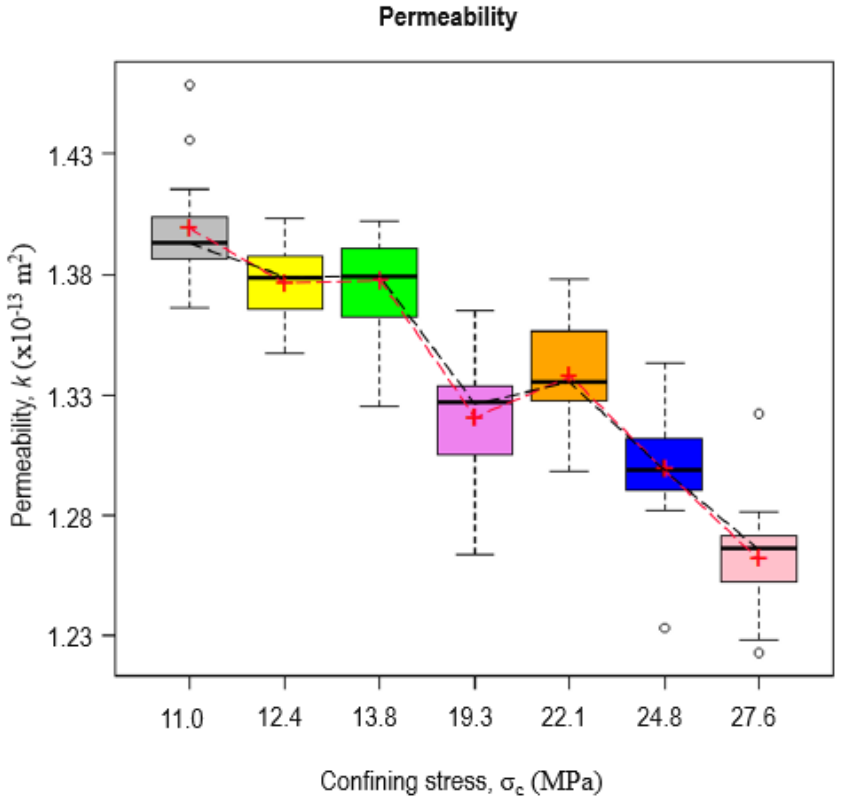

Figure 6. Boxplots of permeability versus confining stress in Case A non-hydrostatic tests. The simulation results are displayed as brown diamonds, the median experimental data values are displayed as a black line, and the mean experimental data are displayed as red crosses

Table 5. Hydrostatic compression tests data. Asterisk (*) means that the median value of the equilibrium flow rate was taken.

Parameter	Value	Unit
Solid density (ρ_s)	2634	kg/m^3
Confining stress (σ_c)	10.3	MPa
Initial porosity (ϕ_0)	14.02	%
Initial permeability (k_0)	1.09×10^{-13}	m^2
Outlet pressure (p_{out})*	1.94	MPa
Coreholder temperature	294.5	K
Time to reach flow steady state Q_{max} (t_s)	36	min
Fluid viscosity (μ)	9.5×10^{-4}	Pa·s

compression tests are displayed in Figure 7. The porosity change shows the physically behavior expected for a core subject to an increasing confinement stress. A reduction of approximately 1% of the porosity in the core is estimated.

The best β_1 fit value is 20 with small variations near ±5. The β_2 parameter is practically insensitive, taking in all cases its best fit value at 1×10^{-8} Pa^{-1}, for all cases. The Figure 10 in Appendix A shows best fit values obtained in the hydrostatic tests.

The results displayed in Figure 8 show the physically expected behavior in a core subjected to an increasing confining stress. No values outside of the general trend appear. A reduction of approximately 2% of the permeability in the core at the end of the hydrostatic tests is observed. A difference between the experimental permeability data and the simulation results of 0.844 RMS error is seen.

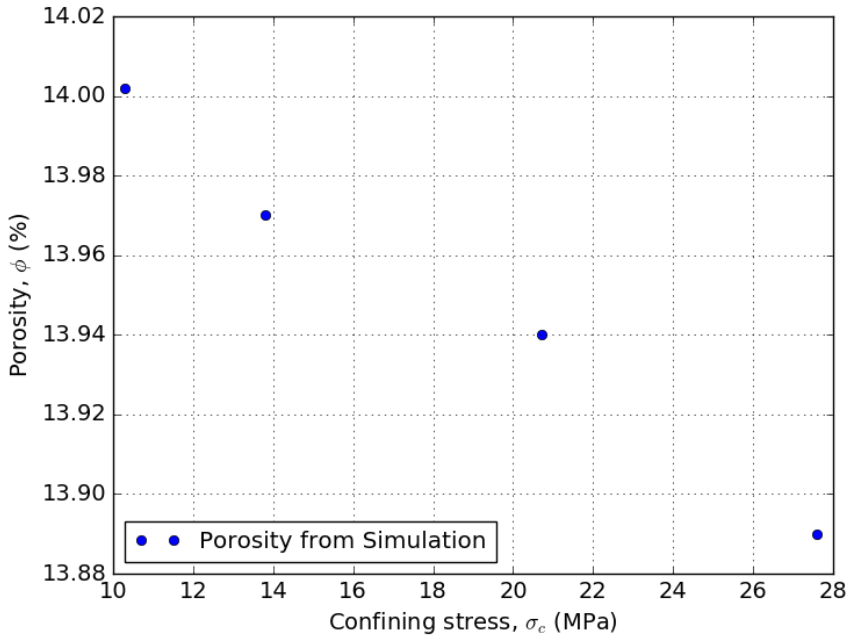

Figure 7. Porosity versus confining stress in case B hydrostatic tests.

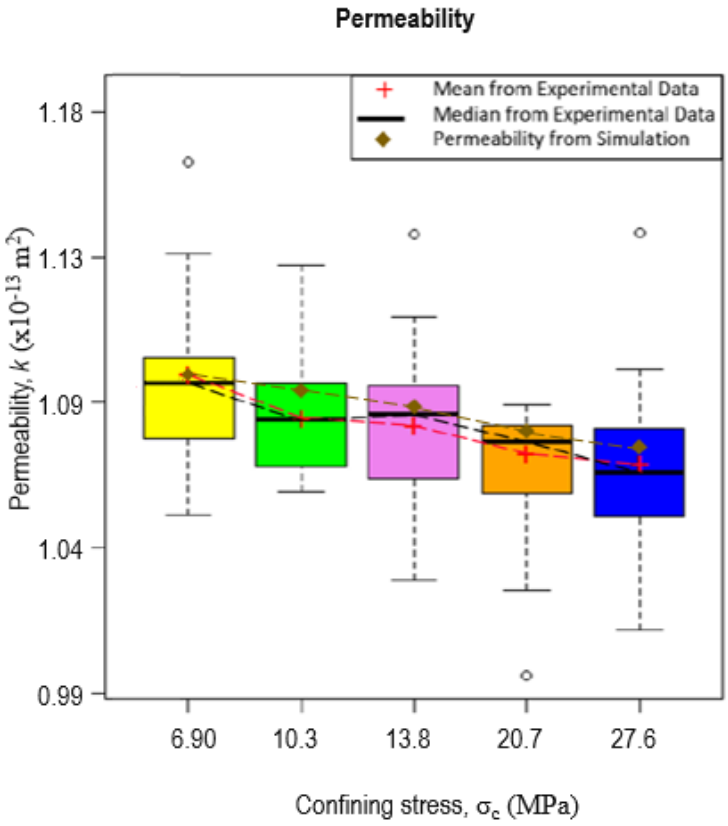

Figure 8. Boxplots of permeability versus confining stress for Case B hydrostatic tests. The simulation results are displayed as brown diamonds, the median experimental data values are displayed as a black line, and the mean experimental data are displayed as red crosses.

Conclusions

Permeability experimental results in terms of volumetric strain and pore pressure in Bedford limestone cores for hydrostatic (low shear stresses) and non-hydrostatic (high shear stresses) tests, in the elastic range have been here presented. Also, a mathematical model has been shown to describe the effect of the confinement stress on rock porosity and permeability by considering single-phase flow and elastic rock response. The main results and conclusions are:

The literature review shows that multiple experimental results on the effect of confinement stress on permeability in sandstone rocks have been reported, but only few tests in carbonate rocks have been performed, despite its relevance. It was found in the present work, that permeability in Bedford limestone is more sensitive to stress than sandstones.

The effect of stress on permeability is clearly stronger when higher shear stresses are present (non-hydrostatic tests), than when small shear stresses are applied (hydrostatic tests). In the linear confining stress range analyzed, from 10 to 28 MPa, the non-hydrostatic case gives a reduction of 8% (with a pore pressure of 6.9 MPa) and in the hydrostatic case gives place to only 2% (with a pore pressure of 2.1 MPa). The above behavior could be explained by noticing that shear stresses can lead to large pore spaces reductions, probably due to a better rearrangement and closure of the internal porous structure of the Bedford limestone, which is made up of highly irregular grains.

There are very few studies published in the literature in which both experimental tests and numerical simulation results of the change in permeability as a function of stress are presented. For this

purpose, a in-house mathematical and computational model has been developed. The few experimental published tests that include modeling employ, third-party software whose operation and results interpretation is not entirely clear.

The model used to analyze the pressure drop experimental data involves fitting parameters permeability-stress correlation model (Eq. 13). The data fitting achieved has been excellent. This indicates that the mathematical model developed describes adequately the phenomenon.

Based on the results here obtained, this work provides useful information for formulating and validating constitutive models for the flow-stress dependence in homogeneous and isotropic poroelastic media. Larger data fitting differences could be expected when working with deformable fractured porous media.

Acknowledgements

This work is partially supported by the Fondo Sectorial Sener-Conacyt-Hidrocarburos through the Geomechanics Network Project 280097 (2017 - 2022) in a joint collaboration between the Mexican Petroleum Institute, the University of Alberta and Pemex.

Referencess

Abousleiman, Y., Cheng, A. H.-D., Cui, L., Detournay, E., and Roegiers, J.-C. (1996). Mandel's problem revisited. *Geotechnique*, 46(2):187–195.

Agheshlui, H., Sedaghat, M. H., and Matthai, S. (2018). Stress influence on fracture aperture and permeability of fragmented rocks. *Journal of Geophysical Research: Solid Earth*, 123(5):3578–3592.

Al-Quraishi, A. A., Almisned, O. A., and Al-Awad, M. N. (2010). Relative permeabilities of homogeneous and heterogeneous laminated rock samples under hydrostatic and triaxial stresses. *Journal of King Saud University - Engineering Sciences*, 22(2):101–109.

Bai, M., Meng, F., Elsworth, D., Zaman, Z., and Roegiers, J. (1997). Numerical modeling of stress-dependent permeability. *International Journal of Rock Mechanics and Minings Sciences*, 34(3-4). Proceedings of the 1997 36th US Rock Mechanics ISRM International Symposium ; Conference date: 29-06-1997 Through 02-07-1997.

Barthlmy, J.-F. (2009). Effective permeability of media with a dense network of long and micro fractures. *Transport in Porous Media*, 76:153–178.

Bear, J. (1972). *Dynamics of fluids in porous media.* Environmental science series. Elsevier.

Belmokhtar, M., Delage, P., Ghabezloo, S., Tang, A.-M., Menaceur, H., and Conil, N. (2017). Poroelasticity of the Callovo-Oxfordian Claystone. *Rock Mechanics and Rock Engineering*, 50(4):871–889.

Biot, M. and Willis, D. (1957). The elastic coefficients of the theory of consolidation. *Journal of Applied Mechanics ASME*, 24:594 – 601.

Biot, M. A. (1941). General theory of three-dimensional consolidation. *Journal of Applied Physics*, 12(2):155–164.

Biot, M. A. (1955). Theory of elasticity and consolidation for a porous anisotropic solid. *Journal of Applied Physics*, 26:182 – 185.

Brace, W. F. (1965). Some new measurements of linear compressibility of rocks. *Journal of Geophysical Research* (1896-1977), 70(2):391–398.

Carman, P. C. (1956). *Flow of gases through porous media*. Butterworths Scientific Publications London.

Chen, Z., Lyons, S., and Qin, G. (2004). The mechanical behavior of poroelastic media saturated with a newtonian fluid derived via homogenization. *International Journal of Numerical Analysis and Modeling*, 1:75 – 98.

COMSOL Multiphysics (2018). Reference manual, version 5.4. *COMSOL AB*.

Coronado, M. (2019). Informe Final de la Etapa 2. *Technical Report. Proyect 280097 (IMP Y.61066). Fondo Sectorial Conacyt-Sener-Hidrocarburos, Mexican* Petroleum Institute, Mexico City.

Coussy, O. (2004). *Poromechanics*. John Wiley and Sons, Chichester, England, first edition.

Cui, L. and Abousleiman, Y. (2001). Time-dependent poromechanical responses of saturated cylinders. *Journal of Engineering Mechanics*, 127(4):391–398.

David, C., Wong, T.-F., Zhu, W., and Zhang, J. (1994). Laboratory measurement of compaction-induced permeability change in porous rocks: Implications for the generation and maintenance of pore pressure excess in the crust. *Pure and applied geophysics*, 143:425–456.

Díaz-Viera, M., Aguilar-Gastelum, P., Coronado, M., Vadillo-Sáenz, M., and Wilson- García, E. (2020). Modelo matemático, numérico y computacional de poroelasticidad monofásico. *Internal Report of th Fondo Sectorial Conacyt Sener Hidrocarburos Project 280097 (IMP-Y.61066) October 15, 2020*.

Ferronato, M., Castelletto, N., and Gambolati, G. (2010). A fully coupled 3-d mixed finite element model of biot consolidation. *Journal of Computational Physics*, 229(12):4813 – 4830.

Fortin, J., Schubnel, A., and Guguen, Y. (2005). Elastic wave velocities and permeability evolution during compaction of bleuswiller sandstone. *International Journal of Rock Mechanics and Mining Sciences*, 42:873–889.

Glowacki, A. and Seladurai, A. (2016). Stress-induced permeability changes in indiana limestone. *Engineering Geology*, 215(19):122–130.

Goral, J., Panja, P., Deo, M., Andrew, M., Linden, S., Schwarz, J.-O., and Wiegmann, A. (2020). Confinement effect on porosity and permeability of shales. *Scientific Reports*, 10.

Han, B., Xie, S. Y., and Shao, J. F. (2016). Experimental Investigation on Mechanical Behavior and Permeability Evolution of a Porous Limestone Under Compression. *Rock Mechanics and Rock Engineering*, 49:3425–3435.

Hoek, E. and Franklin, J. (1968). A simple triaxial cell for field and laboratory testing of rock. *Transactions of the Institution of Mining and Metallurgy*, 77:A22–26.

Huo, D. and Benson, S. (2016). Experimental investigation of stress-dependency of relative permeability in rock fractures. *Transport in Porous Media*, 113:567–590.

Jones, C. and Smart, B. (2002). Stress induced changes in two-phase permeability. In *SPE/ISRM Rock Mechanics Conference held in Irving, Texas, 20-23 October*, number SPE/ISRM 78155. Society of Petroleum Engineers.

Kozeny, J. (1927) U¨ ber kapillare Leitung des Wassers im Boden, Sitzb. *Akademie der Wissenschaften in Wien. Mathematisch-Naturwissenschaftliche Klasse*, 136:271–306.

Lamb, A. and Gorman, G. (2010). Finite element coupled deformation and fluid flow in fractured porous media. In *SPE EUROPEC/EAGE Annual Conference and Exhibition held in Barcelona, Spain, 1417 June 2010*, number SPE-131725. Society of Petroleum Engineers.

Li, P., Chalaturnyk, R., and Polikar, M. (2004). Issues with reservoir geomechanical simulation of the sagd process. *Journal of Canadian Petroleum Technology*, 43(1):1–11.

Lion, M., Skoczylas, F., and Ledesert, B. (2004). Determination of the main hydraulic and poro-elastic properties of a limestone from bourgogne, france. *International Journal of Rock Mechanics and Mining Sciences*, 41:915–925.

Ma, F., He, S., Zhu, H., Xie, Q., and Jiao, C. (2012). The effect of stress and pore pressure on formation permeability of ultra-low-permeability reservoir. *Petroleum Science and Technology*, 30(12):1221–1231.

Ma, J. (2015). Review of permeability evolution model for fractured porous media. *Journal of Rock Mechanics and Geotechnical Engineering*, 7:351–357. Peer review under responsibility of Institute of Rock and Soil Mechanics, Chinese Academy of Sciences.

Mainguy, M. and Longuemare, P. (2002). Coupling fluid flow and rock mechanics: Formulation of the partial coupling between reservoir and geomechanical simulators. *Oil & Gas Science and Technology*, 57(4):355–367.

Mandel, J. (1953). Consolidation des sols (´etude mathématique). *Geotechnique*, 30:287 – 299.

McPhee, C., Reed, J., and Zubizarreta, I. (2015). *Core Analysis: A Best Practice Guide*. ISSN. Elsevier Science.

Ojagbohunmi, S., Chalaturnyk, R., and Leung, J. (2012). Coupling of stress-dependent relative permeability and reservoir simulation. *In Eighteenth SPE Improved Oil Recovery Symposium held in Tulsa*, Oklahoma, USA, 1418 April 2012.

Philips, O. (1991). Flow and reactions in permeable rocks. *Cambridge University Press*, Cambridge, UK.

Ramos da Silva, M., Schroeder, C., and Verbrugge, J.-C. (2010). Poroelastic behavior of a water-saturated limestone. *International Journal of Rock Mechanics and Mining Sciences*, 47:797–807.

Rinaldi, A. P. and Rutqvist, J. (2016). Modeling stress/strain-dependent permeability changes for deep geoenergy applications. In *EGU General Assembly Conference Abstracts*, EGU General Assembly Conference Abstracts, pages EPSC2016–15108.

Roded, R. and Holtzman, R. (2017). Reactive transport under stress: Permeability evolution by chemo-mechanical deformation. In *AGU Fall Meeting Abstracts*, volume 2017, pages H43G–1725.

Sangnimnuan, A., Li, J., and Wu, K. (2018). Development of efficiently coupled fluid- flow/geomechanics model to predict stress evolution in unconventional reservoirs with complex-fracture geometry. *SPE Journal*, pages 640–660.

Sasaki, T. and Rutqvist, J. (2021). Estimation of stress and stress-induced permeability change in a geological nuclear waste repository in a thermo-hydrologically coupled simulation. *Computers and Geotechnics*, 129:103866.

Selvadurai, A. and Selvadurai, P. (2010). Surface permeability test: experiments and modelling for estimating effective permeability. *Proceedings of the Royal Society A*, 466:2819– 2846.

Showalter, R. E. (2000). Diffusion in Poro-Elastic Media. *Journal of Mathematical Analysis and Applications*, 251(1):310–340.

Takahashi, M., Park, H., Takahashi, N., and Fujii, Y. (2013). True triaxial tests - using permeability and extensional stress parameters to simulate geological history in rocks. *Geosystem Engineering*, 16(1):75–82.

Terzaghi, K. (1923). Die Berechnung der Durchlassigkeitsziffer des Tones aus dem Verlauf der Hydrodynamichen Spannungserscheinungen Akademie der Wissenschaften in Wien. *Mathematish-Naturwissen-Schaftiliche Klasse*, 132:125–138.

Terzaghi, K. (1925). *Erdbaumechanik auf Bodenphysikalischen Grundlagen*. Leipzig u. Wien, F. Deuticke.

Touhidi-Baghini, A. (1998). *Porosity reduction and crustal pore pressure development*. PhD thesis, Department of Civil Engineering, University of Alberta.

Vadillo-Sáenz, M., Aguilar-Gastelum, P., Díaz-Viera, M., and Coronado, M. (2020a). Permeability simulation in an elastic deformable sandstone under stress changes. *Suplemento de la Revista Mexicana de Física*.

Vadillo-Sáenz, M., Díaz-Viera, M., Coronado, M., and Aguilar-Gastelum, P. (2022). An analysis of standard permeability stress - dependent relationships in homogeneous elastic porous media. *Journal of Rock Mechanics and Geotechnical Engineering (submitted)*.

Vadillo-Sáenz, M., Domínguez-Torres, A., Díaz-Viera, M., Serrano-Saldaña, E., and Coronado, M. (2020b). Modelado de pruebas de flujo con deformación en roca caliza Bedford. *Internal Report of th Fondo Sectorial Conacyt Sener Hidrocarburos Project 280097 (IMP-Y.61066) October 15, 2020.*

Walder, J. and Nur, A. (1984). Porosity reduction and crustal pore pressure development. *Journal of Geophysical Research: Solid Earth*, 89(B13):11539–11548.

Wang, F., Sun, Z., Liu, H., Xu, T., and Jing, J. (2016). Experimental study on the variation of permeability of medium-fine feldspar-quartz sandstone low-permeability reservoir under the circulatory increasing or reducing conditions of confining pressure. *Geofluids*, 47:1125–1132.

Zhu, W., Montesi, L. G., and fong Wong, T. (1997). Shear-enhanced compaction and permeability reduction: Triaxial extension tests on porous sandstone. *Mechanics of Materials*, 25(3):199–214.

Zhu, W. and Wong, T.-f. (1997). The transition from brittle faulting to cataclastic flow: Permeability evolution. *Journal of Geophysical Research: Solid Earth*, 102(B2):3027–041.

Appendix A. Poroelastic Model Fitting of Hydrostatic and Non-Hydrostatic Compression Tests

In this appendix the fitting results of the experimental pressure drop data obtained from the non-hydrostatic and hydrostatic compression tests described in this paper are shown. They are graphically illustrated in Figures 9 and 10, respectively.

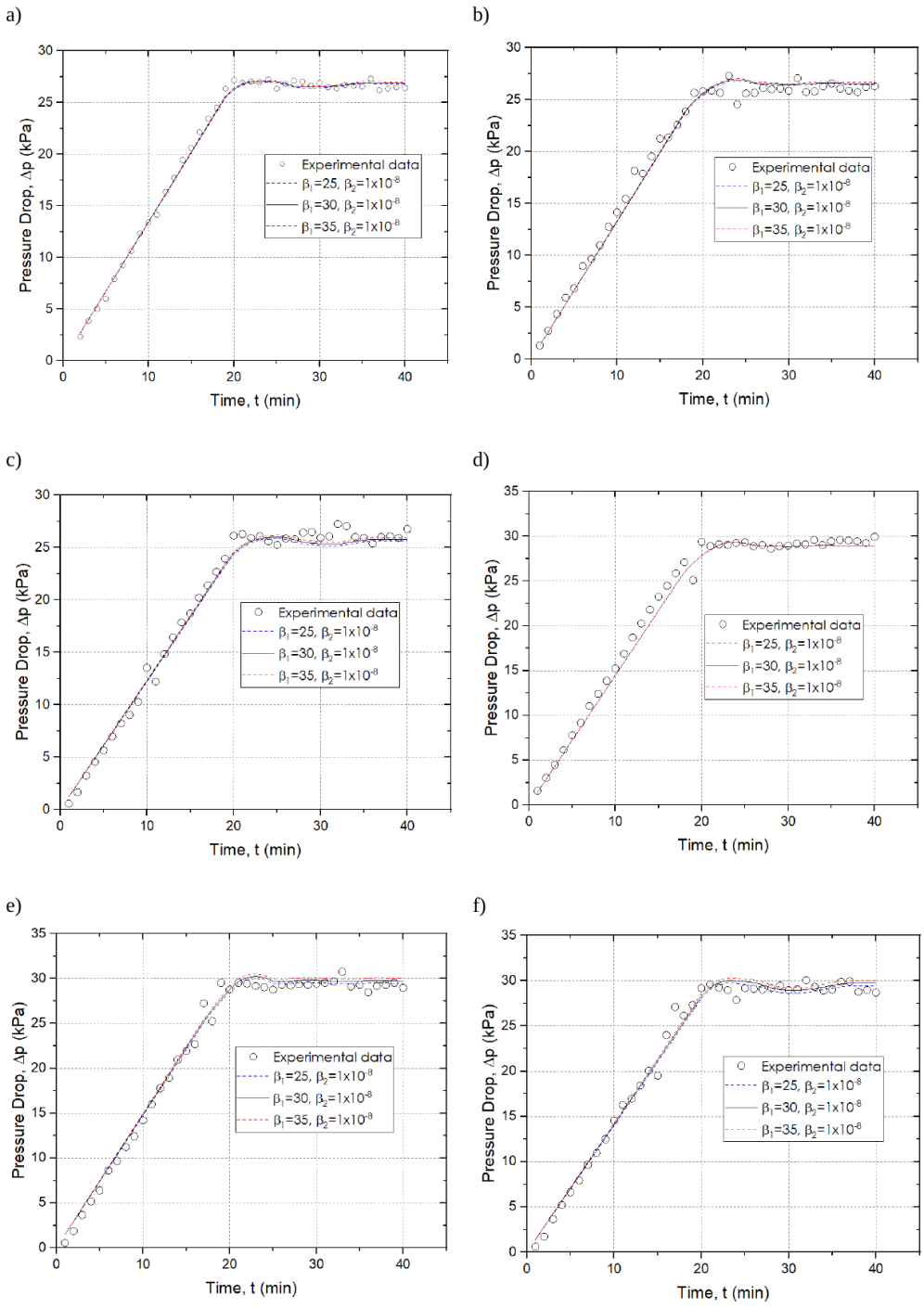

Figure 9. Pressure drop along the time for non-hydrostatic compression tests at confining stress: a) 12.4 MPa, b) 13.8 MPa, c) 19.3 MPa, d) 22.1 MPa, e) 24.8 MPa and f) 27.6 MPa. In hollow circles the experimental data and as broken lines the fitting curves corresponding to three different β_1 parameter values. Here, β_1 is dimensionless and β_2 has dimensions of 1/Pa.

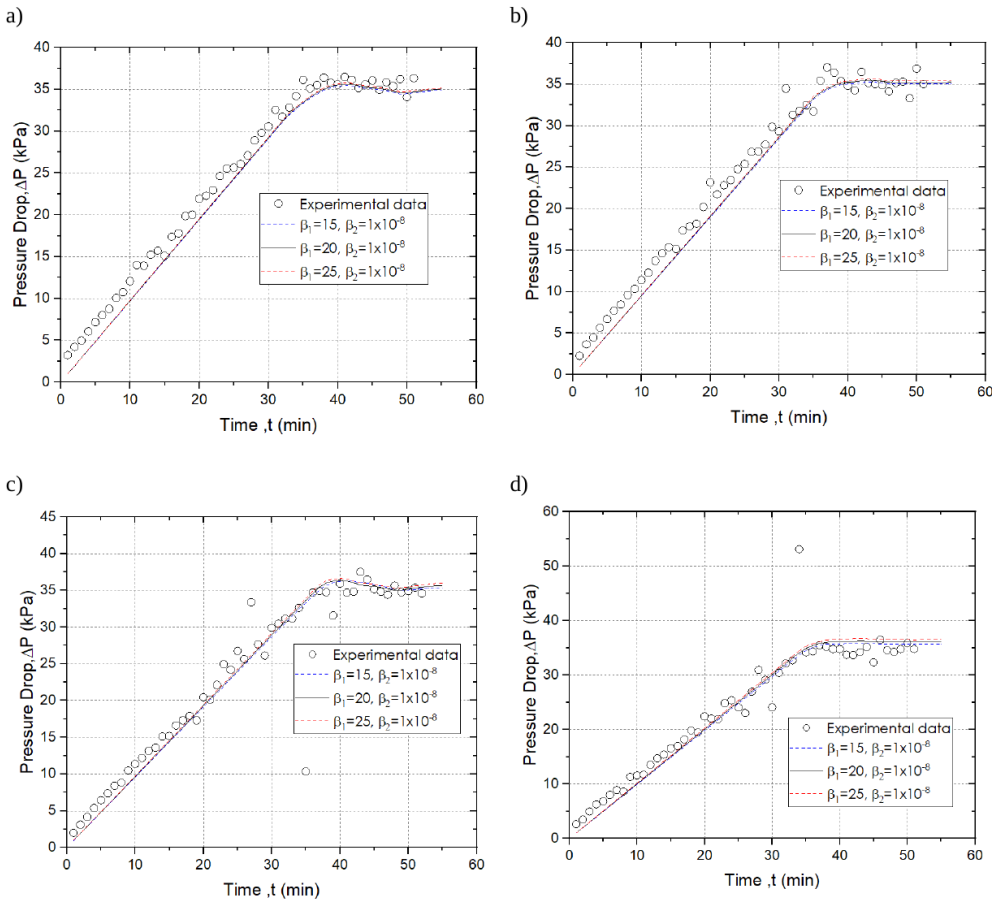

Figure 10. Pressure drop along the time for hydrostatic compression tests at confining stress: a) 10.3 MPa, b) 13.8 MPa, c) 20.7 MPa and d) 27.6 MPa. In hollow circles the experimental data and as broken lines the fitting curves corresponding to three different β_1 parameter values. Here, β_1 is dimensionless and β_2 has dimensions of 1/Pa.

Original paper

https://doi.org/10.22201/10.22201/igeof.00167169p.2022.61.3.2198

The Great 1822 Aleppo Earthquake: New Historical Sources and Strong Ground Motion Simulation

Ryad Darawcheh*[1], Mohamad Khir Abdul-Wahed[1] and Adnan Hasan[1]

Received: November 1, 2021; accepted: March 30, 2022; published on-line: July 1, 2022.

Resumen

El terremoto de 1822 fue devastador y se considera uno de los eventos relativamente recientes que azotaron el noroeste de Siria y las áreas cercanas del centro-sur de Turquía, es decir, en la unión del sistema de fallas del Mar Muerto con el sistema de fallas del este de Anatolia. En este trabajo, se vuelve a estudiar este terremoto, con base en nuevas fuentes de información originales contemporáneas y casi contemporáneas, que no habían sido citadas anteriormente. El análisis de estas fuentes revela lo siguiente: (1) se proporcionan descripciones más detalladas de los efectos del terremoto para las ciudades de Aleppo, Antakia y Latakia, y la identificación de seis nuevas ubicaciones afectadas; (2) evaluación de los parámetros pertinentes del terremoto, como el epicentro, la onda de superficie, las magnitudes de momento y la intensidad sísmica; (3) se muestra documentación de evidencias de una ola marina sísmica que ocurrió entre las costas chipriota y Siria, e (4) identificación de la falla de San Simeón, ubicada al oeste de Aleppo, como la probable falla causante. Además, el movimiento del suelo generado por el terremoto de 1822 ha sido simulado utilizando el método de estocástica extendida. Se generaron series temporales de aceleración y espectros de pseudoaceleración amortiguados para la ciudadela de Aleppo, donde la aceleración máxima del suelo, debido al terremoto, se estimó en 0.4 g. Los resultados contribuirán a actualizar la configuración de riesgo sísmico en el noroeste de Siria y el centro-sur de Turquía.

Palabras Clave: Terremotos históricos, terremoto de Aleppo de 1822, fuentes históricas de información y simulación del movimiento del suelo

Editorial responsibility: Luis Quintanar Robles

**Corresponding author at cscientific28@aec.org.sy*
[1]Atomic Energy Commission of Syria, Dept. of Geology P.O. Box 6091, Damascus, Syria

Abstract

The devastating 1822 earthquake is one of the relatively recent events that struck northwestern Syria and the nearby areas of central-southern Turkey, at the junction of the Dead Sea fault system with the Eastern Anatolian fault system. This earthquake is re-examined, in this work, based on new original contemporary and near contemporary sources of information not cited in previous literature. Analysis of these sources reveals the following: (1) more detailed descriptions of the earthquake effects are provided for cities of Aleppo, Antakia and Latakia, and the identification of six new locations affected; (2) assessment of relevant earthquake parameters such as the epicenter, surface-wave, moment magnitudes and seismic intensity; (3) documentation of evidences of a seismic sea wave that occurred between the Cypriot and the Syrian coasts and (4) identification of the Saint Simeon fault, located to west of Aleppo, as the probable causative fault. Furthermore, the ground motion generated by the 1822 earthquake has been simulated using the extended stochastic simulation method. Acceleration time series and damped pseudo acceleration spectra were generated for Aleppo Citadel, where the peak ground acceleration, due to the earthquake, has been estimated at 0.4 g. The results will contribute to updating the seismic hazard setting in the northwestern Syria and central-southern Turkey.

Key words: Historical earthquakes, The 1822 Aleppo earthquake, Historical sources of information and Ground motion simulation

Introduction

Investigation of historical large earthquakes is one of the most important seismological issues for understanding the long-term active tectonics within the context of earthquake hazard assessment. In addition, the quantification of the ground motions resulting from such strong earthquakes, where their recordings are not available, represents a necessary approach for earthquake engineering purposes (e.g. Honoré *et al.*, 2011).

Numerous well-documented, large historical earthquakes have occurred in northwestern Syria, that originated in the Dead Sea fault system (DSFS) (e.g. Sbeinati *et al.*, 2005). Among those past events is the earthquake of 13 August 1822, which occurred in northwestern Syria and the neighboring provinces in central-southern Turkey. This earthquake was descriptively and analytically included in numerous earthquake catalogues. The worldwide descriptive catalogue of R. Mallet and J.W. Mallet (1858: 140-42, 150-51) represents the first report of this earthquake, and some foreshocks and aftershocks, based on data provided by French journals such as the Annales de Chimie et de Physique, Le Moniteur, Journal des Débats and Journal des Voyages. Al-Ghunaim (2002), in his historical descriptive catalogue on earthquakes in the Arab countries, provided all Arabic accounts of the 1822 earthquake without giving his own interpretation for this earthquake. The last catalogue that listed this event is the historical parametric one compiled by Sbeinati *et al.* (2005) that presented damage in 29 localities, based on the work of Ambraseys (1989), the famous Aleppian historian Mohammad Ragheb Al-Tabbakh (Al-Tabbakh, 1925: 400-410), and the letter of the French consul in Aleppo Monsieur "Mathieu-Maximilien-Prosper de Lesseps- (1771-1832), dated on September 1822 (Archives des Affaires Étrangères, 1822, 176-181). Ambraseys is the first to provide an extensive description of the earthquake of 57 localities affected by this earthquake in Syria, Turkey, Cyprus and Lebanon, based on the numerous consular archives, contemporary accounts, and press

reports (Ambraseys, 1989; 2009). He later re-assessed the epicentral coordinates and the surface-wave magnitude (Ambraseys and Jackson, 1998). Table 1 lists a summary of the results of some previous works. Ambraseys (1989; 2009) emphasized that more work is required to fully understand this large earthquake and other similar events that struck the plate boundary between the Arabian and the Anatolian plates.

Recently, some preliminary results on the 1822 earthquake were presented by Darawcheh *et al.* (2019). In this paper, we return to the 1822 earthquake since numerous new and relevant original and contemporary sources of information have been found. Accordingly, the purpose of this paper is to: (1) resume the analysis of the new historical sources of the 1822 earthquake; (2) assess its new parameters in light of these new sources; (3) suggest the most probable causative fault of the earthquake. Also, it aims to produce ground motion simulation of the earthquake using the stochastic finite-fault method for a historical site in the damaged area. It is believed that the results of the paper represent additional contributions to the 1822 earthquake, not mentioned at the previous works.

Table 1. Parameters of the 13 August 1822 earthquake according to the previous works. Abbreviations: Ms: surface-wave magnitude; Io: epicentral maximum intensity; I_A: intensity at Aleppo city. 1822Am, 1822AmJ and 1822Sb are the symbols of epicenter shown in Figure 3.

Author(s)	Epicenter (Lat.-Long.)	Symbols on Fig. 3	Depth (h)	Ms	Io (Scale)	I_A
Ambraseys (1989)	36.70-36.90	1822Am	-	7.4 +	X (MSK)	VII-VIII
Ambraseys & Jackson (1998)	36.70-36.50	1822AmJ	-	7.5	-	-
Sbeinati *et al.* (2005)	36.10-36.75	1822Sb	18	7.0	IX (EMS-92)	VIII-IX

Pachalic of Aleppo

The earthquake of 1822 occurred during the Ottoman period in Syria. Aleppo (in Arabic Halab) was the capital of the state called the Pachalic of Aleppo (Pachalic is a province governed by a Pasha or Governor-General). According to the French orientalist Constantin-Françios Volney (1757-1820), who stayed in Aleppo from 1783 to 1784, the Pachalic extended from the Euphrates river to the Mediterranean Sea, between two imaginary lines; one drawn from the town of Iskenderun to the small town of Birecik; the other from the village of Balis to the Mediterranean Sea, by both towns of Maarrat Al-Nu'man and Jisr Al-Shughur (Figure 1). Administratively, this province includes numerous small towns such as Antioch (in Arabic Antakia), Iskenderun, Aintab, Idlib, Jisr Al-Shughur, Suwaydiyeh and Payas along with more than 3000 villages (Volney, 1788: 139).

Aleppo was the third largest city in the Ottoman Empire, in size and population, after Constantinople (now Istanbul) and Cairo. This city was one of the best built in the whole Ottoman Empire. Most of the houses are one-story built of hewn stone and there were numerous mosques; the Great Umayyad Mosque is the most important one. Aleppo has nine historical gates and is surrounded by a thick ancient wall built in the Mamlouk period. One of the more remarkable structures in the city is the medieval citadel, built after 1209 AD. (Talas, 1956). It has an elliptical shape and is built on a natural high hill. The city had many large squares, two-story khans (commercial courtyard

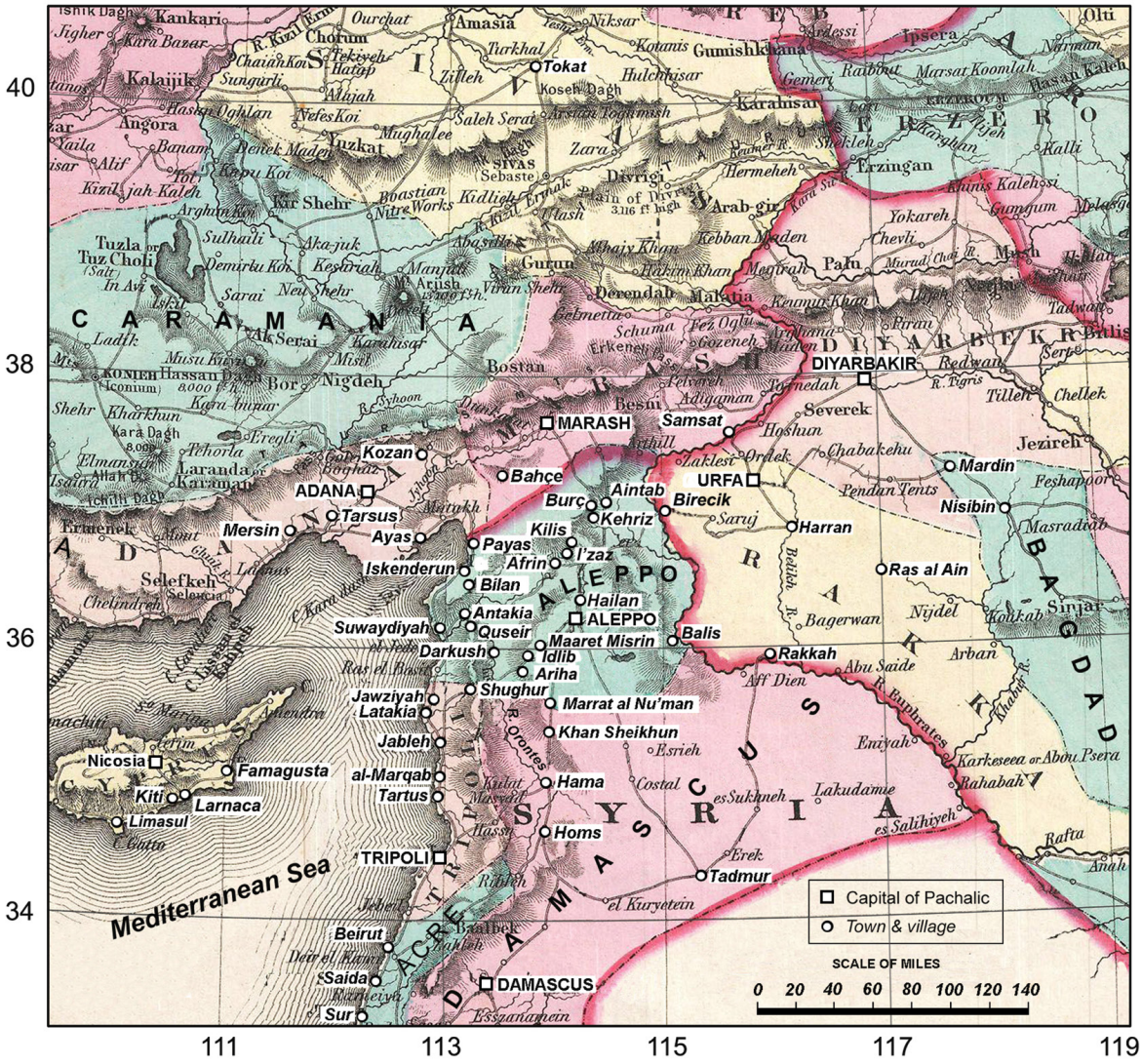

Figure 1. A geographical map of the Pachalics of the Ottoman Empire in and around Syria showing the location of Pachalic of Aleppo (modified after Colton, 1855:25).

buildings) and roofed long bazaars (market places). The river Quaiq that rises near Aintab runs westward of the city. The city was a large commercial center of the Levant and an important center of economic, cultural and political activities to the extent that many chroniclers, scholars, orientalists and travelers visited and lived here (Russell, 1794: 1-40; Conder, 1824: 274-297). In addition, many European states opened consulates and trading offices in Aleppo during the 16th and 17th centuries such as the consulates of Republic of Venice, France, England and the Dutch.

Most of the historical sources indicate that the population of Aleppo and its suburbs was about 200,000 at the beginning of the 19th century, including 20,000 Christians and several thousand Jews. Miller (1826: 22) mentioned that Aleppo had 40.000 houses. Figure 2 is a plan of Aleppo during the period 1811-1818. Although it contains inaccuracies and errors (e.g. direction of the citadel), the map has a large historical value as it includes the gates of Aleppo, quarters within the

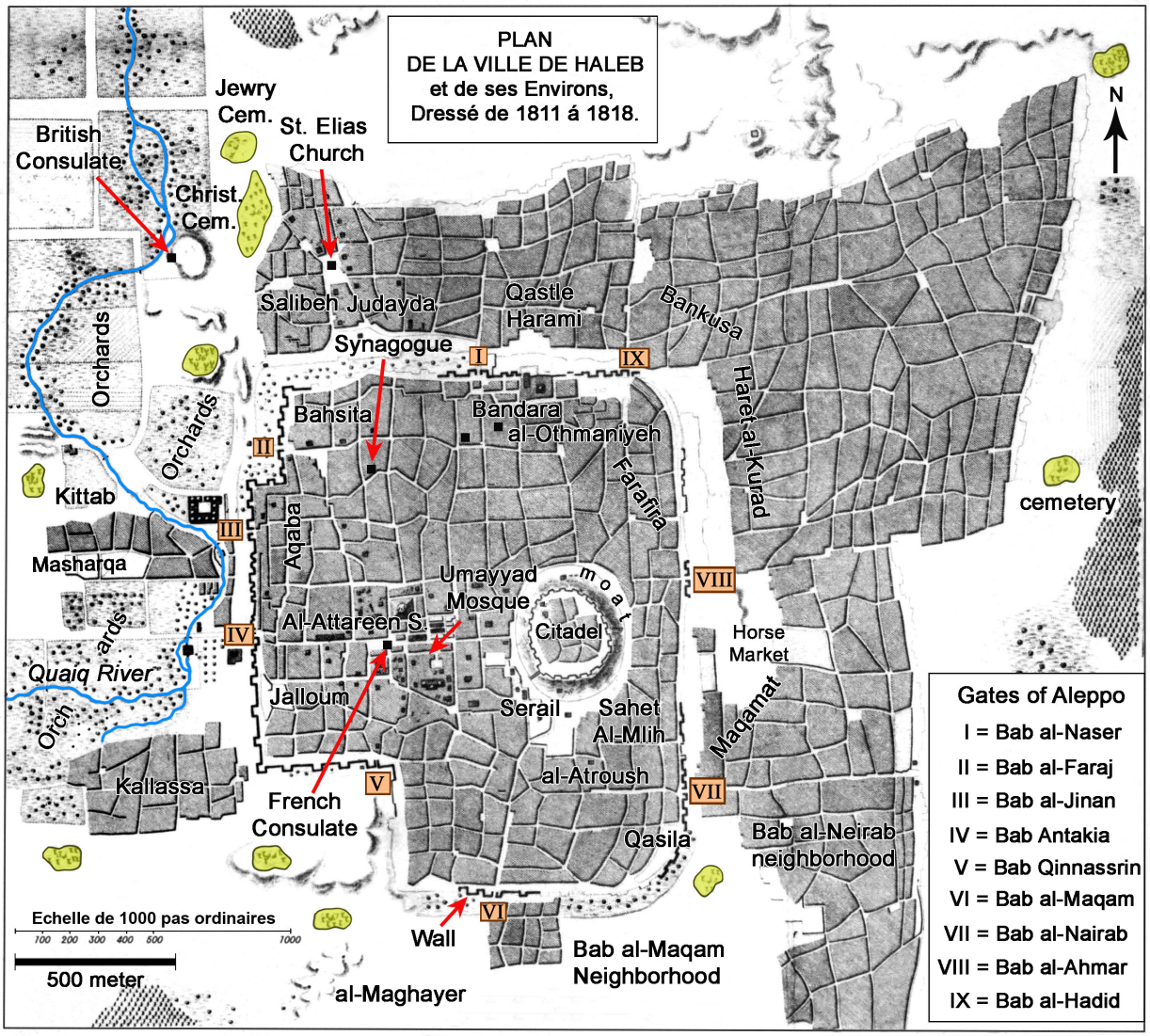

Figure 2. Plan of Aleppo city and its environs prepared during the period 1811-1818. The plan first established in 1811 by Vincent Germain, a European resident in Aleppo who was in the consul of France, then completed in 1818 by Jean-Baptist Rousseau (1780-1831), the French consul of Aleppo in 1814 (Raymond, 2010). The broken, bold line between the gates represents rests of the wall of the old city. (modified after Barbié du Bocage, 1825: 218-244).

wall, suburbs, small gates of suburbs, and significant buildings along with public establishments, gardens and cemeteries.

As seen, Aleppo was a famous city in the East and West, and had important economic, cultural, and historical value. Unfortunately, this situation changed completely in few seconds at the night of August 13, 1822.

Tectonic Setting and Seismicity

The 1822 earthquake struck a region located in northwestern Syria and Turkish neighboring areas. In this region, three active faulting systems meet (Figure 3). They are the left-lateral Dead Sea fault (DSF), the left-lateral East Anatolian fault (EAF) and Cypriot Arc (CA), in which the Latakia fault

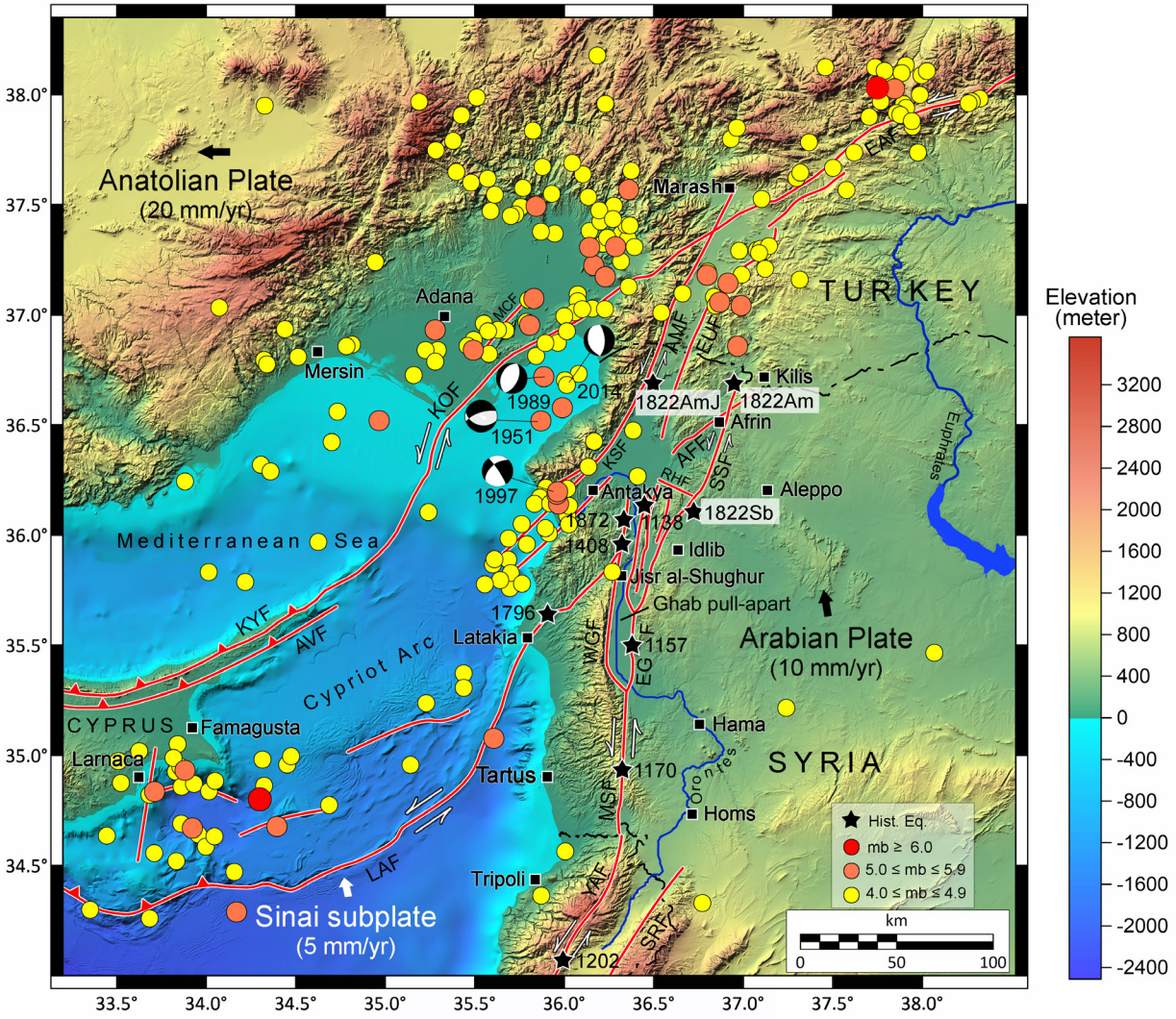

Figure 3. A digital elevation model of the northwestern of the Mediterranean showing the main faults (red lines), the distribution of instrumental seismicity (mb≥4.0) during the period 1900-2017 (different color circles), and the main historical earthquakes (black stars). The epicenters of the 1822 earthquake of previous studies are symbolized according to Table 1. Faults are from Över *et al.* (2002), Karakhanian *et al.* (2008), Tari *et al.* (2013). Instrumental earthquake data are compiled from ISC. Abbreviations of the faults: AFF: Afrin fault; AMF: Amanus fault; EAF: Eastern Anatolian fault; EGF: East Ghab fault; HPF: Hacipaşa fault; KOF: Karataş-Osmaniye fault; LAF: Latakia fault; KSF: Karasu fault; MCF: Misis-Ceyhan fault; RHF: ar-Rayhaniyah fault; SSF: Saint Simeon fault; WGF: West Ghab fault. Large black arrows present relative plate motions after (Jackson and McKenzie, 1988; McClusky *et al.*, 2000).

(LAF) is the southern segment of the CA. The DSF represents a plate boundary between the Arabian plate and Sinai subplate, EAF is the plate boundary between Arabian and Anatolian plates, and CA is a wide boundary between Sinai subplate and Anatolian plate. This means there is a triple junction in the region. In this regard, Over *et al.* (2004), using SPOT imagery and seismicity data, defined the point of triple junction to the NE of Antakia in the Amik basin (so-called Antakia or Amik triple junction, ATJ).

Numerous faults exist to the west of Aleppo within the ATJ. The 145-km-long Amanus (Karasu) fault (AMF) has a NNE-SSW orientation. AMF may be part of the EAF (Westaway, 1994). The

114-km-long Saint Simeon fault (SSF) stretches from the northeastern corner of Ghab pull-apart basin in NNE-SSW direction. Karakhanian *et al.* (2008) demonstrated that SSF is an active fault according to the observed left-lateral displacements and deformations of the landforms. North of Afrin, the 40-km-long Afrin fault (AFF) joins the SSF. No information is available for AFF. Between Jisr ash-Shughur and Antakia, the active NS Hacipaşa fault (HPF) exists, which belongs to the northern DSF (Akyuz *et al.*, 2006).

Instrumental seismicity from 1900 is low to moderate (Figure 3). Focal depths are in the range of 5-15 km. As shown in Figure 3, the earthquake activity for ≥ 4.0 (mb) is mainly distributed along EAF, the extension of AMF at sea, and along the Karataş-Osmaniye fault (KOF). Although the instrumental seismicity reveals only small to moderate earthquakes, the region has been the site of numerous large historical earthquakes that damaged Aleppo, Antakia, Latakia and other towns, like the 10 October 1138, 29 December 1408, 26 April 1796, 13 August 1822 and 3 April 1872 (Ambraseys, 1989; Ambraseys, 2004; Guidoboni *et al.*, 2004; Sbeinati *et al.* 2005). Consequently, this may indicate that the current seismic activity may be going through relative quiescence, compared with the historical earthquakes (Abdul-Wahed and Asfahani, 2018).

Data and Methodology

Historical Sources of Information

In this paper, thirteen new contemporary and near-contemporary sources of information cited partly or not cited in the works of Ambraseys (1989) and Sbeinati *et al.* (2005) are presented. These new sources, listed in Table 2, enabled us to describe in more details the seismic damage in Aleppo, Antakia and Latakia, and to identify new affected localities. These new sources include local accounts written by Aleppians; British and French consular correspondences from Aleppo and Latakia in Syria and Kiti in Cyprus; Letters written by visitors; accounts left by travelers; diaries and accounts written in European magazines and journals. Also, other historical sources that include very short accounts of aftershocks of the main 1822 earthquake were considered and used.

Historical Earthquake Methodology

For re-assessing the 1822 earthquake, the procedures recommended by the International Atomic Energy Agency (IAEA, 1987) were considered. These procedures concern the methodology of the historical earthquake search, how to study these data, and how to extract and assess the parameters of historical earthquakes.

These new sources (Table 2) were studied to re-assess the 1822 earthquake and its effects. Also, some secondary sources and studies dealing with this earthquake were considered. We estimated the macroseismic intensity using the European Macroseismic scale, EMS-98 (Grünthal, 1998). In addition, some focal parameters of the earthquake were estimated based on the empirical relationships of Ambraseys and Jackson (1998). The surface-wave magnitude (Ms) of the earthquake was estimated with the empirical relationship, developed by Ambraseys and Jackson (1998), for the Middle East:

$$Ms = -1.54 + 0.65\ (I_i) + 0.0029\ (R_i) + 2.14 \log (R_i) + 0.32\ p \qquad (1)$$

Table 2. A list of the new historical sources for the earthquake of 1822.

Source of information	Type of document/date (language)	Main localities mentioned	Reference(s)
Paul Aroutine, bishop	Manuscript (Arabic)	Aleppo	Aroutine (1933)
- Nasrallah Ghazaleh, clergyman - Jromanus Hawa, bishop	- Letter (Arabic) - Church archive/16 April 1823 (Arabic)	Aleppo	Taoutel (1958)
Mohammad Agha Mekansi, Aleppine centenarian	Diaries (Arabic)	Aleppo	Al-Ghazzi (1926)
Benjamin Barker, brother of the British Consul in Aleppo	Letter/23 Aug. 1822 (English)	Aleppo	The Religious Tract Society (1822); Conder (1824)
John Barker, British Consul at Aleppo	Account/13 Sept. 1822 (English)	Aleppo, sea waves between Cypriot and Syrian coasts	The Edinburgh Magazine (1823)
Joseph Wolf, Missionary and oriental scholar	Traveler account/diary (English)	Jawziyah, Latakia	The Missionary Journal (1824)
Anonymous English gentleman	Diaries (English)	Antakya, sea waves in Suwaydiyeh	Neale (1854)
Anonymous	Account (English)	Aleppo, Latakia, Jableh	Miller (1826)
Austrian Observer	Letter/ 3 Sept. 1822 (English)	Aleppo, Antioch, Latakia, sea near Cyprus	The Asiatic Journal (1822)
Monsieur Derché, second dragoman of the French Consulate in Aleppo	Document/14 Aug. 1822 (French)	Aleppo	Derché (1824)
Charles-Édouard Guys Vice-Consul of France in Latakia	document of archive/15 Oct. 1822 (French)	Latakia, Jableh, al-Markab	Bulletin de la Société de Géographie (1822)
Observatoire Autrichien	Account/1822 (French)	Aftershocks at Aleppo	Gazette Géographique (1822)
Anonymous	Annals (French)	Aleppo	Gay-Lussac and Arago (1822)

where $R_i=(r_i^2+9.72^2)^{0.5}$ and r (km) is the mean isoseismal radius of intensity I, and p is zero for mean values and one for 84 percentile values. Ms was converted to moment magnitude (M_W) using the following empirical relationship developed for Syria (Alissa *et al.*, 2021):

$$M_W = 0.75\ Ms + 1.39 \pm 0.5 \quad (2)$$

Simulation Method

The stochastic finite-fault method is widely used in ground-motion simulations of past or scenario earthquakes. Here, we use the extended stochastic finite-fault simulation method (EXSIM) proposed by Motazedian and Atkinson (2005).

The EXSIM was developed from both the stochastic point source simulation (SMSIM) proposed by Boore (1983, 2003), and the finite fault simulation (FINSIM) proposed by Beresnev and Atkinson

(1997, 1998). Strong ground motion simulation involves a physical approach, using the earthquake source, the path, and the site effects. The stochastic point source model assumes the source process is concentrated at a single point and the acceleration time series generated at a site carries both deterministic and stochastic aspects of ground motion. The deterministic part, which is a function of both magnitude and distance, is specified by Fourier amplitude spectrum, and the stochastic aspects are obtained by treating the motion as white noise. Beresnev and Atkison (1997) extended the stochastic procedure to large faults by subdividing the large fault into sub-faults, each of which is then treated as a point source. The ground motions at a site is obtained by summing the contributions of all sub-faults. Motazedian and Atkinson (2005) introduced the concept of dynamic corner frequency to reduce the dependence on sub source size.

In this study, the latest version of extended stochastic finite-fault simulation code EXSIM12 (Atkinson and Assatourians, 2015) is employed to simulate the ground motion of the 1822 earthquake at the citadel of Aleppo. This prominent archaeological structure is chosen since it was built on a rocky hill and was damaged by the 1822 earthquake. The ground motion records have been simulated with ten trials to eliminate the bias resulting from stochastic variability.

Results

The Earthquake of 13 August 1822

It should be mentioned that the previous devastating earthquake prior to the 1822 earthquake that destroyed Aleppo was on 11 October 1138. This suggests 684 years of no other major earthquakes until the 1822 earthquake occurred.

The 1822 earthquake was preceded by several foreshocks in a short period (some days). The main event was followed by aftershocks lasting for months. A series of small foreshocks lasted about 7 days. They were felt in Pachalic of Aleppo. The last foreshock happened on 13 August 1822 (at 8 pm local time), half an hour before the main destructive event. This last foreshock event caused great fear in Aleppo. However, no one was able to leave the city because its gates were closed at that moment. This main earthquake took place during a hot summer evening when the people were sitting on the roofs or in courtyards of their houses. This earthquake affected mainly most of Pachalic of Aleppo, the northern part of Tripoli Pachalic, and some parts of Marash Pachalic (see Figure 1 for location). It should be mentioned that four aftershocks occurred one hour following the main event.

In Aleppo, the main earthquake caused large damage and great loss of life. What follows is a summary of the main testimonies of the personalities for the horrible scenes of the earthquake in the city: i) Mohammad Agha Makansi (ca. 1787-1891), an Aleppine centenarian (Al-Ghazzi, 1926: 330-334); ii) Paul Aroutine (1788-1850), bishop of Aleppo (Aroutine, 1933: 77-78); iii) Benjamin Barker, brother of the British consul in Aleppo, John Barker (1771-1831) (Religious Tract Society, 1822), and iv) Monsieur Derché, the second dragoman of the French consulate in Aleppo (Derché, 1824 : 162-168). These four eyewitnesses, who miraculously survived the earthquake, saw tragic scenes in Aleppo such as women without headgear screaming and beating on their chest, laments of the people, death corpses and wounded in the streets, considerable number of inhabitants buried under debris, fallen walls of houses and people rushing toward the neighborhood orchards around the city. Many people tried to recover their death, including their children who were under debris. The fallen houses and buildings produced a cloud of dust that covered the city. After a short time from the main shock, another strong shock completed the destruction in the city.

At dawn of the next day, the size of the catastrophe started to be seen. Dead bodies were seen floating on the Quaik river and many structures and tall buildings partially or completely collapsed. Damages concentrated in the quarters of Bahsita (NW of the old city), Al-Aqaba (west of Aleppo citadel), Al-Farafira (NW of the citadel), Al-Attareen (herbals) souk, towers of the citadel, in addition to most of the houses and buildings located around the citadel (see Figure 2 for locations). The citadel itself along with its great mosque was severely damaged and most of the inhabitants left the citadel and settled in the city below. Also, the ring wall of the citadel, which is composed of towers linked by curtain walls, was damaged. Numerous mosques were severely damaged; the minaret of the Umayyad Mosque (b. *circa* 713) was split and also Al-Mehmendar mosque (b. 14th century) located north of the Citadel. Due to the strength of the shaking, the crescent of minaret of Al-Othmaniyeh Mosque (b. in 1730), located near Bab Al-Nasr fell to the ground through the southern dome, forming a hole. Also, the dome of the Behramiyeh Mosque (b. 1580) collapsed. The minaret of the Mosque of Al-Kizawani, one of the religious and historical features of Aleppo located in Al-Aqaba quarter, was cut from its middle. Madrassa (school) of Al-Khusruwiyah (b. 1537), located directly west of the citadel, was also damaged. The old Maronite church of Saint Elias (b. *ca* 15th century) located in the quarter of Al-Jdiadeh was damaged, requiring the Bishop Jromanus Hawa (1752-1827) to send a letter to the British consul on April 16, 1823, complaining on the bad conditions of the parish and asking for help in restoration of the damaged church (Taoutel, 1958: 133-134). Also, Nasrallah Ghazaleh (the clergyman in Aleppo at the time of earthquake), reports that the shaking of the main event caused great fright, to the extent that large number of infants was died. The cathedral of the Dormition was damaged also by the earthquake. The main synagogue located in Al-Aqaba quarter was destroyed. A part of the wall of the old city collapsed on people. The British consulate in Aleppo was completely ruined and the private houses of the European residents were destroyed. Moreover, Khan Al-Hibal (robes) (b. 1594), which was a residence of the French consulate and located, a short distance to the west of Umayyad Mosque, suffered severely without any loss of life. The Austrian general consul in Aleppo, M. Esdra de Picciotti, perished under the debris with 10-12 persons of his family, together with 16 horses, due to the first strong aftershock, these who with him.

The public safety in Aleppo was disturbed due to the earthquake and looting and theft have increased. In this regard, Knost (2010) documented that the Aleppo court was damaged, and its activity interrupted as seen in the court records of the Law Court Registers. Few days later, numerous cases of ophthalmia and dysentery appeared in the city (The Asiatic Journal, 1822: 519). The great number of unburied bodies in this extremely hot period of year produced pestilential effluvia and forced survivors to seek refuge in distant districts. Table 3 presents these aftershocks, and Figure 4 is a time series of the 1822 earthquakes. Therefore, Aleppines remained encamped around the city few months later (The Asiatic Journal (1822: 519) However, these aftershocks seem to continue till 10 October 1824 (The Missionary Herald, 1825: 373). The Asiatic Journal (1822: 519) also mentioned that an immense quantity of valuable goods of all kinds from Persia and India has been destroyed. It is said in Aleppo that a meteor fell near the village of Atarib at the night of August 13, 1822.

Numerous historical sources mentioned that some ruins in Aleppo due to 1822 earthquake were observable for a long time (Figures 5, 6 and 7). In contrast to the evident destruction in the previous figures, some minarets and towers remained standing. It could be argued that they would be the first to fall during strong shaking. For example, Figure 6 stresses the debris of the barracks of Ibrahim Pacha. However, the minaret of the Big Mosque is unscathed. Figure 7 does show the remains of

Table 3. A list of foreshocks and aftershocks of the 1822 earthquake.

Date (LT)	Description	City/town	Reference(s)	Intensity (EMS-98)
5 Aug. 1822	slight shock	felt at Aleppo & Antakia	Ambraseys (1989)	IV
5-12 Aug.	slight shocks	felt at Aleppo & Antakia	Ambraseys (1989)	III-IV
10 Aug.	slight shock	felt at Aleppo	R. Mallet & J.W. Mallet (1858)	IV
12 Aug.	slight shock	felt at Aleppo, Antakia & Latakia	Miller (1826)	IV
13 Aug. (20:10)	strong shock	felt between Latakia, Aleppo & Antakia	Ambraseys (1989)	V
13 Aug. (20:40)	main shock	Northwestern Syria & the nearby areas in southern Turkey	All sources of information mentioned in Table 2	VIII-IX
13 Aug. (night)	successive damaging shocks	felt at Aleppo, Antakia & Aintab	Ambraseys (1989)	VI
14 Aug. (morning)	great shock	felt at Aleppo	R. Mallet & J.W. Mallet (1858); Aroutine (1933)	VI-VII
15 Aug.	destructive shock	felt at Urfa & Aleppo with some damage	Perrin (1822)	VI
16 Aug.	strong shock	felt at Aleppo	Gay-Lussac & Arago (1822); Perrin (1822)	V
20 Aug.	terrible shock	felt at Latakia	Bayford (1824)	VI
23 Aug.	destructive shock	-	Ambraseys (1989)	VI
4 Sept. (sunset)	destructive shock	felt at Aleppo	Aroutine (1933)	IV-V
5 Sept. (night)	numerous shocks, one of them destructive	damages of some tall buildings at Aleppo	Gay-Lussac & Arago (1822); Gazette Géographique (1822); R. Mallet & J.W. Mallet (1858)	VI
13 Aug.- 20 Sept.	38 felt shocks	felt at Aleppo	Purdy (1832)	III-VI
29 Sept.	several shocks	felt at Aleppo	R. Mallet & J.W. Mallet (1858)	IV
30 Sept.	several shocks, one of them violent	felt at Aleppo	Gazette Géographique (1822); R. Mallet & J.W. Mallet (1858)	IV
31 Sept. (afternoon)	violent shock	felt at Aleppo	Aroutine (1933)	IV
19 Oct.	violent shock	felt Aleppo	John Barker (Condor, 1824); Purdy (1832)	VI
First half of Nov.	strong shocks	felt at Aleppo	Gay-Lussac & Arago (1822); Gazette Géographique (1822); R. Mallet & J.W. Mallet (1858)	IV-V
12 Nov. (night)	very violent shock	felt at Aleppo	R. Mallet & J.W. Mallet (1858)	VI

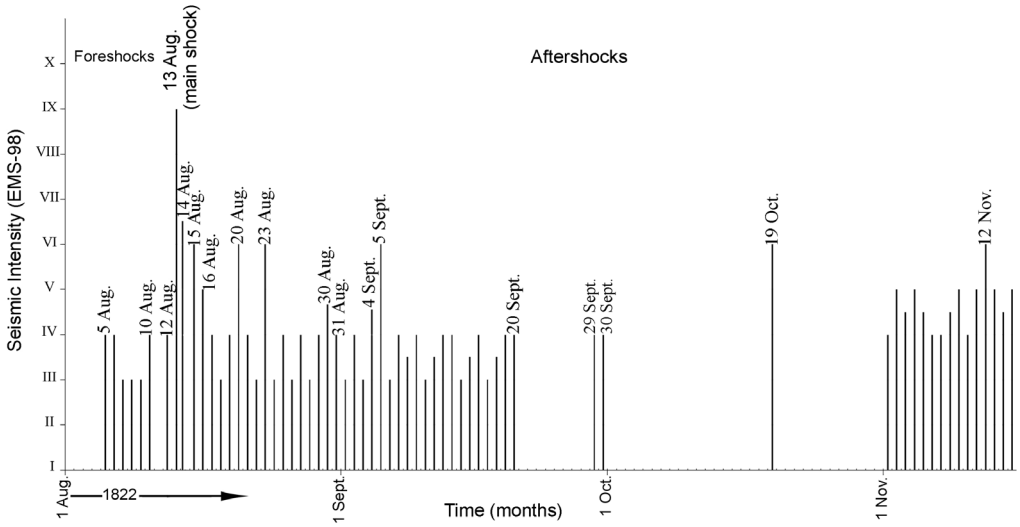

Figure 4. Time series of the most 1822 earthquakes from 5 August 1822 till 15 November 1822 that were felt in and around Aleppo, as documented by the numerous sources of information (last column in Table 3). Each black vertical line indicates a single event.

Figure 5. The earliest known photograph of Aleppo taken in 1844 by the French photographer Joseph-Philibert Girault de Prangey (1804-1892) showing the miserable condition of the city due to the 1822 earthquake (black arrows). Source: Metropolitan Museum of Art at: https://www.metmuseum.org/art/collection/search/726483

Figure 6. A photo inside the citadel of Aleppo taken in 1895 showing the debris resulted by the 1822 earthquake and the damages of the Great Mosque (black arrows). The debris was still in situ till the beginning of the 20th century. Source: Historical Digital Documentation House in Aleppo: https://www.dig-doc.org/images/photo_gallery/pic_322020124558.jpg

Figure 7. A photo of Aleppo dated back to 1890 showing Bab Qinnsarin, one of two southern gates of the city. Note the remains of its tower destroyed by the 1822 earthquake. Source: Historical Digital Documentation House in Aleppo at: https://www.dig-doc.org/images/photo_gallery/pic_36202052727.jpg

the tower in the southern gate of the city. Once again, this picture, taken in 1890, 68 years after the Aleppo earthquake, shows a very slim minaret of the Al-Adiliyah mosque. There is no evidence that these apparently sensible constructions withstood the 1822 earthquake or whether they were later reconstructed. But it is likely that they were rebuilt since they were religious places that benefitted from donations of benefactors. The earthquake formed a real phobia for the Aleppines to the extent that from time to time rumors appear of the imminent occurrence of a major earthquake, causing people to panic, leaving their houses and fleeing to the nearby orchards (Bakhkhash, 1985: 16).

Concerning the loss of life in Aleppo, the main earthquake of 13 August happened at night when most people were indoors, and this contributed to large number of deaths. Estimates of the number of deaths in Aleppo city alone vary between 15000 persons (Al-Ghazzi, 1926: 332), to 25,000-30,000 (e.g. Asiatic Journal, 1822: 519). We believe that these numbers may be exaggeration, but it is certain that the number of people killed was at least 10,000. This figure represents a considerable percentage of Aleppo population at that time. On the other hand, there were an equal number of maimed or wounded. In view of the heavy damage in Aleppo due to the 1822 earthquake, the seismic intensity is estimated between VIII and IX on the EMS-98 (See Figure 8).

Villages located about 30 km west of Aleppo were damaged, but without any details, such as those located at the plain of Al-Halaqa (Turmanin, Hazra, Dana, Teladeh and Deir Hassan) (Al-Tabbakh, 1925: 407). These last villages are directly located on the St. Simeon fault.

The small town of Idlib, at a distance of 53 km southwest of Aleppo, was entirely ruined. A script documents that its Grand Mosque dated on Mamluk era was repaired after the 1822 earthquake (Fayez Kosara, Historian of Idlib, personnel communication, 2018), a possible indication that this mosque was damaged by the earthquake (See Figure 8). The village of Maaret Misrin located 50 km southwest of Aleppo was destroyed. In this regard, Knost (2010) found in the Law Court Registers in Aleppo that a hammam (bath) and the walls of a farm in this village were damaged.

Antioch, the famous town through the history with about 9,000 to 10,000 inhabitants before the earthquake (Bell, 1832: 194), and located 90 km distance west of Aleppo, was strongly damaged by the earthquake causing a considerable loss of life. It is worth mentioning that Antakia was largely damaged by previous destructive earthquakes, such as the 29 April 1407 (Ambraseys and Melville, 1995). For this town, there is an anonymous English eyewitness who lived in Antakia at the time of 1822 earthquake, and his memories were presented to the English Sir Frederick Arthur Neale (1821-1863) when visited the town 25 years later of the earthquake (Neale, 1854: xxiii-xxxiv). He recalls how Antioch was turned into a miserable state after the earthquake, and that mosques and buildings were destroyed to the extent that the streets were filled with debris. Half of the houses was leveled, and the other half were damaged. In this regard, the Antioch Court records are rich in dozens of documents indicating the demolition of houses, stores and buildings as a result of the earthquake of 1822 (Capar, 2017). The survivors were busy assisting the villagers and rescuing the wounded. The Grand Khan of the town was destroyed, with its camels and beasts under its debris. Along the coast of Suwaydiyah, the sea was largely disturbed and no boat could withstand the sea waves. Some unofficial estimates have mentioned that four to five thousand people perished by the earthquake, representing half of the population of Antioch (Neale, 1854: xxiii-xxxiv; The Edinburgh Magazine, 1823). Pliny Fisk (1792-1825), an American missionary, visited Antakia in late 1824, and saw ruins of walls, houses and mosques due to the 1822 earthquake (Bond, 1828: 390). John Barker, the Brit-

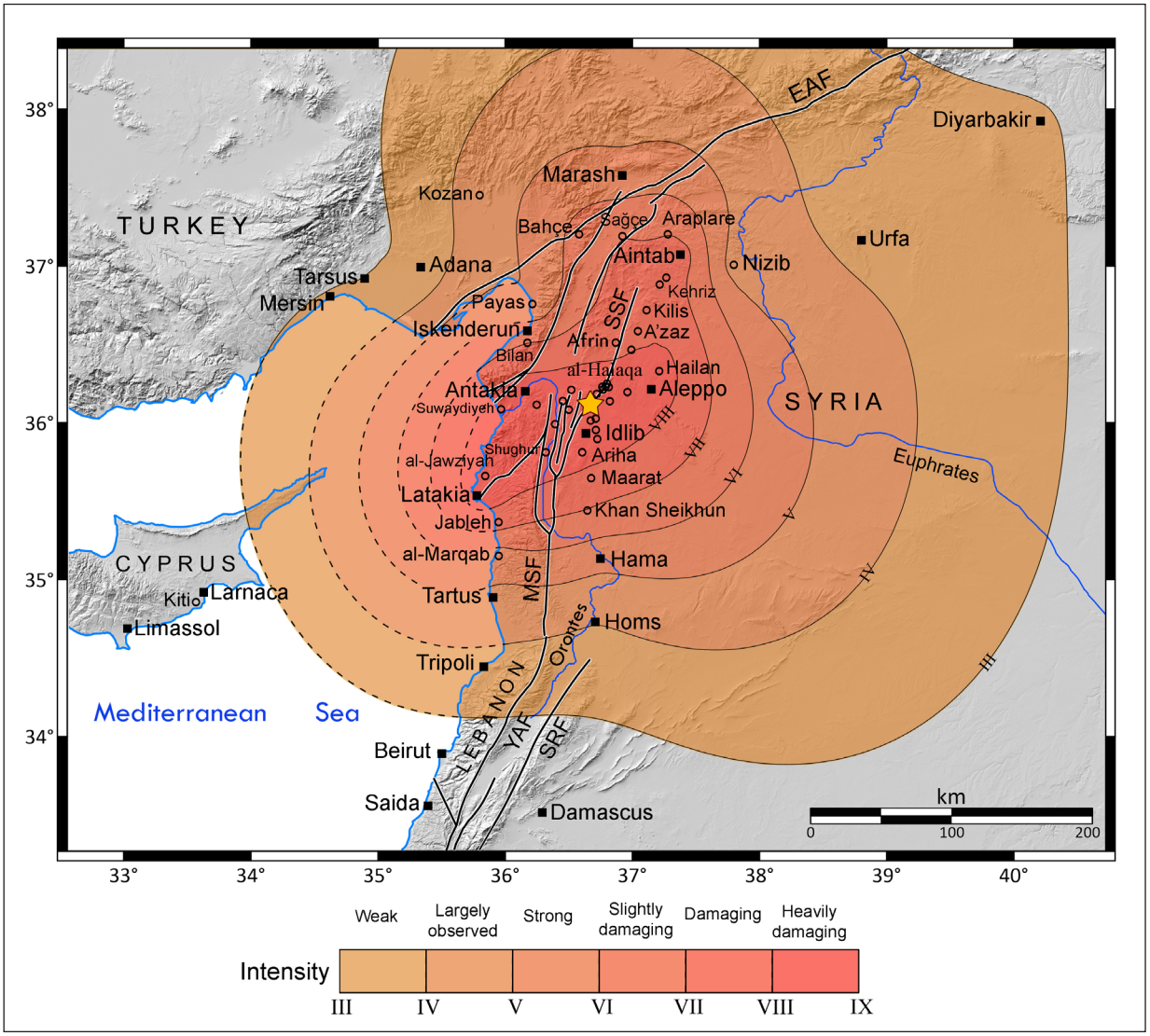

Figure 8. A map showing locations of cities (black squares), towns and villages (empty circles) affected by the 13 August 1822 earthquake. It also shows an averaged isoseismal map for the earthquake. The numbers ranging from III to VIII are intensity degrees on the EMS-98, assessed in this study. The earthquake epicenter is shown with a yellow star. The group of overlapping circles located west of Aleppo are villages of Sahle (plain) al-Halaqa. Abbreviations of the active faults: EAF: East Anatolian fault; MSF: Missyaf fault; SRF: Serghaya fault; SSF: Saint Simeon fault; YAF: Yammouneh fault.

ish consul in Aleppo, was at his country-house near Suwaydiyeh, at the time of the earthquake. He and his wife survived the earthquake and mentions that ground cracks were seen everywhere around the town, and the buildings located on the top of mountains were damaged or destroyed. Based on these effects of the 1822 earthquake in Antakia, the seismic intensity is estimated between VIII and IX on the EMS-98 (See Figure 8).

The town of Salqin, located ~30 km east of Antakia and 80 km from Aleppo was destroyed. In the small town of Armanaz, 60 km southwest of Aleppo, damages were serious. It is to mention that there is now a clear inscription at the southern entrance of the Grand Mosque in Armanaz documenting the date of its reconstruction after the 1822 earthquake (Majd Sari, member of the Syrian

Astronomical Association, personnel communication, 25 April 2019). In the village of Darkush, located 32 km SE of Antakia, the castle, collapsed and masses of rocks fell on the village destroying most of its houses.

In 1818, Latakia was a flourishing town along the Syrian coast located 145 km southwest of Aleppo, with a population of about 6,000 and 300 houses together with several large magazines (Purdy, 1832: 255). Latakia also suffered strongly from the 1822 earthquake. Several documented earthquakes caused also destruction during its long history; the 26 April 1796 was the last previous one with 1,500 death (e.g. Ambraseys, 1989). Two contemporary sources of information were eyewitnesses on the destruction of the town due to 1822 earthquake: i) Charles-Édouard Guys (1783-1871), vice-consul of France at Latakia in 1822 (Guys, 1822: 301-305), and ii) Joseph Wolff (1795-1862), the German missionary and orientalist who was in a mission in the region (Bayford, 1824: 325-328). The main event of 13 August 1822 caused heavy damages in the town (Miller, 1826: 23). Half of the town was destroyed, and many houses were damaged. Joseph Wolff mentions that 150 houses were totally destroyed, and several hundred people lost their life. Most people ran from their houses and encamped outside the town for a long time. Some families deserted the town and settled in other nearby regions. It is said that the *Maktab* (school) collapsed on the children killing all of them. The quarter that includes houses of the European consuls has suffered the most. Charles-Édouard Guys says that the French consulate registered one-third of the town collapsed, nearly 200 deaths, and the ruin of the fortress located at the Marina was damaged. He adds that the Big Mosque, the Custom and the Grand Khan (*Khan al-Dukhan* or *Tobacco*), located in the seaport (Scala or Marina), were among the damaged buildings. The English traveler George Robinson, who visited Latakia in 17 April 1831, observed numerous large fissures in the walls of houses, and immense stones displaced in many parts of the town due the 1822 earthquake (Robinson, 1837: 363). Aftershocks were felt in Latakia four to five times a day for 40 days as mentioned by Wolff (Bayford, 1824: 325-328).

Several villages around Latakia were totally destroyed. One of them was al-Jawziyah located 15 km to the northeast of latakia (See Figure 8). It is now called Khirbet, meaning ruin of al-Jawziyah. Joseph Wolff in his way from Antakia to Latakia was again an eyewitness in that night of the total destruction of the houses in the village including the killed women, children and cattle. Also, he felt at the night of 13 August with numerous shocks (Bayford, 1824: 325).

In the small coastal town of Jableh, 20 km southeast of latakia, the news arrived that this town became ruins, but some people could escape from the town and the Grand Mosque, which is called Sultan Ibrahim, was damaged (Guys, 1822: 303). Also, Miller (1826: 24) says that three quarters of the town are destroyed, its harbor chocked up by the ruins of the houses that have been fallen into it and 300 persons have lost their lives.

The Crusader castle of al-Marqab, built in late 12th century and located south of Jableh on the top of a mountain, collapsed by the earthquake (Guys, 1822: 303). Further south, the earthquake was felt in Tartus, Tripoli and Saida (Guys, 1822: 303).

Between Aleppo and Latakia, several towns and villages have been destroyed. One of them was Jisr Al-Shughur, the main town that located on the Orontes river. Here, the Great Mosque (*Jamea al-Coprly*) was slightly damaged, but details are lacking. In this regard, both French travelers, Joseph Michaud (1767-1839) and Jean Poujoulat (1808-1880) on their way from Latakia to Aleppo found Jisr Al-Shughur was heavily damaged due to the earthquake of 1822 as mentioned in the letter no. 173 dated on June 1831 (Michaud and Poujoulat, 1841: 27). News has come to Latakia that

Suwaydiyeh and Iskenderun were totally destroyed. For example, Iskenderun transferred into ruins (Guys, 1822: 303).

The small town of Afrin, 40 km northwest of Aleppo, was particularly affected and many buildings were destroyed (Knost, 2010). Aintab, located in southern Turkey, felt this earthquake (Guys, 1822: 303).

The main earthquake was felt in Larnaca (Cyprus), as well as some of its strong aftershocks (Regnault, 1822: 215), without causing damage. Between the Syrian and eastern Cypriot coasts, sources mention that the earthquake was felt so violently at sea at a distance of two leagues (~11 km) of Cyprus to the extent that it was thought the ships in Cyprus had grounded, as described by John Barker in his famous official account (e.g. Conder, 1824: 298). Other sources said that two rocky masses arose from the sea near Cyprus at the time of earthquake (e.g. Asiatic Journal, 1822: 519). This last observation was written on 3 September 1822 in a report of a caption of French ship departed from Cyprus to Latakia. A summary of previous macroseismic data for the 1822 earthquake is listed in Table 4.

The earthquake of 13 August 1822 did not only affect the aforementioned cities, towns and villages, it also damaged numerous towns and cities in northwestern Syria and its neighboring areas in central-southern Turkey. This damage is well-documented by Ambraseys (1989) and Sbeinati *et al.* (2005). Figure 8 shows almost all cities, towns and villages affected by the event based on the last two works and our study.

Earthquake Parameters

One of the targets of this paper is to convert the historical descriptions of the 1822 earthquake into parameters that can be used in the modeling the earthquake effects. In this paper, it is notable that the details of damage descriptions of the 1822 earthquake are not confined to Aleppo; damage descriptions in other cities such as Antakia, Latakia and their surroundings have been detailed in the current paper. Other towns and villages in the region had very short description of the damage. The heavy damages of the 1822 earthquake have been observed at the cities: Aleppo, Antakia and Latakia. Therefore, the epicenter is probably located between these three cities. Based on damage descriptions, the greatest damage occurred in Aleppo city. This implies that the earthquake epicenter is probably close to this city. The only nearest active fault to Aleppo is the Saint Simeon fault (SSF) (Figure 3). This fault is associated with numerous scarps and left lateral offsets (Karakhanian *et al.*, 2008). We suggest that the SSF could be responsible for the 1822 earthquake. This hypothesis requires paleoseismic investigation along the SSF to confirm this likely finding.

Referring to the tectonic map of Syria (Leonov, 1989), SSF is divided into three segments: the southern, central and northern ones with length of 42, 26 and 46 km, respectively. The central segment is likely to be the displaced one during the 1822 earthquake. In this case, the epicenter could be approximately estimated in the center of this segment at 36.11° N and 36.68° E. According to field investigations and some previous studies (Karakhanian *et al.*, 2008), the faulting type is strike-slip.

In view of the high level of damage and the great loss of life in Aleppo due to the 1822 earthquake, the seismic intensity could attain VIII-IX on the EMS-98. The size of the 1822 earthquake is large in term of magnitude. In this study, the Ms was estimated to be 7.7 ± 0.32 using the relationship (1) depending on macroseismic scaling laws of Ambraseys and Jackson (1998). The moment magnitude (Mw) was estimated to be 7.3 using the relationship (2).

Table 4. A summarized list of the macroseismic observation for the 1822 earthquake at the most affected localities (cities, towns and villages), as described in their references. The intensity values were assessed after the European Macroseismic Scale (1998). For location of these localities, see Figures 1 and 8.

Locality	Macroseismic observation	Reference(s)	Intensity
Aleppo	Very large destruction of houses, buildings and structures such as mosques (e.g. Umayyad, Al-Mehmendar, Al-Othmaniyeh and Behramiyeh), the citadel, khans (e.g. al-Hibal), the Maronite church of Saint Elias, the main synagogue and the British consulate. Damage concentrated in the quarters of Bahsita, Al-Aqaba, Al-Farafira and Al-Attareen Bazar. Great loss of life including the infants (15000-25000 deaths) and same figure for wounded.	- The Religious Tract Society (1822) - Derché (1824) - Al-Tabbakh (1925) - Al-Ghazzi (1926) - Aroutine (1933) - Taoutel (1958)	VIII-IX
Antakya	Large destruction including mosques, buildings and the khans (e.g. Grand Khan). Considerable loss of life (4000-5000 deaths).	- Neale (1854) - Tabbakh (1925)	VIII-IX
Latakia	Destruction of half of the town including the quarter of the European consuls, Khan of al-Dukhan, the Great Mosque and the Custom. ~ 200 deaths.	- Guys (1822) - Bayford (1824) - Miller (1826)	VIII-IX
Suwaydiyah	Occurrence of ground cracks around the village. Destruction of many buildings located on the top of mountains. Large disturbance of the sea and no boat could withstand the sea waves.	- Neale (1854) - John Barker	+ VIII
Darkush	Large destruction with large number of deaths. Masses of rocks fell on the village destroying most of the houses.	- Tabbakh (1925)	+ VIII
Jisr Al-Shughur	Total destruction. A minor damage for the Great Mosque, Jamea al-Coprly.	- Michaud and Poujoulat (1841) - Tabbakh (1925)	+ VIII
Maaret Misrin	Large destruction with considerable number of deaths.	- Tabbakh (1925) - Al-Ghazzi (1926)	+ VIII
Jawziyah	Total destruction with large number of deaths for women and children.	- Bayford (1824)	+ VIII
Salqin	Heavy damage.	- Tabbakh (1925)	+ VIII
Armanaz	Heavy damage.	- Tabbakh (1925)	+ VIII
Idlib	Large destruction.	- Tabbakh (1925) - Fayez Kosara*	+ VIII
Turmanin	Great damage.	- Al-Tabbakh (1925)	+ VIII
Hazra	Great damage.	- Al-Tabbakh (1925)	+ VIII
Dana	Great damage.	- Al-Tabbakh (1925)	+ VIII
Teladeh	Great damage.	- Al-Tabbakh (1925)	+ VIII
Deir Hassan	Great damage.	- Al-Tabbakh (1925)	+ VIII
Jableh	Destruction of three quarters including the mosque of Sultan Ibrahim. Killing ~ 300 people.	- Guys (1822) - Miller (1826)	VII-VIII
Al-Markab	Collapse of the castle.	- Guys (1822)	~ VI

* Personnel communication with Fayez Kosara (2018)

Simulation Parameters

The main set of inputs for simulation an earthquake are the source, the path, and the site effects parameters. The source parameters include the moment magnitude, hypocentral location (latitude and longitude), and fault geometry. As mentioned above, the 1822 earthquake is probably located along the St. Simeon fault at a focal depth about 15 km. Also, the faulting type is strike-slip and the strike, dip, and rake have been estimated to be N 42°E, 90°, -10°, respectively. The tectonic map of Syria (Leonov, 1989) demonstrates a length of central fault segment to be 26 km. The wide and the top of fault have been estimated to be 15 and 0 km, respectively. The fault of size 26 × 15 km is discretized into 2 × 2 km size sub-faults (91 in total). The stress drop has been estimated to be 90 bars using empirical relations of Kanamori and Anderson (1975), and macroseismic scaling laws of Ambraseys and Jackson (1998).

Path effects are corrected by geometric spreading, the anelastic attenuation, the near-surface attenuation, as well as site amplification factors. Due to lack of detailed studies on attenuation model and the absence of strong motion recordings in Syria, other parameters were assigned based on previous published works: i) The pulsing area percentage is assigned as 50% (Atkinson and Boore, 2006); ii) The sub source window is selected as Saragoni-Hart taper window for time-modulating Gaussian white noise (Saragoni and Hart 1974); iii) The epsilon (ε) and eta (η) values of the tapered window are fixed as 0.35 and 0.15, respectively; and iv) The shear wave velocity (β) and density have been estimated according to the regional velocity model to be 3.7 km/s and 2.8 g/cm^3, respectively (El-Isa *et al.*, 1987; Mechie *et al.*, 2005). For the distance-dependent attenuation, we applied a geometric spreading operator of 1/R, in which R is the distance from the seismic source (Zengin and Çaktı, 2014). The anelastic attenuation, described through a frequency-dependent quality factor $Q(f)= Q_0 f^{\alpha}$, is taken from the works of Mitchell *et al.*, 1997; Steck *et al.*, 2009; Bao *et al.*, 2011; Mohamad *et al.*, 2012. The Q_0 (Q at 1 Hz), for which the values are ranging between about 200 and 400, and frequency-dependence (α), for which the values are in the range 0.5-0.7. The crustal amplification factors were worked out with the Syrian velocity model (El-Isa *et al.*, 1987; Mechie *et al.*, 2005; Ibrahim *et al.*, 2012) using the quarter-wavelength approximation method (Boore and Joyner, 1997). The velocity with which the rupture propagated during this event, rupture velocity (V_{rup}) is obtained from literature as 0.8*Vs; Kappa value, which characterizes near-surface attenuation, is taken to be 0.035 as suggested by Boore and Joyner (1997) for generic rock sites. The total path duration is calculated as a function of distance (R) based on Beresnev and Atkison (1999). The response spectra are computed at 1, 3, 5, 10 and 20% damping ratios at the frequency range of engineering interest (Atkinson *et al.* 2009). Time step is fixed as 0.01 sec to be compared with probable observational data. The simulation was run using the above input parameters, as summarized in Table 5.

Simulation Results

Simulation for 1822 Aleppo earthquake was run with EXSIM method. Acceleration time series and damped Pseudo Spectral Acceleration (PSA) were generated for the site of Aleppo citadel without considering local site-effects, where this site could be considered as rocky site. The site of citadel, located at a distance of 44 km from the epicenter, has been affected by 1822 earthquake, where considerable damages occurred. Figure 9 shows the simulated acceleration time history computed at the bedrock level. The simulated peak ground acceleration (PGA) was determined after ten iterations. This PGA obtained was 0.4 g. For synthetic acceleration time series, we select the one with this

Table 5. A list of the basic input parameters used in the stochastic finite-fault model.

Parameter, symbol	Value/unit	Reference
Moment magnitude, M_W	7.3	present work
Latitude & longitude	36.7° E, 36.1° N	present work
Hypocenter depth	15 km	present work
Faulting type	strike-slip	present work
Fault strike, dip & rake	N 42°E, 90°, -10°	present work
Fault length, width & depth	26, 15 & 0 km	present work
Fault size	26 km × 15 km	present work
Subsource length & width	2 km × 2 km	present work
Number of sub-sources	13 × 7 (91 in total)	present work
Slip distribution	Random	present work
Stress drop, Δσ	90 bars	present work
Shear wave velocity, β	3.7 km/s	Mechie *et al.* (2005)
Crustal density, ρs	2.8 gm/cm^3	Mechie *et al.* (2005)
Rupture velocity, V_{rup}	0.8 × Vs	Atkinson *et al.* (2009)
Fault pulsing area	50%	Atkinson and Boore (2006)
Subsource window	Saragoni-Hart (W_ε=0.35, W_η=0.15)	Saragoni and Hart (1974)
Damping ratios	1, 3, 5, 10 and 20%	Atkinson *et al.* (2009)
Path duration	0.16 × R (10<R<70 km)	Beresnev and Atkison (1999)
Geometrical spreading, G(R)	1 / R (R<100 km)	Zengin and Cakti (2014)
Quality factor	Qmin=60, Q_0=300, α=0.6	Bao *et al.*(2011)
Kappa value, κ	0.035	Boore and Joyner (1997)

value of ten trials. The response spectra were computed at 1, 3, 5, 10 and 20% damping ratios for periods ranging from 0.02 to 100 seconds (0.01-50 Hz) (Figure 10). In particular, the 5% damped PSA represents the maximum acceleration caused by a linear oscillator with 5% damping and a specified natural period. The stress drop value of 90 bar was estimated using the empirical relations. However, numerous trials to choose the best parameters for simulating the earthquake were run. For example, a small stress drop (60 bar) and a larger stress drop (120 bar), meaning that ± 30% as a large uncertainty, have been tested. The results of simulations were as follows: 0.29 and 0.45 g respectively. Accordingly, the uncertainty of stress drop can produce an uncertainty of 0.1 g in PGA.

The simulated strong ground motion time histories and PSAs could be considered as the best kind of information required for engineering structural design in the absence of real accelerograms in Syria. However, these results need to be validated by comparison with the strong motion recordings when they become available. The direct comparison between simulation results and observed ground motions during real earthquakes allowed us to evaluate the efficiency and limitations of the simulation method. Complementary work should include the use of strong motion records when available and of physical models of propagation.

Discussions

This work provides additional details on the damages and loss of life in the cities of Aleppo, Antakia and Latakia and their surroundings due to the 1822 earthquake. However, the destruction and the

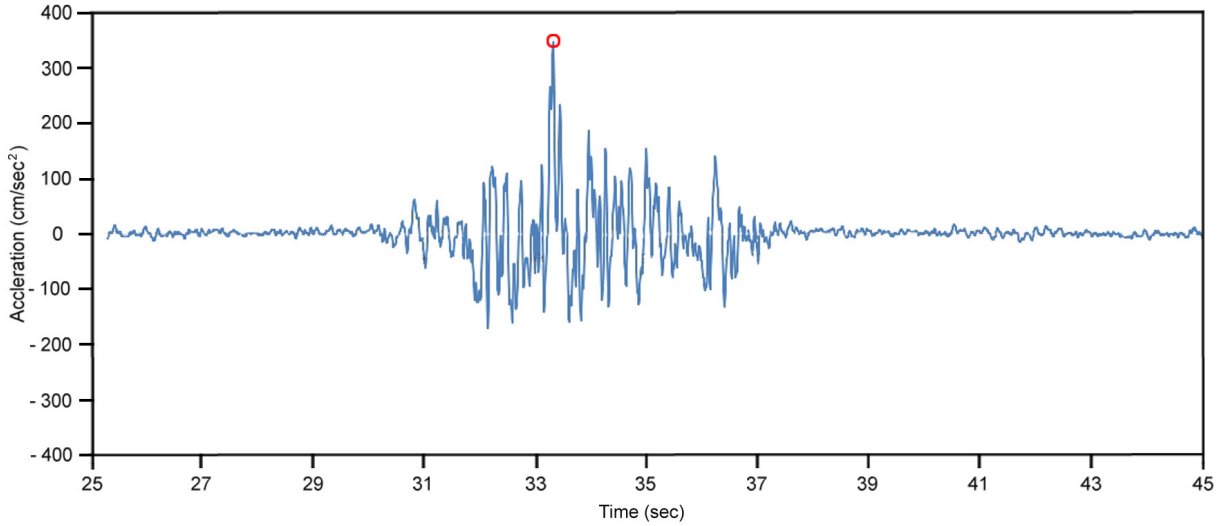

Figure 9. Acceleration time history of the 1822 earthquake at the citadel of Aleppo. This simulated result could be a tentative of reproducing the input motion of this severe earthquake.

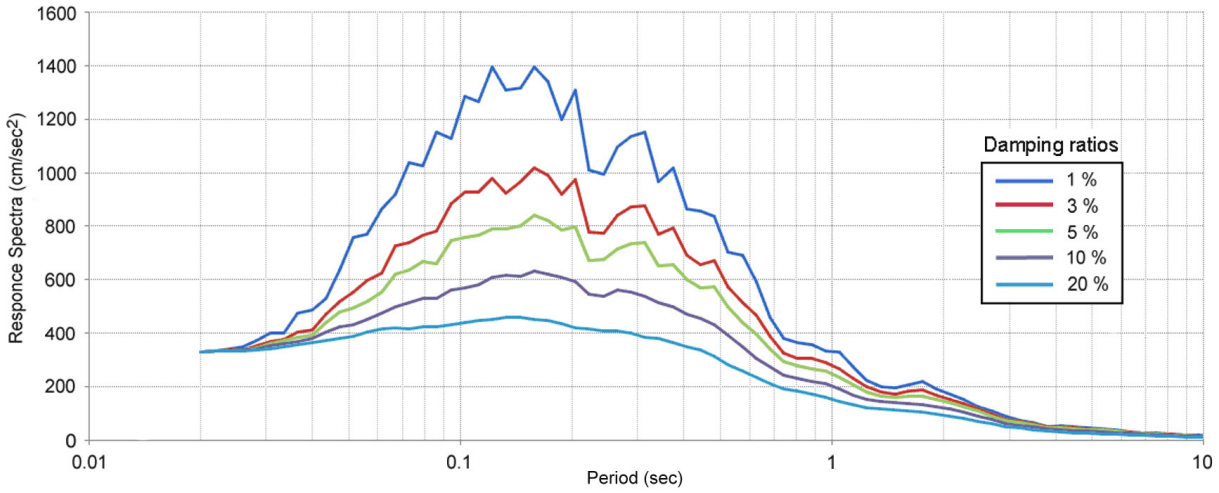

Figure 10. Response spectra of the 1822 earthquake at the citadel of Aleppo for different damping ratios. This simulated result could be a tentative of reproducing the input motion of this severe earthquake.

human losses were not confined to these cities, but rather extended to other cities, towns and villages in northwestern Syria and the adjacent areas in central-southern Turkey as documented in Ambraseys (1989) and Sbeinati *et al.* (2005). Figure 8 shows a map with 63 cities, towns and villages affected by the 1822 earthquake. Furthermore, the intensity isoseismals for the main earthquake were assessed, considering the findings obtained by the results of previous works and by the current study as well. This map is generated by averaging the overall effects of the earthquake. As shown, a vast area in northwestern Syria and some adjacent regions in Turkey were damaged by the 1822 earthquake.

The whole macroseismic data of the 1822 earthquake suggests that the earthquake epicenter is more likely located on the central segment of the St. Simeon fault (SSF) which is located close to Aleppo city. This is attested by the large destruction and loss of life in the city. Although SSF is considered active from the geomorphotectonic evidence, paleoseismic investigation is undoubtedly requested to unveil the rupture of the 1822 earthquake in the sediments.

Some historical sources reported the occurrence of sea waves hitting Cypriot and Syrian coasts following the 1822 earthquake. For example, Neale (1854: xxiii-xxxiv) documented the observation of disturbance of the sea near the coast of Antakia. Also, Conder (1824: 298) mentioned that the earthquake was felt so violently at sea at a distance of about 11 km of Cyprus to the extent that it was thought the ships in Cyprus had grounded. In addition, a rising the rocky masses near Cyprus was documented on 3 September 1822 in a report of a caption of French ship departed from Cyprus to Latakia (Asiatic Journal, 1822: 519). These phenomena could be indirectly related to strong earthquakes such as 1822 earthquake. In this regard, Ambraseys and Barazangi (1989) presented a preliminary explanation about the association of large earthquakes that occurred in land along the DSFS with sea waves in the Syrian coast, stating that these sea waves may be caused by submarine landslides in the Levantine margin due to the presence of layers of Evaporators.

In this research, we use a stochastic finite-fault approach, allowing us to incorporate significant finite-fault effects such as the geometry of larger ruptures and its effects on attenuation, and directivity. The simulations are performed with the computer code EXSIM. Like most other stochastic finite-fault approaches, EXSIM does not assign a directivity effect to individual subfaults, but the effects of rupture propagation along the fault (from subfault to subfault) are assumed to mimic the overall directivity effect (Assatourians and Atkinson, 2007). However, the results of simulation of 1822 earthquake may be considered as a first approach to model the input motion of this severe earthquake. The synthetic accelerogram and response spectra (Figs. 9 and 10) show that the values of acceleration are less than 800 cm/s2 meaning that they are less than 1 g. However, these values could be reasonable regarding the observed damage in Aleppo city due to the 1822 earthquake.

Complementary work should include the use of strong motion records when available and of physical models of propagation, such as site effects, to get a more realistic simulation of this historical earthquake. Small to moderate magnitude events should be recorded at sites where strong motions of the historical events could be simulated. For this purpose, high-resolution strong motion network should be deployed in Syria. In this case, the results of simulation could be employed for conducting dynamic and response spectrum analysis of structures in the damaged regions, for earthquake resistant design.

There is still controversy among some Aleppine researchers on the origin of the disaster that struck Aleppo on the night of August 13, 1822. Some believe that the disaster resulted by a large meteor that fell near the village of Atarib, some 18 km to the west of Aleppo. They support their argument by the existence of a vast hole known as al-Hutah, with dimensions of about 150 meter in diameter, with a maximum depth of 70 meter. In this regard, two clear observations are presented discounting the previous hypothesis; i) The hole itself existed before 1822, as the both Scottish "Alexandar Russell" (1715-1768) and his half-brother "Patrick Russell" (1727-1805), physicians and naturalists of the British business community who lived in Aleppo in the mid-eighteenth century, described the hole (Russell, 1794: 57-58); and ii) the behavior of this natural phenomena, a main large seismic event proceeded by foreshocks and followed by a long series of aftershocks.

Concerning the archaeoseismicity, Kázmér and Major (2010) found traces of two historical earthquakes on the castle of al-Marqab, based on historical and archaeological evidence. The first one is the large magnitude earthquake of 1202 and the second one is related to an earthquake that happened after 1285. As the castle collapsed by the 1822 earthquake, it is believed that the second earthquake may be the 1822 earthquake. On the other hand, many other ruins of archaeological

sites are distributed west and north-west of Aleppo at a short distance from the St. Simeon fault. These sites are part of the so-called the forgotten cities (e.g. Dar Qita, Deir Sita, Barisha, Burj Haidar, Mushabbak Basilica, Qalb Lozeh) flourished in the Byzantine period. Although the historical sources of information were silent on the effects the 1822 earthquake on these sites, Sbeinati *et al.* (1994) considers that these sites should have been strongly affected by the 1822 earthquake since they include strong evidence of seismic scars such as horizontal shifting, waved walls and fractures. However, further investigation is needed.

Based on the results of this study, the 1822 earthquake is named here as "The great Aleppo earthquake", considering that most serious damages and losses of life have concentrated in the city of Aleppo. In addition to the direct effects mentioned in this work, the earthquake caused long-term serious economic impacts. For example, Knost (2010), analyzing the proficiently economic impacts of the earthquake mentioned that the 1822 earthquake was one of the main reasons that contributed in the decline of the trade in Aleppo. Moreover, Bosworth (2007: 11) believes that the trade of goods between Europe and Asia has also declined because of 1822 earthquake in Aleppo.

Conclusion

Based on new contemporary and near contemporary Aleppine, English and French sources of information, this paper describes in detail the 1822 earthquake and its destructive impacts in Aleppo, Antakia, Latakia, and the immediate vicinity. Also, it presents the intensity map of the earthquake and showed the time series of the 1822 earthquakes. Moreover, the earthquake epicenter is suggested on the Saint Simeon fault. Using the stochastic extended simulation method, the strong ground motion of the 1822 earthquake at Aleppo citadel has been simulated.

Aleppo is situated at a very short distance from Antakia triple junction (ATJ). In and around the ATJ, numerous historical destructive earthquakes have occurred such as the last earthquake on 3 April 1872. This means that faults in the ATJ are mostly active and capable of producing large earthquakes. This poses a genuine seismic potential hazards for Aleppo and other cities. If an earthquake like the earthquake of 1822 were to take place in northwestern Syria today, it is expected that the loss of life and damages will be considerably significant due to the large increase in the population and the presence of industrial facilities. Therefore, the results of this work should be of considerable interest in seismic hazard assessment and engineering design for the area.

Acknowledgments

The authors thank Prof. Ibrahim Othman, Director General of the Atomic Energy Commission of Syria (AECS), for his continuous scientific support. We are grateful to anonymous reviewers (Geofísica Internacional) for their helpful comments and suggestions on the manuscript. We also thank both colleagues Drs. Mohamad Reda Sbeinati and Mohamad Al-Hilal (AECS) for their linguistic and scientific comments. Finally, we want to thank Dr. María-José Jiménez for the Spanish translation. Numerous primary sources of information for the 1822 earthquake were obtained from the Google Books Project. This work is a local scientific research no. AECS-G\ RSS 1255/2019.

References

Arabic sources

Aroutine, Paul. 1933. *Ahm Hawadith Halab fi an-Nisf al-Awal min al-Qarn at-Tasea Ashar* [*The most important incidents of Aleppo in the first half of the 19th century*]. Publiées et annotées par L'Appé Paul Cara'li, al-Matba'ah al-Sūrīyah, Misr al-Jadideh.

Bakhkhash, Na'um. 1985. *Akhbar Halab kama katabaha Na'um Bakhkhash fi dafatir al-Jamiyyeh min am 1835 hata am 1875* [*News of Aleppo as written by Na 'um Bakhkhash in the notebooks of the association from 1835 to 1875*]. Qushaqji, Youssef (ed.), Matb'at al-Ihsan, Aleppo.

Al-Ghazzi, Kamil. 1926. *Nahr al-Dhahab fi Tarikh Halab* [*The River of gold in the history of Aleppo*], Part 3, al-Matbaa al-Marouniyeh, Aleppo.

Al-Tabbakh, Mohamad Ragheb. 1925. *I'lam al-Nubala bi Tarikh Halab al-Shahba* [*Informing the nobles in the History of Aleppo*], Part 3, Aleppo.

Taoutel, Ferdinand. 1958. *Watha'iq ta'rikhiyyat an Halap: Akhbar al-mawarinah wa mailayhim min 1606 ila yawmina* [*historical documents on Aleppo: News of Maronites from 1606 to our days*]. Tome 4, al-Matb'ah al-Kathulikiyah, Beyrouth.

English and French sources

Archives des Affaires Étrangères [Forgien Affaires Archives]. 1822. Vol. 26, Paris.

The Asiatic Journal and monthly register for British India and its dependencies. July-December 1822. Syria: Earthquake at Aleppo. Vol. XIV, London.

Barbié du Bocage, Jean-Denis. 1825. Description de la ville de Hhaleb [Description of the town of Aleppo]. Recueil de voyages et de mémoires, Paris: Société de Géographie, Tome II, imprimerie d'Éverat.

Bayford, John (ed.). 1824. *Memoir of the Rev. Joseph Wolff*. London: James Duncan.

Bell, James. 1832. *A system of geography, popular and scientific or a physical, political, and statistical account of the world and its various divisions*. Glasgow: Archiballd Fullarton & Co., Vol. IV.

Bond, Alvan. 1828. *Memoir of the Rev. Pliny Fisk, A.M.: Late Missionary to Palestine*. Boston: Crocker and Brewstar.

Colton, George Woolworth. 1855. *Colton' Atlas of the world illustrating physical and political geography*. Vol. 2, First Edition, NY.

Conder, Josiah. 1824. *The Modern Traveller: Syria and Asia Minor*. Vol. I, London: James Duncan.

Derché. 1824. Relation du tremblement de terre d'Alep par M. Derché, 2e Drogman du Consulat général de France [Report of the Aleppo earthquake by Mr. Derché, 2nd Drogman of the Consulate General of France]. *Bull. Soc. Géogr.*, tome second, Paris.

Gay-Lussac, Joseph Louis, and François Arago. 1822. Annales de Chimie et de Physique, Tome xxi, Chez Crochard, Paris, 395-396.

Gazette Géographique. 1822. Tremblement de terre d'Alep [Earthquake of Aleppo]. Journal des Voyages, Découvertes et Navigations Modernes tome 16 (48): 134-35. Paris: Revue des Deux Mondes. http://www.jstor.org/stable/44868785.

Guys, Charles-Édouard. 1822. Notice sur le tremblement de terre qui a bouleversé la Haute-Syrie en août 1822 [Notice on the earthquake which shook upper Syria in August 1822]. *Bull. Soc. Géogr.*: 301-305, Tome Premier, no 7, Paris.

Michaud, Joseph François, and Jean Joseph François Poujoulat. 1841. *Correspondance d'Orient (1830-1831)* [Correspondance from the East (1830-1831)]. Tome VIII, Bruxelles: Gregoir-Wouters et C^{e}.

Miller, John. 1826. *Awful phenomena of nature, Earthquakes: being an account of the earthquake at Lisbon in 1755, at Caracas in 1812, in Scotland in 1816, and at Aleppo in 1822.* John Cumming, Cheap Tracts, No. 5.

The Missionary Herald. December 1825. *Palestine Mission*. Vol. XXI, No. 12, Boston.

Neale, Frederick Arthur. 1854. Introduction. In *Evenings at Antioch; with sketches of Syrian life*, xxiii-xxxiv. London: Eyre and Williams.

Perrin, N. 1822. Description historique, géographique et statistique de la ville d'Alep et de ses environs [Historical, geographical and statistical description of the city of Aleppo and its surroundings]. *Journal Des Voyages, découvertes et navigations modernes* 16 (48): 5-66. www.jstor.org/stable/44868772.

Purdy, John. 1832. *The new sailing directory for the Strait of Gibraltar and the western division of the Mediterranean Sea: comprehending the coasts of Spain, France, and Italy, from Cape Trafalgar to Cape Spartivento; the Balearic Isles, Corsica, Sardinia, Sicily, and the Maltese Islands; with the African coast, from Tangier to Tripoli, inclusive: including description of the lighthouses and copious tables of positions, or of latitudes and longitudes, of all the principal points &c. also, particular descriptions of the coasts, towns, islands harbours, and anchorages; occasional sketches of national habits and customs; the general products, population, and condition, &c. of the respective places.* London: R.H. Laurie.

Regnault, A.L. (Joseph). 1822. Lettre de M. Le Consul du Roi, Saint-Jean d'Acre, adressée à M. Jomard, Chiti (Chypre), 5 Octobre 1822 [Letter from M. Le Consul du Roi, Saint-Jean d'Acre, addressed to M. Jomard, Chiti (Cyprus), October 5, 1822]. *Bull. Soc. Géogr.*, Tome Premier, Paris, p. 215.

Religious Tract Society. 1822. A true narrative of a most dreadful calamity, the destruction of Aleppo by an earthquake, being an affecting account of the overview of that large an populous city, at midnight, on the 13th of August 1822. No. 566, printed for the Religious Tract Society, London.

Robinson, George. 1837. *Three years in the East being the substance of a journal written during a tour and residence in Greece, Egypt, Palestine, Syria, and Turkey, in 1829-1830, 1831, and 1832*. London: Henry Colburn Henry, et Paris, A. and W. Galignani, 2 vol. in-80, t. I (Palestine), t. II (Syria).

Russell, Alexander. 1794. *The natural history of Aleppo containing a description of the city, and the principal natural productions in its neighborhood*. The Second Edition, revised and enlarged by Patrick Russell, Vol. 1, London: G. G. and J. Robinson.

Volney, Constantin-Françios. 1788. *Travels through Syria and Egypt, in the years 1783, 1784, and 1785*. London: G.G.J. and J. Robinson, Vol. II.

Articles, catalogues and studies

Abdul-Wahed M.K., Asfahani J., 2018, The recent instrumental seismicity of Syria and its implications. Geofs. Int., 57 (2): 79-92, https://doi.org/10.22201/igeof.00167169p.2018.57.2.1655.

Akyuz H.S., Altunel E., Karabacak V., Yalciner C.C., 2006, Historical earthquake activity of the northern part of the Dead Sea fault zone, southern Turkey. *Tectonophysics*, 426: 281-93.

Alissa M., Abdul-Wahed M.K., Shoukeir N., Zeizafoun S., 2021, Empirical relationships for deriving the moment magnitude (MW) for earthquakes in Syria. *Magazine of Albaath-University*, 43 (4), 75-89.

Ambraseys N.N., 1989, Temporary seismic quiescence: SE Turkey. *Geophys. J.*, 96 (2): 311-31.

Ambraseys N.N., 2004, The 12th century seismic paroxysm in the Middle East: A historical perspective. *Ann. Geophys.*, 47 (2-3): 733–58.

Ambraseys N.N., Barazangi M., 1989, The 1759 earthquake in the Bekaa Valley: implications for earthquake hazard assessment in the Eastern Mediterranean region. *J. Geophys. Res.*, 94 (B4): 4007-13.

Ambraseys N.N., Melville C., 1995, Historical evidences of faulting in eastern Anatolia and northern Syria. *Ann. Geophys.*, 38 (3-4): 337-43.

Ambraseys N.N., Jackson J.A., 1998, Faulting associated with historical and recent earthquakes in the Eastern Mediterranean region. *Geophys. J. Int.*, 133 (2): 390–406.

Ambraseys N.N., 2009, Earthquakes in the Eastern Mediterranean and the Middle East: A Multidisciplinary Study of Seismicity up to 1900. Academy of Athens and Cambridge University Press, Cambridge.

Assatourians K., Atkinson G.M., 2007, Modeling variable-stress distribution with the stochastic finite-fault technique. *Bull. Seismol. Soc. Am.*, 97(6), 1935-1949. https://doi.org/10.1785/0120060203.

Atkinson G.M., Assatourians K., 2015, Implementation and validation of EXSIM (A Stochastic Finite-Fault Ground-Motion Simulation Algorithm) on SCEC broadband platform. *Seismol. Res. Lett.*, 86 (1): 48-60.

Atkinson G.M., Assatourians K., Boore D.M., Campbell K., Motazedian D., 2009, A guide to differences between stochastic point-source and stochastic finite-fault simulations. *Bull. Seismol. Soc. Am.*, 99 (6): 3192–3201.

Atkinson G.M., Boore D.M., 2006, Earthquake ground motion prediction equations for eastern North America. *Bull. Seismol. Soc. Am.*, 96: 2181–2205.

Bao X., Sandvol E., Zor E., Sakin S., Mohamad R., Gök R., Mellors R., Godoladze T., Yetirmishli G., Türkelli N., 2011, Pg attenuation tomography within the Northern Middle East. *Bull. Seismol. Soc. Am.*, 101 (4): 1496–1506. doi: https://doi.org/10.1785/0120100316.

Beresnev I.A., Atkinson G.M., 1997, Modeling finite-fault radiation from the ωn spectrum. *Bull. Seismol. Soc. Am.*, 87 (1): 67–84.

Beresnev I.A., Atkinson G.M., 1998, FINSIM-a FORTRAN program for simulating stochastic acceleration time histories from finite faults. *Seismol. Res. Lett.*, 69 (1): 27–32.

Beresnev I.A., Atkinson G.M., 1999, Generic finite-fault model for ground-motion prediction in eastern North America. *Bull. Seismol. Soc. Am.*, 89: 608–25.

Boore D.M., 1983, Stochastic simulation of high-frequency ground motions based on seismological models of the radiated spectra. *Bull. Seismol. Soc. Am.*, 73 (6A): 1865–94.

Boore D.M., 2003, Simulation of ground motion using the stochastic method. *Pure Appl. Geophys.*, 160: 635–76.

Boore D.M., Joyner W.B., 1997, Site amplifications for generic rock sites. *Bull. Seismol. Soc. Am.*, 87 (2): 327–41.

Bosworth C.E. (ed.), 2007, Historic Cities of the Islamic World. Leiden-Boston, Brill.

Capar A., 2017, A portrayal of an Ottoman city and its inhabitants: administration, society and economy in Ottoman Antakya (Antioch) 1750-1840. PhD Dissertation, University of Arkansas.

Darawcheh R., Abdul-Wahed M. K., Hasan A., 2019, The 1822 Aleppo Earthquake: Implications for the Seismic Hazard Assessment at the Antakya Triple Junction, N. Sundararajan *et al.* (eds.), On Significant Applications of Geophysical Methods, Advances in Science, Technology & Innovation, https://doi.org/10.1007/978-3-030-01656-2_40.

Al-Ghunaim A.Y., 2002, Earthquakes in Arab Records: their Events and Effects in Arab Resources. First edition. Kuwait: Kuwaiti Geographic Society.

Grünthal G. (ed.)., 1998, European Macroseismic Scale 1998 (EMS98). Luxembourg: Centre Européen de Géodynamique et Séismologie.

Guidoboni E., Bernardini F., Comastri A., 2004, The 1138-1139 and 1156-1159 destructive seismic crises in Syria, south-eastern Turkey and northern Lebanon. *J. Seismol.*, 8: 105-27.

Historical Digital Documentation House (www.dig-doc.org). https://www.facebook.com/pg/digdoc.net/about/?ref=page_internal

Honoré L., Courboulex F., Souriau A., 2011, Ground motion simulations of a major historical earthquake (1660) in the French Pyrenees using recent Moderate size earthquakes. *Geophys. J. Int.*, 187 (2): 1001-18.

Ibrahim R., Hiroshi T., Daoud M., Hara T., 2012, 1-D velocity model for Syria from local earthquake data and new seismicity map in Syria. *Bulletin of IISEE*, 46, 121-137.

IAEA (International Atomic Energy Agency), 1987, Methodology and procedures for compilation of historical earthquakes data. IAEA-TECDOC-434, Vienna.

ISC (International Seismological Center). http://www.isc.ac.uk/iscbulletin/search/bulletin/

El-Isa Z., Mechie J., Prodehl C., 1987, Shear velocity structure of Jordan from explosion seismic data. *Geophys. J. R. Astr. Soc.*, 90 (1): 265-81.

Jackson J., McKenzie D., 1988, The relationship between plate motions and moment tensors, and the rates of active deformation in the Mediterranean and Middle East. *Geophys. J. Int.*, 93 (1): 45-73.

Kanamori H., Anderson D.L., 1975, Theoretical basis of some empirical relations in seismology. *Bull. Seism. Soc. Am.*, 65 (5): 1073–95.

Karakhanian A.S., Trifonov V.G., Ivanova T.P., Avagian A., Rukieh M., Minini H., Dodonov A.D., Bachmanov D.M., 2008, Seismic deformation in the St. Simeon monasteries (Qal'at Sima'n), northwestern Syria. *Tectonophysics*, 453 (1): 122-47.

Kázmér M., Major B., 2010, Distinguishing damages from two earthquakes-Archaeoseismology of a Crusader castle (Al-Marqab citadel, Syria). In Sintubin, M., Stewart, I.S., Niemi, T.M., and Altunel, E. (eds.), Ancient Earthquakes, Geological Society of America Special Paper 471, pp. 185–98.

Knost S., 2010, The impact of the 1822 earthquake on the administration of *Waqf* in Aleppo. In Syria and Bilad al-Sham under Ottoman rule: assays in honor of Abdul-Karim Rafeq, ed. Peter Sluglett and Stefan Weber, 293-305. Leiden; Boston: Brill.

Leonov Y.G. (ed.), 1989, The Tectonic Map of Syria, scale 1:500,000. Ministry of Petroleum and Mineral Resources of the Syrian Arab Republic and Academy of Sciences of the USSR.

Mallet R., Mallet J.W., 1858, The Earthquake Catalogue of the British Association: with the Discussion, Curves, and Maps, etc. London: Taylor and Francis.

McClusky S., Balassanian S., Barka A., Demir C., Ergintav S., Georgiev I., Gurkan O., Hamberger M., 2000, Global Positioning System constraints on plate kinematics and dynamics in the eastern Mediterranean and Caucasus. *J. Geophys. Res.*, 105 (B3): 5695-5719.

Mechie J., Abu-Ayyash K., Ben-Avraham Z., El-kelani R., Mohsen A., Rümpker G., Saul J., Weber M., 2005, Crustal shear velocity structure across the Dead Sea Transform from two-dimensional modelling of DESERT project explosion seismic data. *Geophys. J. Int.*, 160 (3): 910-24.

Mitchell B.J., Pan Y., Xie J., Cong L., 1997, Lg coda Q variation across Eurasia and its relation to crustal evolution. *J. Geophys. Res.*, 102, 22767-779.

Mohamad R., Al-Samara M., Sandvol E., 2012, Seismic tomography and its implication structures using regional seismic phase recorded in Syrian national seismic network and surrounding networks. *Journal of Engineering Sciences*, Assiut University, 40 (1): 45-65.

Motazedian D., Atkinson G.M., 2005, Stochastic finite-fault modeling based on a dynamic corner frequency. *Bull. Seismol. Soc. Am.*, 95 (3): 995–1010.

Över S., Ünlügenç U.C., Bellier O., 2002, Quaternary stress regime change in the Hatay region (SE Turkey). *Geophys. J. Int.*, 148 (3): 649-62.

Over S., Kavak K. Ş, Bellier O., Özden S., 2004, Is the Amiq Basin (SE Turkey) a triple-junction area? Analyses of SPOT XS imagery and siesmicity. *International J. Remote Sens.*, 25 (19): 3857-72.

Raymond A., 2010, Aux origines du la plan d' Alep par Rousseau: le plan de Vincent Germain de 1811 [At the origins of the plan of Aleppo by Rousseau: the plan of Vincent Germain of 1811]. In Syria and Bilad al-Sham under Ottoman rule: assays in honor of Abdul-Karim Rafeq, eds. P. Sluglett, and S. Weber, 499-512. Leiden Boston: Brill.

Saragoni G.R., Hart G.C., 1974, Simulation of artificial earthquakes. *Earthq. Eng. Struct. Dyn.*, 2: 249-67.

Sbeinati M.R., Darawcheh R., Mouty M., 1994, Field archaeological evidences of seismic effects in Syria. In Historical Investigation of European Earthquakes: Materials of the CEC Projects, 2, ed. P. Albini and A. Moroni, 195-203. Milano: CNR.

Sbeinati R., Darawcheh R., and Mouty M., 2005, The historical earthquakes of Syria: an analysis of large and moderate earthquakes from 1365 B.C. to 1900 A.D. *Ann. Geophys.*, 48 (3): 347-435.

Steck L. K., Philips W. S., Mackey K., Begnaud M. L., Stead R. J., Rowe C. A., 2009, Seismic tomography of crustal P and S across Eurasia, *Geophys. J. Int.*, 177: 81–92.

Talas M.A., 1956, Al-Athar al-Islamiyya wa at-Tarikhiyyah fi Halab [Islamic and historical monuments in Aleppo]. Damascus: Directorate General of Antiquities.

Tari U., Tüysüz O., Gençe Ş.C., İmren C., Blackwell B.A.B., Lom N., Tekeşin Ö., Üsküplü S., Erel L., Altıok S., Beyhan M., 2013, The geology and morphology of the Antakya graben between the Amik triple junction and the Cyprus Arc. *Geodin. Acta.*, 26 (1-2): 27-55.

Westaway R., 1994, Present-day kinematics of the Middle East and Eastern Mediterranean. *J. Geoph. Res.*, 99: 12071-90.

Zengin E.Ç., Çaktı E., 2014, Ground motion simulations for the 23 October 2011 Van, Eastern Turkey earthquake using stochastic finite fault approach. *Bull. Earthq. Engin.*, 12: 627-46.

Original paper

https://doi.org/10.22201/igeof.00167169p.2022.61.3.2200

Relation of Shear Wave Velocity Variations with Depth for Different Lithologies: A Contribution Towards Mitigating the Region's Seismic Risk

Jyoti Singh[1], A. Joshi*[1], Mohit Pandey[1], Saurabh Sharma[1], Sandeep Singh[1], Sanjay[1], Sohan Lal[1], N. K. Samadhiya[2], Anamika Sahu[1], Himanshu Badoni[3], Sumit Jain[3], Janeet Sharma[3], Praful Ramola[3], Vijay Dangwal[3]

Received: November 16, 2021; accepted: May 24, 2022; published on-line: July 1, 2022.

Resumen

El estado de Uttarakhand en la India se encuentra en una zona de alta actividad sísmica, por lo que se han seguido criterios de diseño resistentes a los terremotos para las principales prácticas de construcción en esta región. Una de las principales entradas para el diseño resistente a los terremotos es la velocidad media de la onda de corte (V_S) a 30 m de profundidad. En el presente trabajo, en veintiséis sitios diferentes, la técnica de la relación espectral horizontal a vertical (HVSR) y el análisis multicanal de onda de superficie (MASW) se utiliza para el análisis conjunto para obtener un modelo de velocidad unidimensional que soporta tanto la curva de espectro de HV como la curva de dispersión obtenida de los métodos HVSR y MASW, respectivamente. Los perfiles de onda de corte obtenidos en varios sitios se comparan con los datos de registro de perforación obtenidos de la perforación y muestra claramente que los V_s para la misma formación tienen una fuerte dependencia de la profundidad en la que ocurrió. Se han utilizado datos de veinticuatro perfiles de onda de corte para preparar una relación de regresión lineal de V_s para diferentes formaciones litológicas con respecto a su profundidad de ocurrencia. El error cuadrático medio obtenido a partir de la relación desarrollada para varias litologías muestra claramente que los resultados están bastante bien dentro del rango de aceptación. Las relaciones desarrolladas han sido validadas adicionalmente por el cálculo de perfil V_s de los datos de registro de perforación obtenidos en dos nuevos sitios de ubicación que no están incluidos en el conjunto de datos utilizado para la preparación de relaciones de regresión. Una comparación de dos secciones de velocidad muestra claramente que el perfil de velocidad calculado a partir de la relación de regresión coincide estrechamente con el obtenido de la encuesta sísmica y por lo tanto se establece la eficacia de la relación de regresión desarrollada para su implementación práctica. Esta relación desarrollada permite la clasificación del tipo de suelo para fines de zonificación.

Palabras Clave: Relación espectral H/V, MASW, velocidad de onda de escucha y relación de regresión

Editorial responsibility: Anonymous

**Corresponding author at joshi.anand@es.iitr.ac.in*

[1]Department of earth sciences, IIT Roorkee

[2]Department of civil engineering, IIT Roorkee

[3]Rail Vikas Nigam Limited, Rishikesh

Abstract

The state of Uttarakhand in India lies in a highly seismically active zone, therefore earthquake resistant design criteria have been followed for major construction practice in this region. One of the major inputs for earthquake-resistant design is average shear wave velocity (V_S) at 30 m depth. In the present work, at twenty-six different sites, the Horizontal to vertical spectral ratio (HVSR) technique and multichannel analysis of surface wave (MASW) is used for joint analysis to obtain a one-dimensional velocity model that supports both the HV spectrum and dispersion curve obtained from HVSR and MASW methods, respectively. Shear wave profiles obtained at various sites are compared with the bore log data obtained from drilling and it clearly shows that the (V_S) for the same formation have a strong dependence on the depth at which it occurred. Data from twenty-four shear wave profiles have been used to prepare a linear regression relation of (V_S) for different lithological formations with respect to their depth of occurrence. Root mean square error obtained from the developed relationship for various lithologies clearly shows that the results are fairly well within the range of acceptance. The developed relations have been further validated by calculating V_s profile from bore log data obtained at two new location sites that are not included in the data set used for the preparation of regression relations. A comparison of two velocity sections clearly shows that the velocity profile computed from regression relation matches closely with that obtained from the seismic survey and thereby establishing the efficacy of developed regression relationship for its practical implementation. This developed relation allows soil type classification for zoning purposes.

Key words: H/V Spectral ratio, MASW, Shear wave velocity and regression relation.

Introduction

Shear wave velocity plays an important role in designing the earthquake-resistant structure for any major engineering construction. Average shear wave velocity at thirty-meter depth (V_{S30}) that is calculated from the shear wave velocity profile is a major requirement for designing an earthquake-resistant structure. The dynamical properties of the local subsoil are a major requirement for the design of earthquake-resistant structures (Amico *et al.*, 2008, Kramer, 1996). This information can be obtained through invasive and time-consuming techniques like drilling, down/cross-hole measurements, etc. These, however, supply local information, and a satisfactory survey may result very expensive, preventing their widespread application (Amico *et al.* 2008). Additional problems arise when urban areas or inaccessible terrain are of concern, where invasion is generally made difficult by buildings or highly inaccessible terrain. This need has resulted in the development of a fast and cost-effective quantitative method aiming at the seismic characterization of subsoil over wide areas by the use of non-invasive procedures (Amico *et al.*, 2008). Active and passive seismic techniques represent a good opportunity in this direction. Because of their importance, these methodologies have been recently the object of active research in the seismological (e.g., the Site Effects Assessment using Ambient Excitations [SESAME] European project, http://sesame fp5.obs.ujf grenoble.fr/index.htm, last accessed March 2008) and engineering (North Atlantic Treaty Organization [NATO] SfP Project 980857, http://nato.gfz.hr, last accessed March 2008) field.

The geotechnical and seismic characterization of shallow soil can be made by the analysis of the surface and interface waves. Through the analysis of the dispersion properties of Rayleigh, Love, Scholte, or Stonely waves, it is possible to retrieve shear-wave velocity profiles in any region. This can be done by using waves generated from active sources as in Spectral Analysis of Surface Waves

(SASW, Nazarian and Stokoe, 1984), Multichannel Analysis of Surface Waves (MASW, McMechan, and Yedlin, 1981; Park *et al.*, 1999), Multiple Signal Classification (MUSIC, Schmidt, 1986), Multi-Offset Phase Analysis Of Surface Wave Data (MOPA, Strobbia, and Foti, 2006), and similar geotechnical approaches (Mulargia *et al.*, 2015) or waves from passive ambient noise, as in the 2D arrays of Spatial Autocorrelation method (SPAC, Aki, 1957) and Extended Spatial Autocorrelation Method (ESAC, Ohori *et al.*, 2002) or in the 1D of Refraction Microtemor™ (ReMiTM, Louie, 2007) and Statistical Self Alignment Property (SSASP, Mulargia and Castellaro, 2013). Although the dispersion curve gives better results there is always chance of error in using the dispersion curve as the sole criteria due to constraints in high-frequency sources and limitations in inversion strategy.

The HVSR method, proposed by Nogoshi and Igarashi (1970) and promoted by Nakamura (1989), and standardized within the SESAME Project (2004), is the most common technique to experimentally assess the subsoil resonance (i.e., amplification) frequencies. In recent years, the joint fit of HVSR and dispersion curves have been proposed by, Parolai *et al.*, 2005; Picozzi *et al.*, 2005; Castellaro and Mulargia, 2010, 2014; Roser and Gosar, 2010; Zor *et al.*, 2010; Foti *et al.*, 2011. The joint fit of the HVSR and dispersion curve are considered better constrained than models based on the match of the curve from a single technique (Castellaro, 2016). A reliable estimate of the shear wave profile obtained at any site can give an accurate estimate of earthquake-resistant design parameters. Shear wave velocity is a diagnostic engineering tool because of its dependence on pore saturation and is considered an important tool in designing buildings for site-specific conditions such as soil liquefaction, ground-spectral earthquake response, etc. (Gorstein and Ezersky, 2015).

The state of Uttarakhand in India falls in the highest vulnerable zone IV of the seismic zonation map of India. Besides being a major source of tectonic earthquakes, it is a locale of many turbulent rivers and tourist destinations. Due to its techno-economic importance to the region, the whole area is a locale of many ongoing major civil projects including major railway projects proposed from Rishikesh to Karnaprayag. The shear wave velocity profile in this has been estimated using non-invasive active and passive seismic methods which include methods dependent on HVSR and dispersion curves. Geological bore logs in this area at the site of seismic investigation have helped in constraining the model obtained from the joint fit of dispersion and HVSR curves. The main objective of this paper is to present a detailed analysis of the shear wave profile obtained at various sites in this project and present the relation of shear wave velocity with rock type obtained at different depths for estimation of the seismic section from rock type exposed in this part of Himalayan Terrain and thus can be used for mitigating region's seismic risk.

Geology of Region

In the Garhwal Himalaya, litho-tectonic units range in age from Precambrian metamorphic to Neogene sediments (Khattri et.al,1989). The Alaknanda River traverses through these litho-tectonic units in the Garhwal Himalaya. The Garhwal Himalaya, drained by the Yamuna, the Bhagirathi, and the Alaknanda rivers constitutes the middle part of Burrard's and Gansser's Kumaun Himalaya extending from the Sutlej to the Kali river (Khattri et.al, 1989). Garhwal Himalaya, comprising the central portion of the Himalaya, is a seismically active region of the Indian subcontinent. It is characterized by the presence of two active fault systems, namely, the Main Boundary Thrust (MBT) and Main Central Thrust (MCT), along with several minor tectonic lineaments.

The main rock types in this area are quartzite, phyllite, meta-volcanic, meta basics, and dolomites with strike directions varying from NE-SW to NW-SE. The geological map of the region together with the study area is shown in Figure 2. Quartzites are the major rock type in the area, followed by phyllites and other rocks. Quartzites and dolomites are generally hard and massive in this region except in places where thrust, fault, or shear zones are present. Phyllites and meta basics are of lower strength and have been reduced to powdery material near shear zones. In general, phyllites occupy the southern part of the area close to the North Almora Thrust (NAT) and are commonly crushed, sheared, and crumpled into numerous folds, whereas the quartzites are hard and compact with joints and fractures (Sarkar *et al.*, 1995). A detailed geological map of the study area together with the location of boreholes at which bore log data is available is shown in Figure 2.

Estimation of Shear Wave Velocity

One of the most common methods of obtaining shear wave velocity is based on ambient micro-tremor data. The micro-tremor data is recorded at each site by a three-component sensor having a natural frequency, which is designed to record the ambient noise. Out of three components, the vertical component is free from any kind of site effect and contains information about the anthropic activity (>2Hz) (Castro et. al., 1997). The ratio of Fourier spectra of horizontal with vertical motion carries site information. This method is popularly known as the HVSR technique. Nakamura (1989) proposes the Horizontal to Vertical Spectral Ratio (HVSR) technique, which is a non-invasive technique in the geophysical field, which gives us the shear wave velocity structure. In addition, due to its low cost, this technique is extensively used in the study of ground motion amplification at a site and gives the resonant frequency of the subsoil layer. HVSR technique is applied over a wide area of ground motion amplitude in the range from micro-tremor to strong motion (both ambient noise and weak motion recordings). Nakamura (1989) assumed that the ambient noise is generally composed of body waves but there are other cases where the ambient noise is treated as fully composed of SH waves (Mucciarelli and Gallipoli, 2004) and surface waves (Rayleigh and Love wave) (Fäh *et al.* 2001, Lachet and Bard, 1994). However, the surface wave content in the ambient seismic noise has been adopted in the present study and the analysis of the HVSR curve has been done accordingly.

The ratio of amplitude spectra of horizontal and vertical components constitutes the HVSR curve. This ratio has effective normalization power which removes the effect of the source and intensifies the subsoil response (i.e. path) (Nogoshi and Igarashi, 1970; Nakamura, 1989). The HVSR curve results in a peak in which the peak frequency indicates the resonant frequency (f_0) and peak amplitude indicates the amplification factor. The relation between resonant frequency (f_0), shear wave velocity (V_S) and thickness of layer (H) is given as:

$$f_0 = \frac{V_S}{4H} \tag{1}$$

Where,

f_0 is the resonant frequency of the subsoil layer (Hz),

V_S is the shear wave velocity of the subsoil layer (m/s),

H is the thickness of the layer (m).

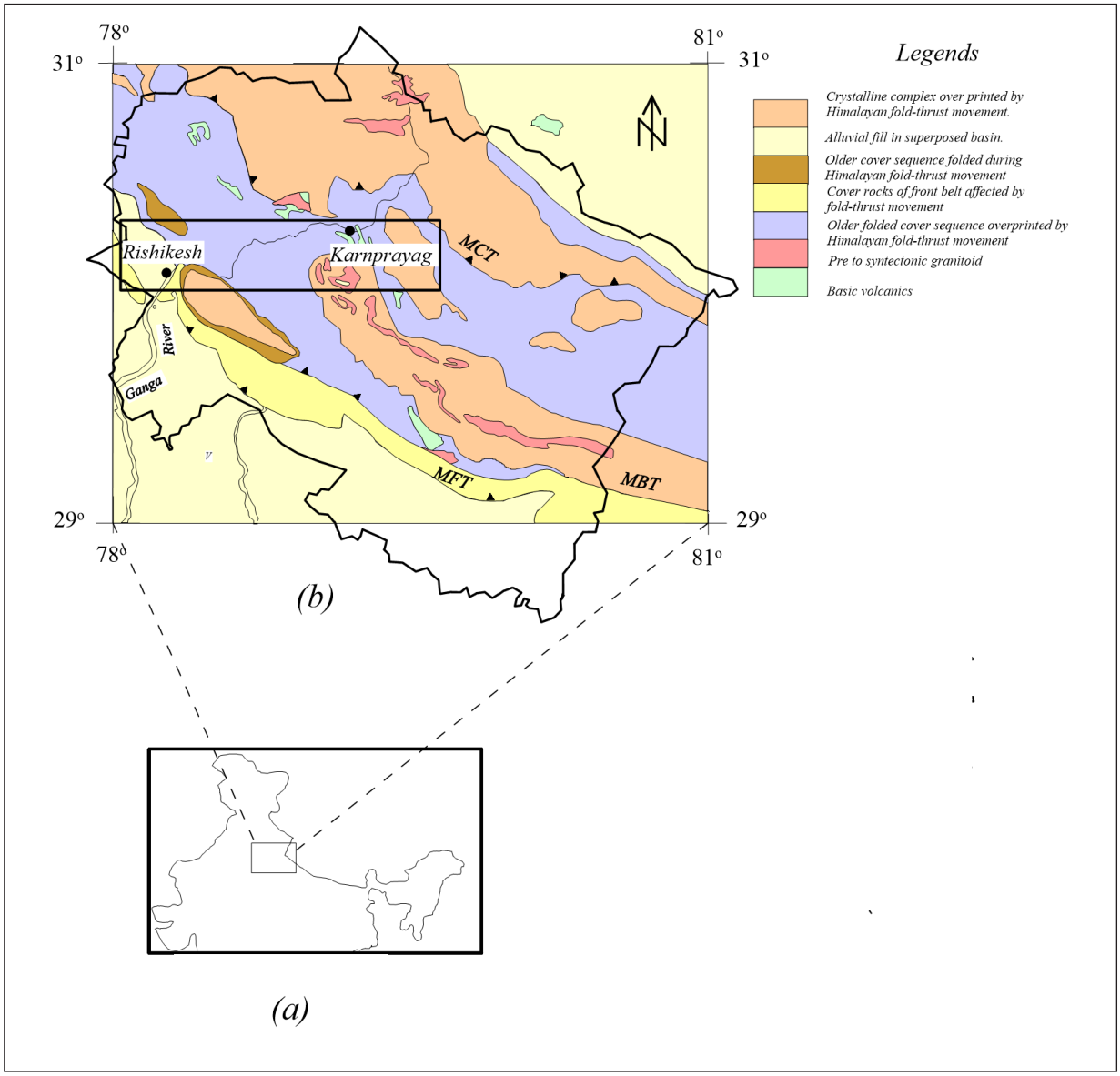

Figure 1. Geological map of Uttarakhand Himalayas with the study area shown in a rectangular block.

When the HVSR curve has only one single peak, it gives the correct amplification value. In the case of several peaks, the peak at the lowest frequency is the fundamental mode and the other peaks are due to the other lithologies, which cause amplification (Tsuboi *et al.*, 2001).

In this paper, the TROMINO instrument is used as the sensor for acquiring the data. The data is generally recorded for a time length and is acquired at both ends of the linear array. In this work, GRILLA software designed by MOHO Science & Technology Company, Italy has been used for processing micro-tremor data. Fourier Spectra of all the three components of recorded ground motion are calculated and the average of two horizontal components is estimated as shown in Figure 3(b). The ratio of average horizontal spectra with vertical spectra using eq. (1) gives the HVSR spectral ratio as shown in Figure 3(c). The portion of ambient noise data utilized for the HVSR study has been from the frequency-time plot of HVSR data of complete record shown in Figure 3.

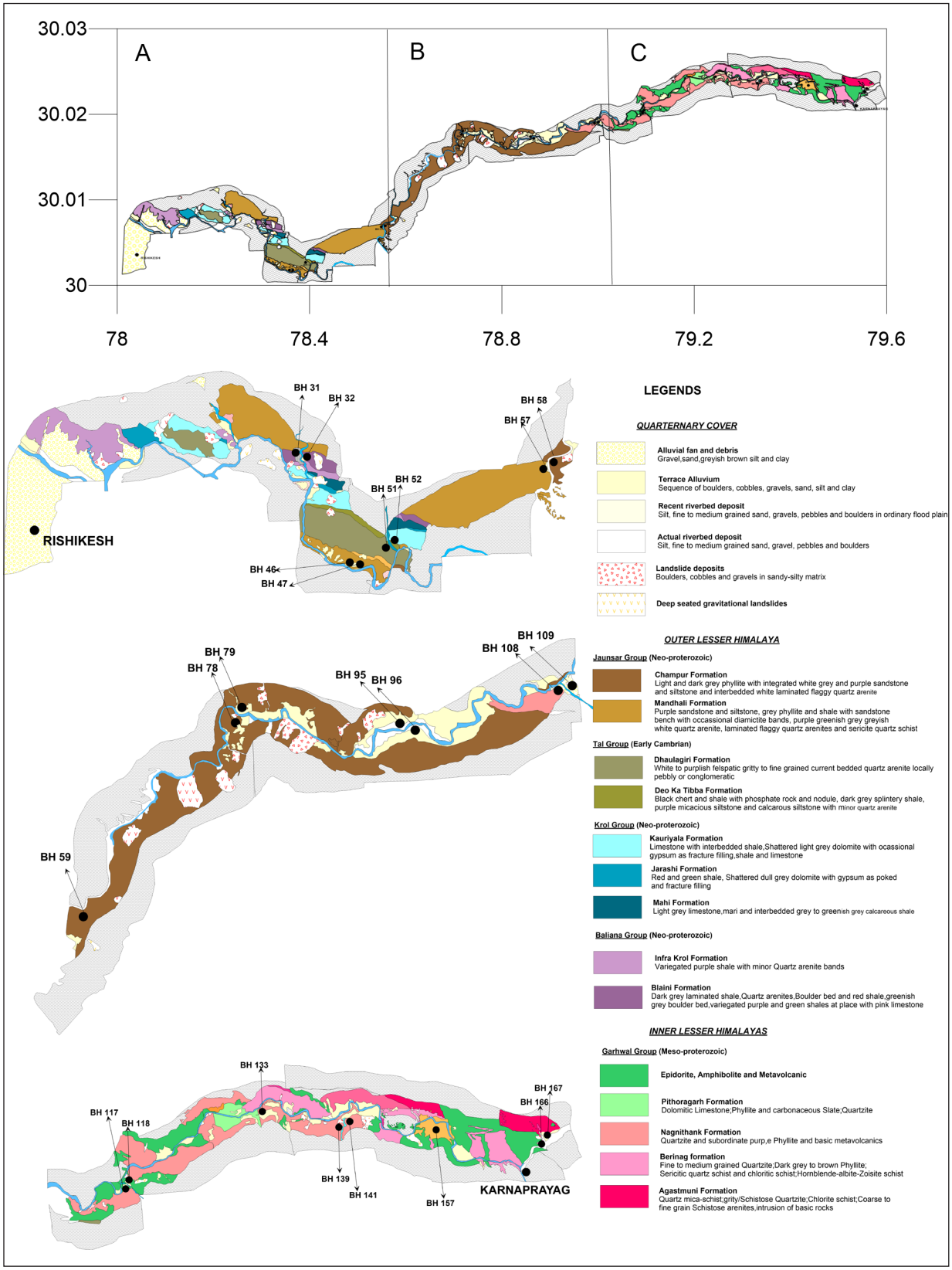

Figure 2. Location of boreholes on the geological map in the study area is shown by a rectangle in Figure 1.

Direct inversion of HVSR curves gives the shear wave velocity model but it requires knowledge of soil parameters (e.g. Poisson's ratio and damping constant in each layer) which is not an easy task to determine. The inversion process also requires the initial model for the construction of the shear wave velocity model. The non-uniqueness in the solution obtained from HVSR inversion can be constrained by jointly fitting the HVSR curve with the dispersion curve obtained from the method commonly known as MASW. MASW is a geophysical method that is used for the estimation of shear wave velocity profile. This technique uses the property of dispersion of surface waves in elastic media. The basis of all of these techniques is the slant stack (or the correlation) of the signal recorded from different receivers, which permits the determination of the propagation velocity of waves of different frequencies travelling between them. In this method, the seismic signal is recorded at different positions (a minimum of two) over time (Figure 4a). The recorded signals are processed by slant stack and fast Fourier transform (FFT) procedures to produce the so-called phase/ group velocity spectra or dispersion curve (Figure 4b). The slant-stack adds traces by shifting it in time in proportion to its offset. The FFT of the traces produces the phase velocity spectra. Phase velocity spectra indicate the most probable velocity of the surface waves at each frequency. From this curve, a forward or inverse modeling procedure is applied to reconstruct a shear wave velocity model for the surveyed area (Figure 4c). The shear wave velocity is linked to the Rayleigh and Love wave velocity (normally 10%–15% larger) through the Poisson's ratio, as formulated in the elastic theory of waves (Castellaro, 2016). These dispersive waves propagate with different velocities. Long-wavelength propagates with higher velocities due to its propagation from the deeper part of the earth and vice versa. Surface waves have high signal-to-noise (S/N) ratio, therefore it is used to characterize near-surface structures.

In the present work, seismic signals have been recorded at different receiver positions using a sledge-hammer of 8 kg weight. The time series recorded at different positions of receivers in increasing order is shown in Figure 4a. The dispersion of the surface wave is visible in the enlargement of the wave packet shown in a quadrilateral window in Figure 4b. The slant stack and Fast Fourier transform have been applied to obtain the dispersion curve of the Rayleigh wave shown in Figure 4c. Ubiquitous ambient noise data recorded from a passive source (Figure 4d) at the same site has been used for estimation of the HVSR curve (Figure 4e) using the Fast Fourier Transform of the recorded signal. In this work, the seismic traces are analyzed using GRILLA software, which generates the dispersion curve. An initial velocity model is heuristically selected to obtain a theoretical HVSR and dispersion curve, which matches with field data shown in Figure 4e and c, respectively. The GRILLA software models the HVSR and dispersion curve using the forward approach by visually fitting both curves. MASW gives the best estimation of shear wave velocity at shallow depths but it does not give information about deeper parts. Therefore, it is generally modeled together with the HVSR curve to get a better-constrained shear wave velocity structure. Experimental evidence indicates that the active techniques usually provide better results in the high-frequency range, that is, shallow depth. The passive techniques that rely on ubiquitous ambient noise have the theoretical potential to perform better in the mid-to-low frequency range that is pertinent to mid-to-large depths (Castellaro, 2016). Therefore, both active and passive technique used in this paper provides reliable results in both shallow and intermediate depths.

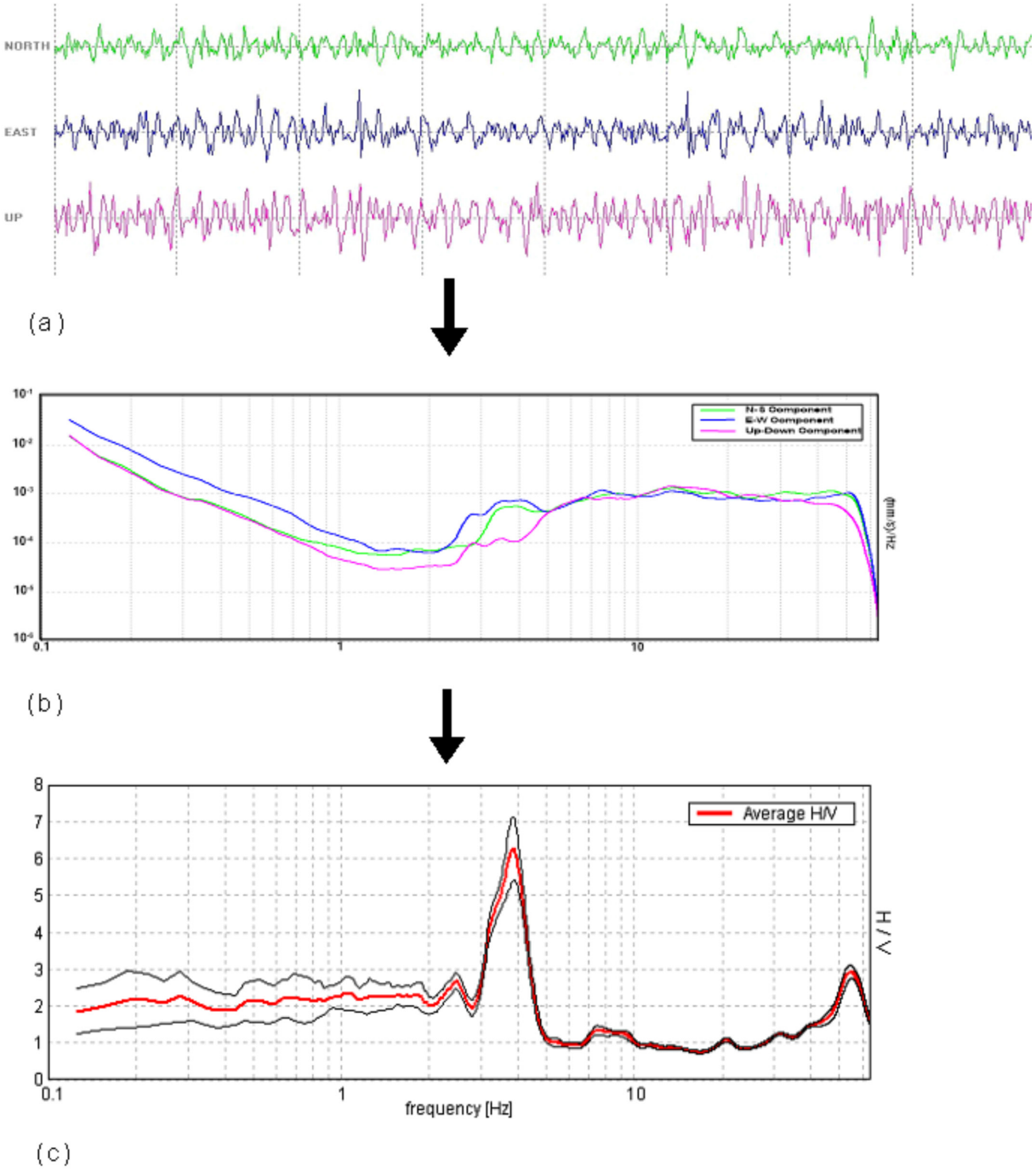

Figure 3. (a) Three-component record of ambient noise (b) The Fourier spectra of the recorded ambient noise (c) The horizontal to vertical spectral ratio (HV) curve.

Data Acquisition and Analysis

The study area is located in the state of Uttarakhand, India, and is shown in Figure 1. Borelog data at those sites at which seismic data using MASW and HVSR survey has been collected is shown in Figure 2. Logs have been obtained using the method of drilling. Twenty-four sites that contain geological logs have been used in this work. The data has been acquired by the TROMINO (MOHO s.r.l.) instrument to study the velocity variation at a site using joint inversion of HVSR and dispersion curve. It is a high-resolution all-in-one system for passive and active seismic surveys and vibration monitoring. It is equipped with 3 channel recording with a frequency range from 0.1-1024 Hz. The same instrument has been used to record the ambient noise and active MASW data. In the present study, the ambient noise data has been recorded for a time window of 8-10 minutes at a sampling rate of 128 Hz. This data has been further analyzed by dividing the time window into 20s duration by taking data free from anthropogenic noise. After that data has been further corrected for baseline correction using a triangular window. The resonance frequency is obtained by averaging the HVSR curves from all windows using the Nakamura technique (Nakamura, 1989). Similarly, MASW data has been recorded at each site at a sampling rate of 512 Hz. In this survey, the TROMINO is placed at a fixed position and the source has been moved to different offsets of equal intervals (1-3 m). The Sledgehammer of 8 kg and an iron plate have been used as a source and at each shot, the trigger is used. Geological samples obtained from bore log data include sandstone, clayey sand, boulders of quartzite, and phyllite with various combinations.

Shear wave velocity profiles have been obtained from the data collected by ambient micro-tremor recording instrument, using an active and passive seismic method at twenty-four different sites. In the present work, joint inversion of the HV curve and dispersion curve has been made by using GRILLA software and is shown in Figure 5. Different modes of dispersion curves have been observed in the data taken in the present study. However, the dispersion curve corresponds to the fundamental mode that has been selected for the analysis. The curve presenting the low-velocity values at each frequency is selected as a fundamental mode. In Rayleigh wave arrays, the depth of investigation is proportional to the maximum exploring wavelength divided by a number comprised between 2 and 3 (where the exact value depends on the Poisson's ratio (Jones, 1958, 1962; Abbiss, 1981). The maximum exploring wavelength is derived from the phase velocity spectra by dividing the (usually maximum) correlation velocity by the corresponding frequency. As an example, in Figure 12a, the maximum velocity that can be observed from the dispersion curve is 250m/s at 5 Hz, which equates to a wavelength λ of 250/5=50 m and a depth of exploration of approximately 50/2.5=20 m. The velocity model up to the depth of 20 m is well explained by the joint fit of HVSR and dispersion curve and below this depth, only the HVSR curve is accountable for obtained velocity model.

The shear wave velocity section obtained from joint inversion is correlated with lithologs obtained from borehole data at twenty-four stations. The correlation of lithologs with obtained shear wave seismic profile at twenty-four stations is shown in Figures 6-9.

Regression Model

Rock samples obtained from various logs at different stations clearly shows that similar rock type can be found at different depths, which can result in different shear wave velocities of similar rock type due to difference in their formation condition. As the modulus of rigidity increases with depth,

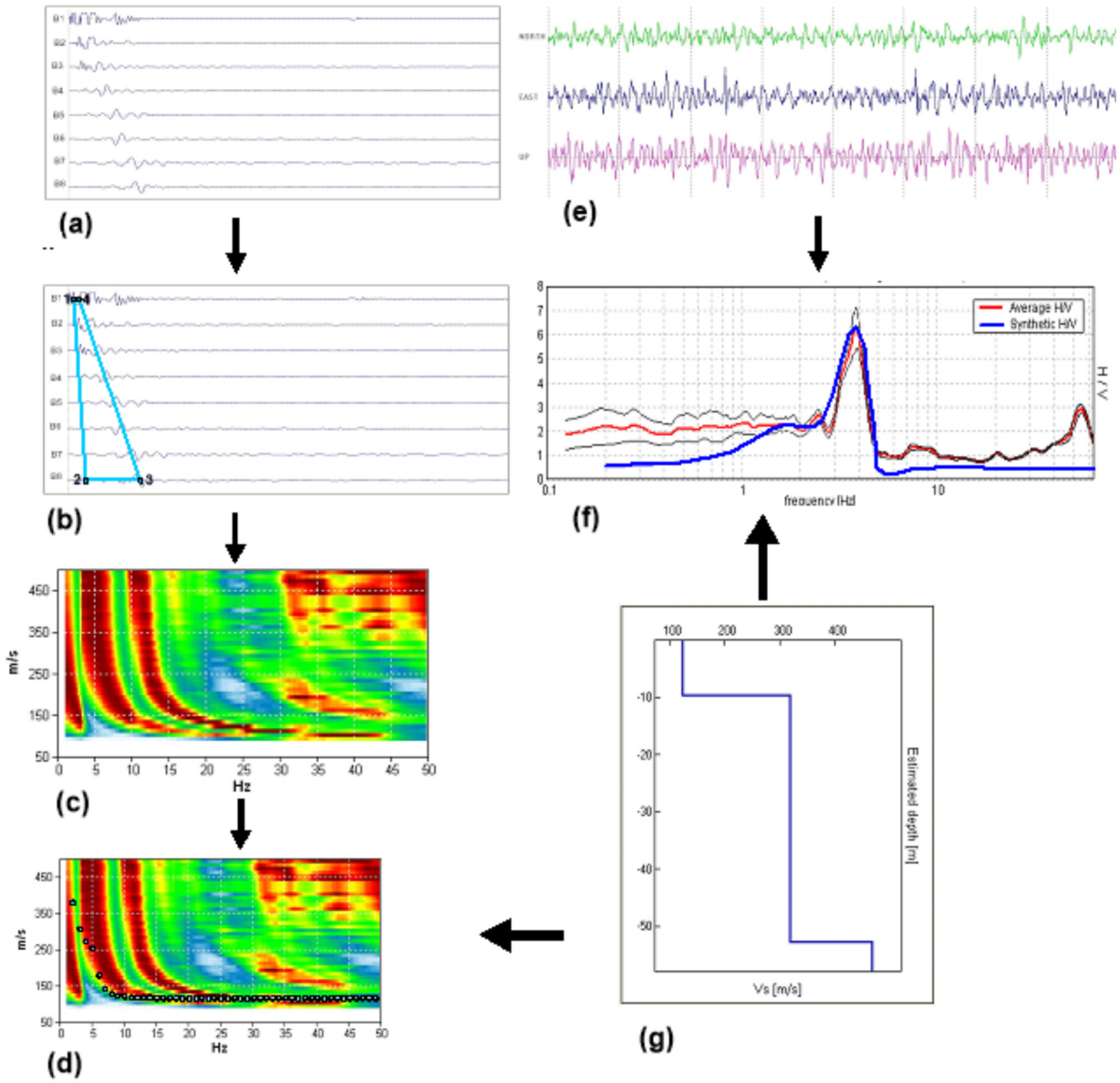

Figure 4. (a) Recorded traces at different receivers in the increasing order of distance (b) Selection of window (c) Rayleigh wave phase velocity spectra obtained from the selected window (d) Theoretical dispersion curve selected for velocity model (e) Three-component record of ambient noise. (f) HV curve from the amplitude spectra of the ambient noise (g) Velocity model was selected for the theoretical HV curve and dispersion curve.

the shear wave velocity also increases with depth. Therefore, a regression model, which defines an increase in shear wave velocity with depth, has been assigned to represent the shear wave velocity (V_s) of a particular rock type concerning its depth of formation (z) as follows:

$$V_S = a.z + b \quad (1)$$

In the above expression, the depth (z) represents the shallowest depth of rock type in meters. After obtaining a reliable subsurface shear wave velocity model from MASW and HVSR survey a database of shear wave velocity of different rock types at different depths has been obtained, for the region

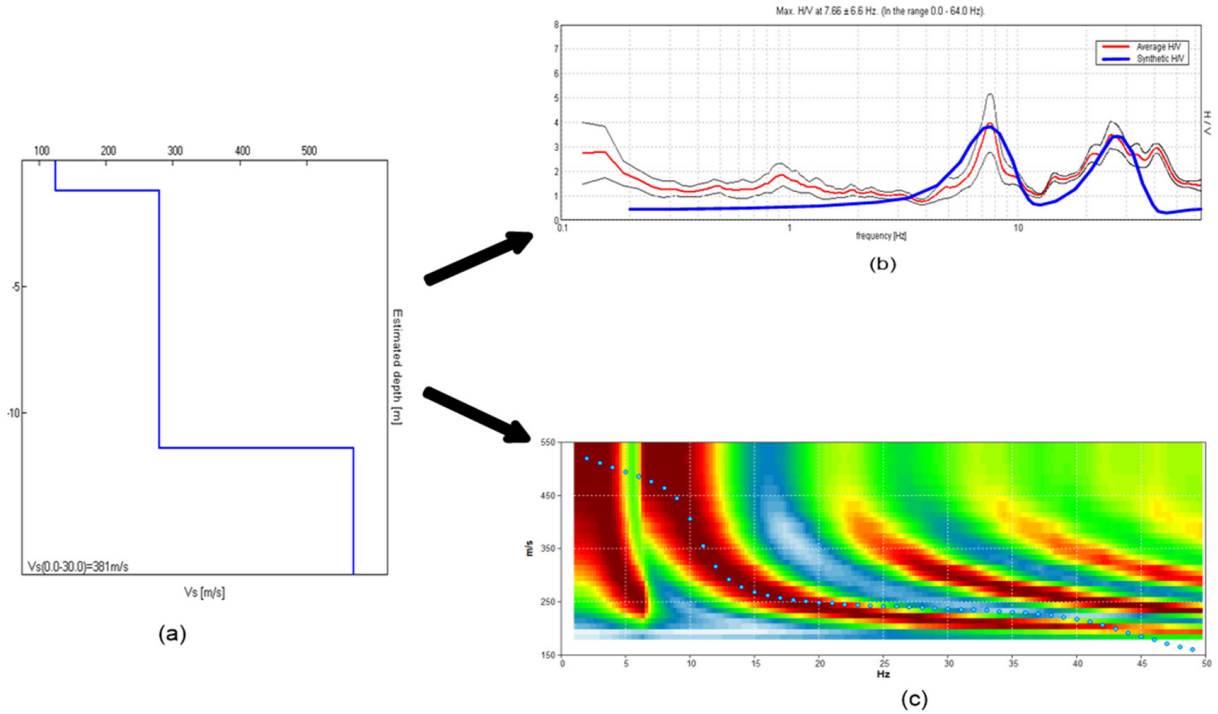

Figure 5. (a) Shear wave velocity profile at Kudiyala (b) Comparison of HV curve from field data and that from velocity model shown in (a) (c) Comparison of dispersion curve from MASW survey and that from velocity model shown in (a)

of Garhwal Himalayas. Linear regression relation for the model given in Equation (1) has been obtained by the least-square fit method. The best-fit line obtained for the different stratigraphic unit that follows the least square fit is shown in Figure 10. To check the efficacy of the developed relation following root mean square error (RMSE) between calculated and observed shear wave velocity has been calculated:

$$RMSE = \frac{\sqrt{\sum_{i=1}^{n}\left(V_{s,i} - V_{rel,i}\right)}}{n}$$

Here, $Vs_{,i}$ = Observed shear wave velocity from seismic survey

$V_{rel,i}$ = Shear wave velocity obtained from developed regression relation.

The regression model and obtained RMSE for each data set are given in Table 1. It is seen that RMSE obtained for different data sets varies from five to twenty-eight m/s, which is relatively small enough keeping in view of observed velocity of rock type.

Discussion

To test the reliability of values of shear wave velocity the regression relations developed for different rock type has been used to obtain shear wave velocity profile at those sites where lithological information is available. Two such sites have been used for this purpose. These two sites have not been included in the database used for developing regression relations. Shear wave velocity profile is obtained at these two sites using the developed regression relation given in Table 1. The lithologs

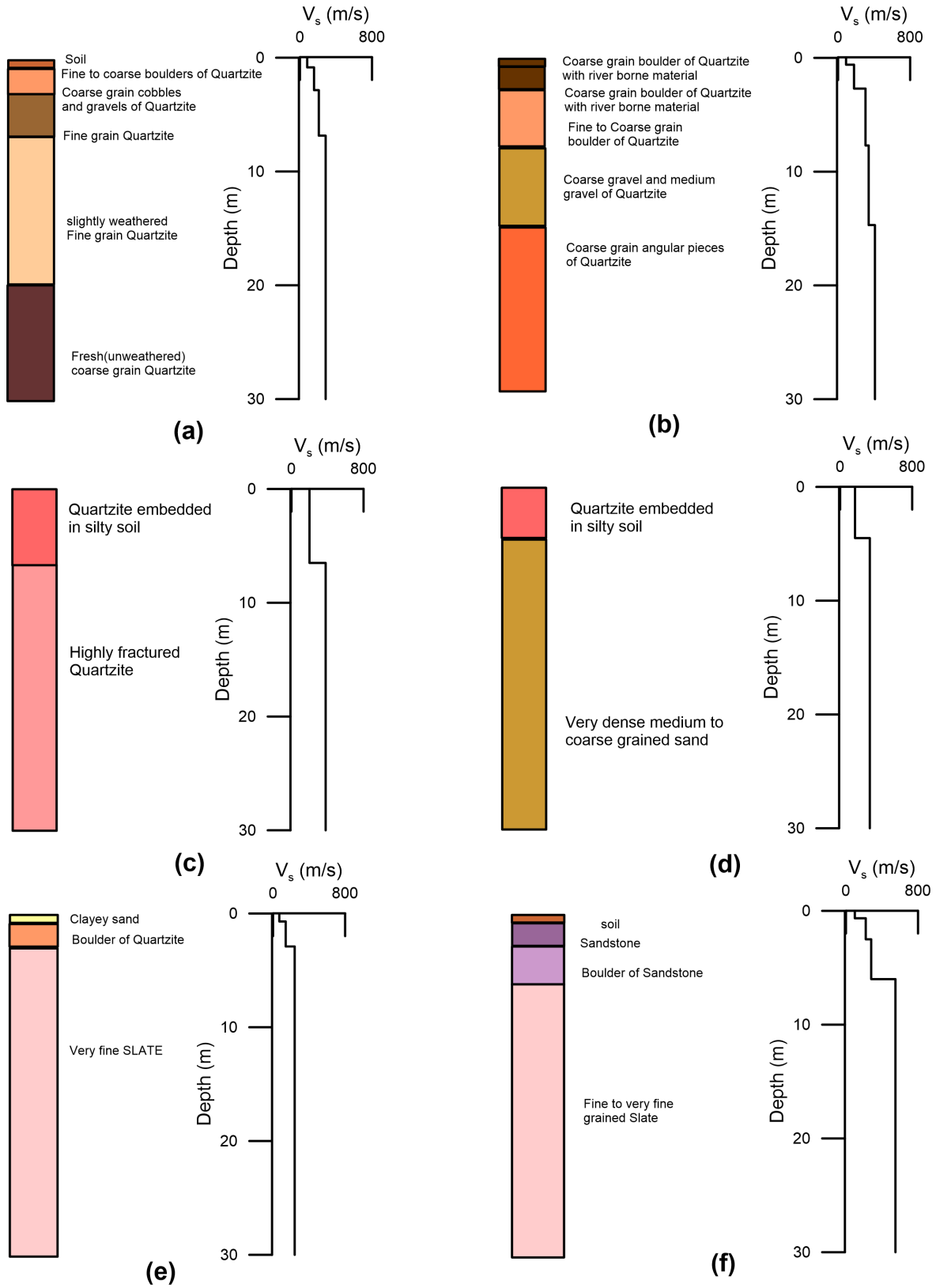

Figure 6. Shear wave profile and geological section from well log at (a) BH 31 (b) BH 32 (c) BH 46 (d) BH 47 (e) BH 51 (f) BH 52 sites, respectively

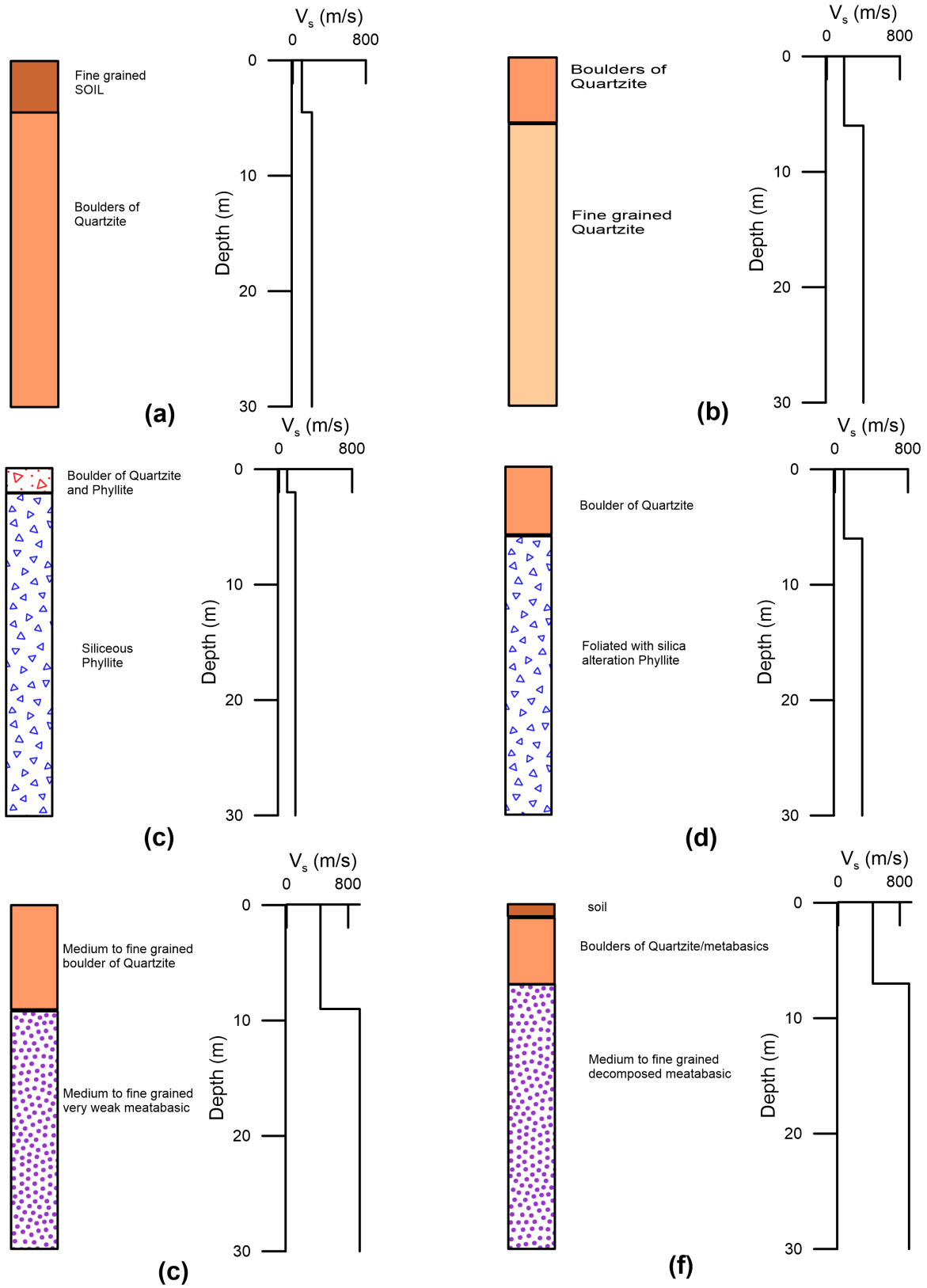

Figure 7. Shear wave profile and geological section from well log at (a) BH 57 (b) BH 58 (c) BH 59/1 (d) BH 59/2 (e) BH 78 (f) BH 79 sites, respectively

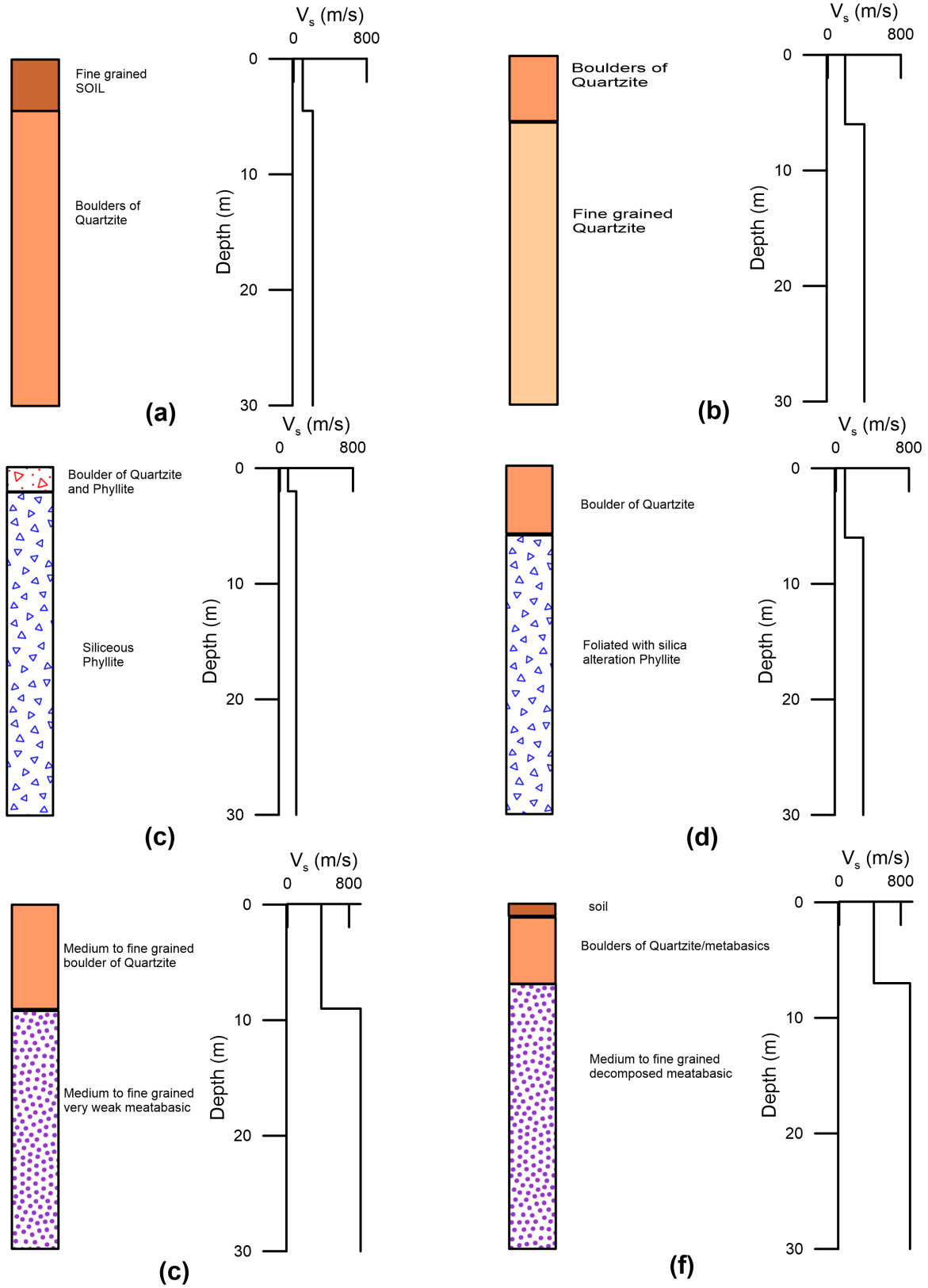

Figure 8. Shear wave profile and geological section from well log at (a) BH 108 (b) BH 109 (c) BH 114 (d) BH 115 (e) BH 117 (f) BH 118 sites, respectively

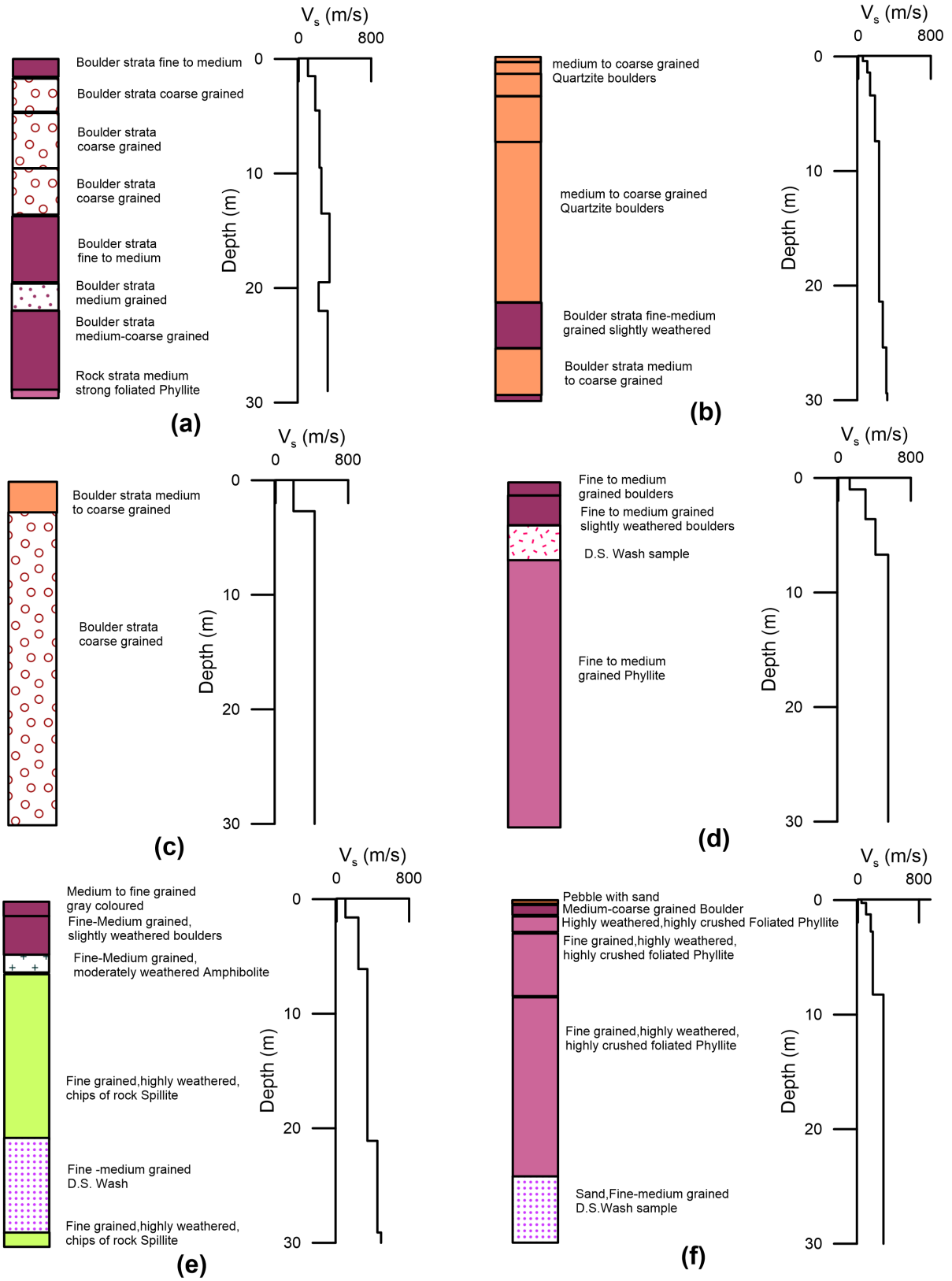

Figure 9. Shear wave profile and geological section from well log at (a) BH 139 (b) BH 141 (c) BH 157 (d) BH 158 (e) BH 166 (f) BH 167 sites, respectively

obtained from these sites using bore log data are shown in Figure 11. The lithologs at these sites have been used to compute the shear wave velocity of different rock-type in the lithologs. The shear wave velocity profile obtained from the developed regression relationship together with the lithology is shown in Figure 11.

In order to validate the shear wave velocity profile obtained at these two sites from regression relation, seismic data has been collected using MASW and HVSR surveys at these sites. The joint inversion of HVSR and dispersion curve obtained from seismic data at each of these two sites is shown in Figure 12. Shear wave velocity profile obtained from joint inversion of seismic data and that from developed regression relation for the lithological unit has been compared in Figure 13. Root mean square error between shear wave velocity profile obtained from joint inversion of seismic data and developed regression relation at these two locations is 29 and 11 m/s respectively, which validates the applicability of the developed regression relation in this area.

One of the important seismic parameters that are used for the classification of foundation sites is the average shear wave velocity at 30 m depth which is commonly known as V_{S30}. Site classification based on V_{S30} given by EUROCODE 8 is shown in Table 2. Table 2 shows the European site classification of Eurocode 8 which specifies the site type (A, B, C, D, E) according to the average shear wave velocities at 30 m depth.

The classification of sites BH 95 and BH 96 has been made based on V_{S30} obtained from both the regression relation and seismic survey. The estimate of V_{S30} from regression relation and seismic survey is given in Table 3. It is seen that V_{S30} obtained at these two sites from the seismic profile prepared using regression relation matches closely with that obtained from the seismic survey. The obtained V_{S30} at these stations from two different approaches classify these sites in Type C as per EUROCODE (CEN, 2004) classification. The comparison presented in Table 3 indicates that the developed regression relationship can be effectively used for the estimation of shear wave velocity profile and classification of rock in this part of Garhwal Himalaya.

Conclusions

In the present work, shear wave velocity structure has been estimated using both active and passive methods at a total of twenty-six sites in Garhwal Himalayas, India. In this work shear wave profiles from twenty-four sites have been used to prepare linear regression relation between shear wave velocities in different formations with respect to their depth of occurrence. In order to correctly identify various lithological units, lithologies from borehole data at each site have been used. Observed and calculated shear wave velocity from relation and seismic data is compared in terms of root mean square error. Root mean square error obtained for different lithological units varies from 5 to 28 m/s. In order to check the validity of regression relation two sites that have not been used for computing regression relation have been selected. Lithologs available at these sites are used for selecting regression relations of various lithological units. Shear wave velocity profile from joint inversion of H/V and MASW data at these sites is compared with that obtained from regression relation. Comparison of shear wave velocity profiles clearly shows that V_{S30} of shear wave velocity profile obtained from seismic experiment and regression relation falls in same EUROCODE 8 classification of the rock, thereby establishing the efficacy of developed relation in Garhwal Himalayas and thus is useful in contribution towards soil classification for zoning purposes and towards mitigation of region's seismic risk.

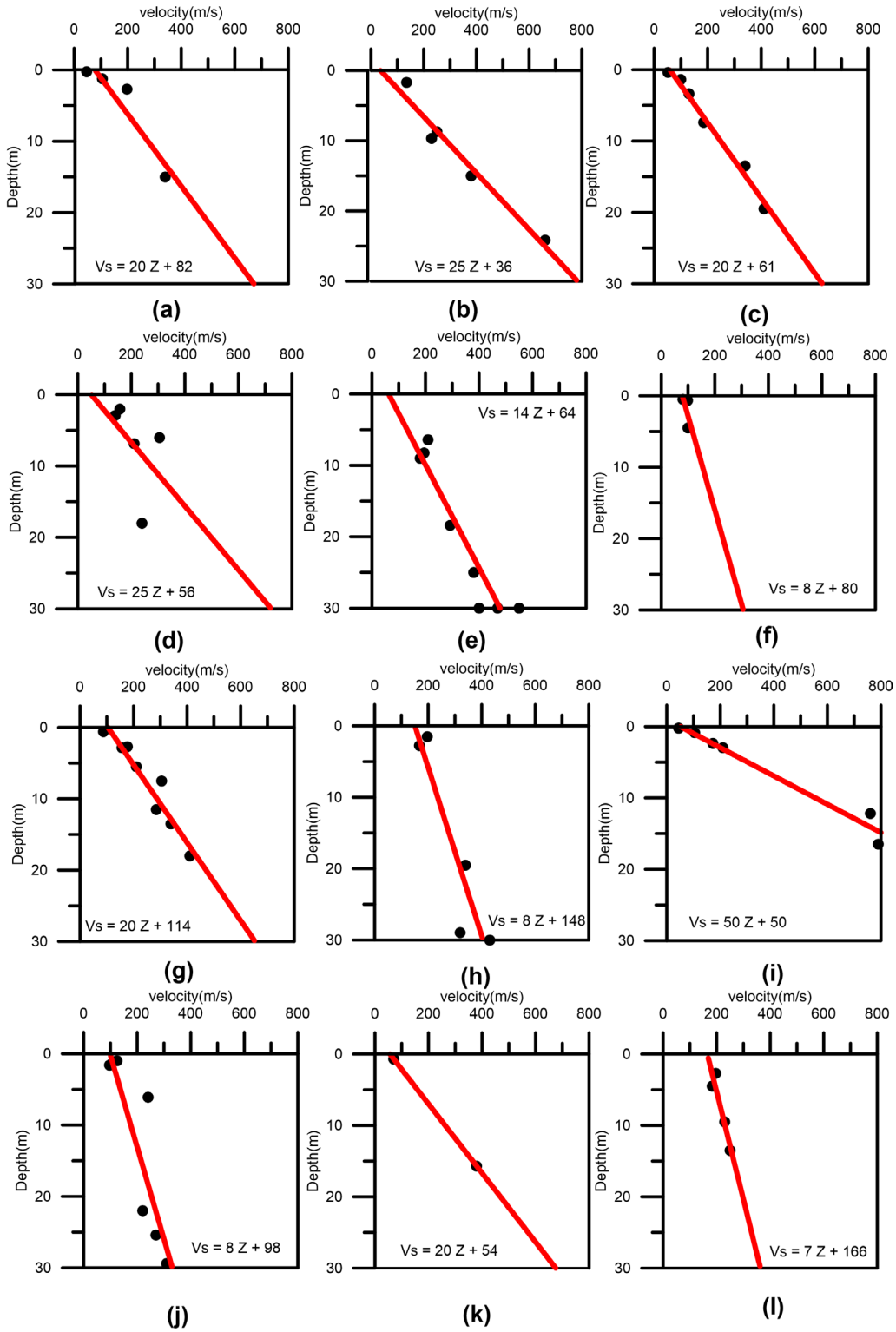

Figure 10. Shear wave velocity with respect to depth of different stratigraphic units. (a)Sand (b) Medium to the fine-grained boulder of quartzite (c) Medium to the coarse-grained boulder of quartzite (d) Fine to coarse-grained boulder of quartzite (e) Fine grained weak decomposed Phyllite (f) Fine grained soil (g) Coarse grained boulder of quartzite (h) Boulder strata medium to coarse grained (i) Medium grained sandstone (j) Fine to medium grained boulders (k) Clayey Sand (l) Boulder strata coarse grained, respectively

Table 1. Relation between shear wave velocity and depth for different lithological units in the Garhwal Himalayas within the depth of thirty meters

S. No.	LITHOLOGY	RELATIONS	RMSE (m/s)
1	Sand	V_S=20Z+82	21
2	Medium to fine grained boulder of quartzite	V_S=25Z+36	17
3	Medium to coarse grained boulder of quartzite	V_S=20Z+61	9
4	Fine to coarse grained boulder of quartzite	V_S=25Z+56	28
5	Fine grained weak decomposed phyllite	V_S=14Z+64	17
6	Fine grained soil	V_S=8Z+80	7
7	Coarse grained boulder of quartzite	V_S=20Z+114	14
8	Boulder strata medium to coarse grained	V_S=8Z+148	18
9	Medium grained sandstone	V_S=50Z+50	22
10	Fine to medium grained boulders	V_S=8Z+98	16
11	Clayey sand	V_S=20Z+54	6
12	Boulder strata coarse grained	V_S=7Z+166	5

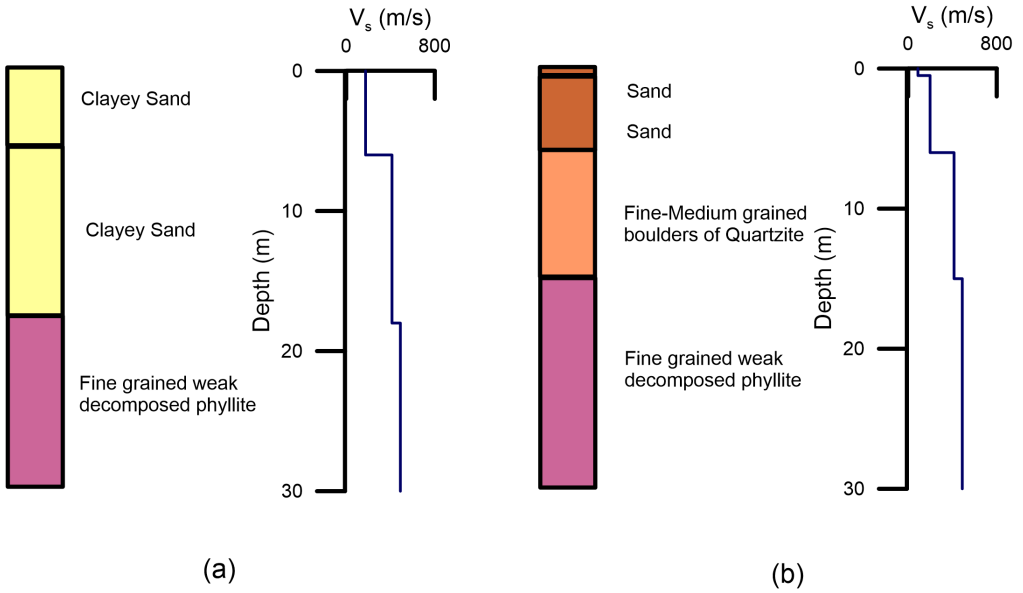

Figure 11. Shear wave velocity profile calculated from developed relation at (a) BH 95 (b) BH 96 site, respectively

Acknowledgements

We are very thankful to Rail Vikas Nigam Limited (RVNL), New Delhi, for their financial support and full cooperation during the data acquisition. We thankfully acknowledge DST-FIST grant No. SR/FST/ESII-018/2015(C) for providing instruments used in this research and the seismic data is acquired by self-installed TROMINO.

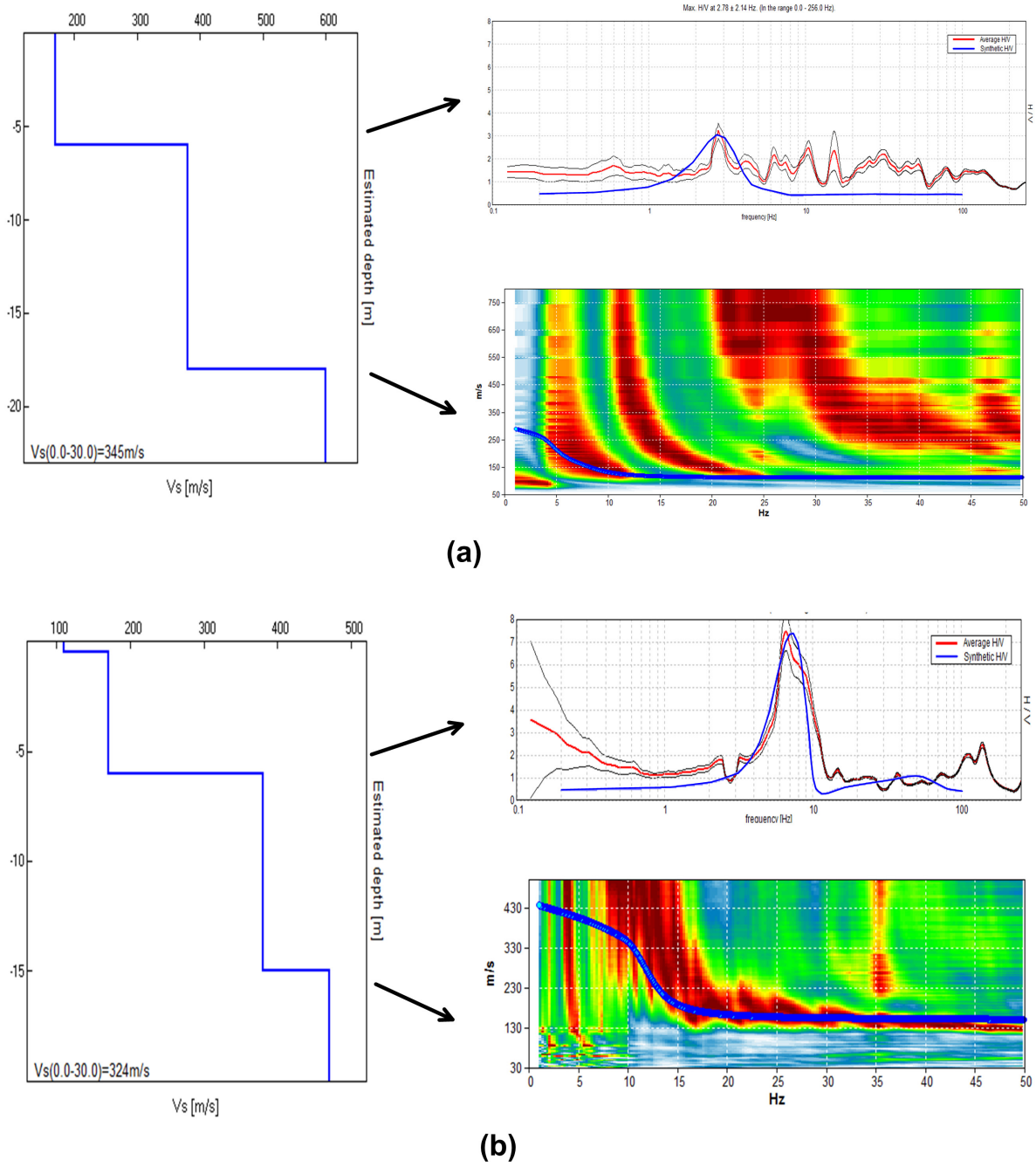

Figure 12. Joint fit of HVSR and MASW at (a) BH 95 (b) BH 96 sites, respectively

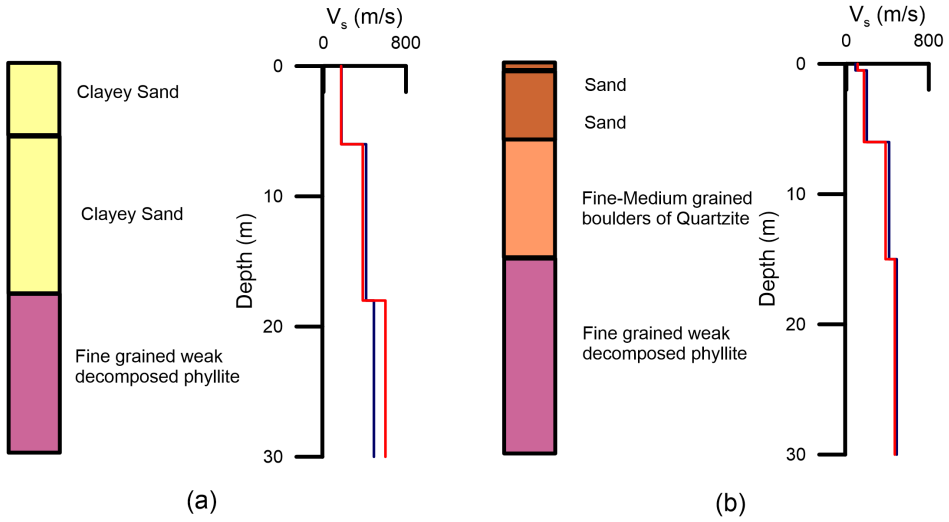

Figure 13. Comparison of shear wave velocity profile obtained from joint inversion of seismic data and that from developed regression relation for different lithologic units. In this figure blue line indicates the shear wave profile obtained from developed relation and the red that from joint inversion of seismic data, respectively

Table 2. European seismic code classes of Eurocode 8 (European committee for standardization [CEN,2004])

CLASS	EUROCODE 8
A	>800
B	360-800
C	180-360
D	<180
E	Surface alluvium layer with V_s values of type C or D and thickness b/w 5 and 20 m, underlain by stiffer material of V_s > 800 m/s.

Table 3. Comparison of VS30 value obtained from shear wave profiles from developed relation and that from joint inversion of seismic data, respectively

SITE	V_{S30} (m/s) obtained from joint inversion of seismic data	V_{S30} (m/s) obtained from developed relation	Diffe ence (m/s)
BH 95	345 (Type C)	341 (Type C)	4
BH 96	324 (Type C)	350 (Type C)	26

References

Abbiss, C.P., 1981. Shear wave measurements of the elasticity of the ground. *Geotechnique*, 31(1), pp.91-104.

Aki, K., 1957. Space and time spectra of stationary stochastic waves, with special reference to microtremors. *Bulletin of the Earthquake Research Institute*, 35, pp.415-456.

Asten, M.W., Lam, N.T.K., Srikanth, V., Rutter, H. and Wilson, J.L., 2005. The importance of shear wave velocity Information of a soil site. In *Proc. Conf. Australian Earthquake Eng Soc.*

ASTM, 1991(1995). Standard D4428/D4428M.Standard Test Methods for Crosshole Seismic Testing.

ASTM, 2007. Standard D7400. Standard Test Methods for Downhole Seismic Testing. ASTM International, USA.

Castellaro, S. and Mulargia, F., 2010. How far from a building does the ground-motion free-field start? The cases of three famous towers and a modern building. *Bulletin of the Seismological Society of America, 100*(5A), pp.2080-2094.

Castellaro, S., Padrón, L.A. and Mulargia, F., 2014. The different response of apparently identical structures: a far-field lesson from the Mirandola 20th May 2012 earthquake. *Bulletin of earthquake engineering, 12*(5), pp.2481-2493.

Castellaro, S., 2016. The complementarity of H/V and dispersion curves. *Geophysics*, 81(6), pp. T323-T338.

Castro, R.R., Mucciarelli, M., Pacor, F. and Petrungaro, C., 1997. S-wave site-response estimates using horizontal-to-vertical spectral ratios. *Bulletin of the Seismological Society of America*, 87(1), pp.256-260.

D'Amico, S., Akinci, A., Malagnini, L. and Galea, P., 2012. Prediction of High-Frequency Ground Motion Parameters Based on Weak Motion Data. *Earthquake Research and Analysis-New Frontiers in Seismology*, pp.69-86.

Eurocode, C.E.N., 2004. 8: Design of structures for earthquake resistance. Part, 1, pp.1998-1.

Fäh, D., Kind, F. and Giardini, D., 2001. A theoretical investigation of average H/V ratios. *Geophysical Journal International*, 145(2), pp.535-549.

Foti, S., Parolai, S., Bergamo, P., Di Giulio, G., Maraschini, M., Milana, G., Picozzi, M. and Puglia, R., 2011. Surface wave surveys for seismic site characterization of accelerometric stations in ITACA. *Bulletin of Earthquake Engineering*, 9(6), pp.1797-1820.

Gallipoli, M.R., Mucciarelli, M., Castro, R.R., Monachesi, G. and Contri, P., 2004. Structure, soil–structure response and effects of damage based on observations of horizontal-to-vertical spectral ratios of microtremors. *Soil Dynamics and Earthquake Engineering*, 24(6), pp.487-495.

Gorstein, M. and Ezersky, M., 2015. Combination of HVSR and MASW methods to obtain shear wave velocity model of subsurface in Israel. *International Journal of Georesources and Environment-IJGE (formerly Int'l J of Geohazards and Environment)*, 1(1), pp.1-1.

Jones, R., 1958. In-situ measurement of the dynamic properties of soil by vibration methods. *Geotechnique,* 8(1), pp.1-21.

Jones, R., 1962. Surface wave technique for measuring the elastic properties and thickness of roads: theoretical development. *British Journal of Applied Physics*, 13(1), p.21.

Khattri, K.N., Chander, R., Gaur, V.K. and Sarkar, I., 1989. New seismological results on the tectonics of the Garhwal Himalaya. *Proceedings of the Indian Academy of Sciences-Earth and Planetary Sciences*, 98(1), pp.91-109.

Kramer, S.L., 1996. *Geotechnical earthquake engineering*. Pearson Education India.

Lachetl, C. and Bard, P.Y., 1994. Numerical and theoretical investigations on the possibilities and limitations of Nakamura's technique. *Journal of Physics of the Earth*, 42(5), pp.377-397.

Lachet, C., Hatzfeld, D., Bard, P.Y., Theodulidis, N., Papaioannou, C. and Savvaidis, A., 1996. Site effects and microzonation in the city of Thessaloniki (Greece) comparison of different approaches. *Bulletin of the Seismological Society of America*, 86(6), pp.1692-1703.

Louie, J.N., 2007. Shear-wave velocity map for California: Collaborative Research with CGS, and UNR. *US Geol. Surv. Tech. Rept.* 07HQGR0029.

Lowrie, W., 2007. *Fundamentals of geophysics.* Cambridge university press.

Marina Gorstein and Michael Ezersky. 2015. Combination of HVSR and MASW Methods to Obtain Shear Wave Velocity Model of Subsurface in Israel. *International Journal of Geohazards and Environment.* 1(1): 20-41.

McMechan, G.A. and Yedlin, M.J., 1981. Analysis of dispersive waves by wave field transformation. *Geophysics*, 46(6), pp.869-874.

Mulargia, F. and Castellaro, S., 2013. A seismic passive imaging step beyond SPAC and ReMi. *Geophysics*, 78(5), pp.KS63-KS72.

Mulargia, F., Castellaro, S. and Vinco, G., 2015. Measuring shear wave velocity, Vs, of a hidden layer: An application to soil improvement under roads. *Canadian Geotechnical Journal*, 52(6), pp.721-731.

Nakamura, Y., 1989. A method for dynamic characteristics estimates of subsurface using microtremor on the round surface: Quarterly Report of the Railway Technical Research Institute, 30, 25–33.

Nazarian, S. and Stokoe, K.H., 1984. Nondestructive testing of pavements using surface waves. *Transportation Research Record*, 993, pp.67-79.

Nogoshi, M. and Igarashi, T., 1970. On the propagation characteristics of microtremors. *J. Seism. Soc. Japan*, 23, pp.264-280.

Ohori, M., Nobata, A. and Wakamatsu, K., 2002. A comparison of ESAC and FK methods of estimating phase velocity using arbitrarily shaped microtremor arrays. *Bulletin of the Seismological Society of America*, 92(6), pp.2323-2332.

Palmer, D., 1986. Refraction Seismics. The Lateral Resolution of Structure and Seismic Velocity. *Geophysical Press*, London-Amsterdam.

Park, C.B., Miller, R.D., Xia, J., Hunter, J.A. and Harris, J.B., 1999. Higher mode observation by the MASW method. In *SEG Technical Program Expanded Abstracts 1999* (pp. 524-527). Society of Exploration Geophysicists.

Park, C.B., R.D. Miller and J. Xia, 1999. Multichannel analysis of surface waves. *Geophysics*, 64(3): 800 - 808.

Parolai, S., Picozzi, M., Richwalski, S.M. and Milkereit, C., 2005. Joint inversion of phase velocity dispersion and H/V ratio curves from seismic noise recordings using a genetic algorithm, considering higher modes. *Geophysical research letters*, 32(1).

Picozzi, M., Parolai, S. and Richwalski, S.M., 2005. Joint inversion of H/V ratios and dispersion curves from seismic noise: Estimating the S-wave velocity of bedrock. *Geophysical Research Letters*, 32(11).

Rodriguez-Marek, A. Bray, J. D., and Abrahamson, N. 2000. A Geotechnical Seismic Site Response Evaluation Procedure. 12 *World Conference on Earthquake Engineering*.

Rošer, J. and Gosar, A., 2010. Determination of V_{S30} for seismic ground classification in the Ljubljana area, Slovenia. *Acta Geotechnica Slovenica*, 7(1), pp.60-76.

S. Sarkar, D. P. Kanungo and G.S. Mehrotra. 1995. Landslide Hazard Zonation: A case study in Garhwal Himalaya, India. *Mountain research and development*. Vol. 15 no. 4, 301-309.

Schmidt, R., 1986. Multiple emitter location and signal parameter estimation. *IEEE transactions on antennas and propagation*, 34(3), pp.276-280.

Socco, L.V. and C. Strobia, 2004. Surface-wave method for near-surface characterization: a tutorial. Near Surface *Geophysics*, 2: 165 -185.

Stokoe II, K.H., A. Kurtulus and K. Park, 2006.Development of field methods to evaluate the nonlinear shear and compression moduli of soil. Earthquake Geotechnical Engineering Workshop, Canterbury 2006 (EGE 2006), Christchurch, New Zealand, November 21 - 24, 2006.

Strobbia, C. and Foti, S., 2006. Multi-offset phase analysis of surface wave data (MOPA). *Journal of Applied Geophysics*, 59(4), pp.300-313.

Tsuboi, S., M. Saito and Y. Ishihara, 2001, Verification of horizontal-to-vertical spectral-ratio technique for estimation of site response using borehole seismographs, *Bull. Seismol. Soc. Am*. 91, 499-510.

Zor, E., Özalaybey, S., Karaaslan, A., Tapırdamaz, M.C., Özalaybey, S.Ç., Tarancıoğlu, A. and Erkan, B., 2010. Shear wave velocity structure of the Izmit Bay area (Turkey) estimated from active–passive array surface wave and single-station microtremor methods. *Geophysical Journal International*, 182(3), pp.1603-1618.

Original paper

https://doi.org/10.22201/igeof.00167169p.2022.61.3.2207

Gamma-ray spectrometry applied in the identification of potential acid mine drainage generation zones in waste rock pile with uranium ore and associated sulfides (Caldas, Brazil)

Anna Carolina Gastmaier Marques[1*], César Augusto Moreira[1], Matheus Felipe Stanfoca Casagrande[1], Erika Juliana Aldana Arcila[2]

Received: January 11, 2022; accepted: April 18, 2022; published on-line: July 1, 2022.

Resumen

La minería de metales modifica profundamente la dinámica ambiental local y produce grandes volúmenes de roca y residuos, los cuales se espera sean eliminados cuidadosamente para evitar el deterioro del suelo, el agua y el medio ambiente. La mina Osamu Utsumi fue un sitio de explotación de mineral de uranio pionero en Brasil, ubicado en el estado de Minas Gerais. La mina abierta y la alta concentración de sulfuro en las capas de material estéril son hoy en día un tema de preocupación para las Industrias Nucleares de Brasil (INB), debido a la oxidación del sulfuro y el drenaje ácido de la mina resultante (AMD, por sus siglas en inglés). El objetivo de esta investigación es analizar los datos de espectrometría de rayos gamma y la generación de AMD en una capa de material estéril, BF-04, en el sitio. La adquisición de datos radiométricos combinada con estudios previos indica que las altas concentraciones de uranio y torio están asociadas con zonas de alto contenido de sulfuro. El mineral de uranio mineralizado incluye sulfuros que se destruyen rápidamente por las condiciones de hidratación de la superficie y son responsables de generar el drenaje ácido de la mina. En este sentido, las zonas superficiales de la capa de material estéril con altos niveles de eU y eTh son áreas expuestas a la oxidación e hidratación de sulfuros y, por lo tanto, su reconocimiento y neutralización pueden contribuir a disminuir la generación de AMD en el sitio de estudio y áreas con condiciones similares. Los resultados de la espectrometría de rayos gamma pueden ser de interés para una remediación de bajo costo en el entorno local.

Palabras clave: minería, contaminación, aguas subterráneas, geofísica, medio ambiente y radiactividad.

Abstract

Metal mining deeply modifies local environmental dynamics and produces large volumes of waste rock and residues, which is expected to be carefully disposed in order to prevent soil, water, and environment degradation. The Osamu Utsumi mine was a pioneer uranium ore exploitation site in Brazil, located in the State of Minas Gerais. The open pit and the high concentration of sulfide

Editorial responsibility: María de Nuria Segovia Aguilar

**Corresponding author at anna.gastmaier@gmail.com*

[1*] *São Paulo State University (Universidade Estadual Paulista), Department of Geology, Av. 24A, 1515, CEP: 13506-900, Rio Claro (SP), Brazil.*

[2] *Catholic University of Manizales (Universidade Católica de Manizales), Departament of Engineering and Architecture, Carrera 23 N0. 60-63, CEP: 170002 , Manizales (Caldas), Colombia.*

in waste rock piles are nowadays a dispendious concern to the Nuclear Industries of Brazil (INB, in Portuguese), due to sulfide oxidation and the resultant acid mine drainage (AMD). The objective of this research is to analyze the correlation between gamma-ray spectrometry data and the generation of AMD in a waste rock pile, locally known as BF-04. Potassium concentrations can be used to distinguish zones of rock depletion, lowest concentrations, and radioelement sedimentation. The radiometric data acquisition combined with previous studies indicates that high uranium and thorium concentrations are associated with high sulfide zones. The mineralized uranium ore includes sulfides that are rapidly destroyed by surface hydration conditions, responsible for generating acid mine drainage. In this sense, superficial zones in the waste rock pile with high levels of eU and eTh are areas exposed to oxidation and hydration of sulfides, and, therefore, their recognition and neutralization can contribute to decrease AMD generation in the study site and areas with similar characteristics. The gamma-ray spectrometry results can subsidize more effective and low-cost remediation techniques.

Key words: mining, pollution, groundwater, geophysics, environment and radioactivity.

Introduction

The mining and metals sector has major importance for regional and local socioeconomic development, in addition to its influence on global economy in terms of mineral supply and energy resources. Consequently, the most varied waste and environmental liabilities generated by such activity demand a proper management for the benefit of environmental integrity and local communities (Gilmore, 2008; Jain, Cui and Domen, 2016).

The Brazilian Mining Institute (IBRAM) indicates that mineral substances correspond to 14.5% of the country total exportation, represents 52% of exportation trade balance and points to the participation of the mineral extractive sector in 3.7% of Brazil's Gross Domestic Product (GDP) (IBRAM, 2019).

Although approximately only one third of its territory was prospected, Brazil possesses the world's sixth largest uranium ore reserves, which amounts approximately 310,000 t of triuranium octoxide (U_3O_8), recoverable at low cost (Brazil, 2017). All processes concerning uranium and other radioactive elements, such as mining, are national monopoly activities. The Nuclear Industries of Brazil are nowadays regulated by the National Nuclear Energy Commission and the Brazilian Institute of Environment and Renewable Natural Resources, CNEN and IBAMA respectively in Portuguese. Despite of CNEN establishment in 1956, IBAMA was only founded in 1989.

Social and environmental impacts of mining must be an integral part of all mine planning and mineral development from the discovery phase through to closure process, regarding the complexity that involves the mined ore. Physically landscape disturbance is a result of mining, including waste rock and tailings disposal areas and facility development. Operations and waste products associated with metal extraction and processing are one of the main causes of environmental concerns about metal mining, which may increase the acidity of soils and consequent degradation of both surface and groundwater quality, as well as increase air-borne dust and other emissions (Hudson, Fox and Plumlee, 1999).

The exposure of natural reactive minerals to superficial environmental conditions can trigger key processes for the generation of highly complex contaminants. Studied across the globe, metal sulfide

minerals are present in host rock associated with most types of metal mining activity. In the presence of moisture and atmospheric oxygen, sulfide minerals are oxidized and generates acid mine drainage (AMD). Although the oxidation of these minerals and the formation of sulfuric acid is a function of natural weathering processes, mining activity, such as extraction and beneficiation operations, increase the chemical reactions by exposing large volumes of sulfide rock material with increased surface area. Among others, pyrite, arsenopyrite, chalcopyrite and chalcocite oxidation can occur for several years following mine closure (USEPA, 1994; Akcil and Koldas, 2006).

Followed by the generation of AMD, secondary factors act to either neutralize the acid produced by oxidation of sulfides or may change the effluent character by adding metals ions mobilized by residual acid. The generation of AMD and the potential to release contaminants are dependent on many factors, including specific characteristics found at different locations, such as climate and physical properties of the waste material. In the geological environment, the occurrence of radioelements associated with sulfide rocks under chemically reducing conditions create an environment where uranium and thorium exist in a tetravalent state, a configuration relatively insoluble. However, under oxidizing conditions uranium occurs in hexavalent uranyl ion (UO_2^{2+}), soluble in water and mobilized by AMD (USEPA, 1994; Dentith and Mudge, 2014).

The radiometric method measures naturally occurring radioactivity in the form of gamma-rays, most originated from mineral species containing radioactive isotopes of potassium, uranium and thorium (^{40}K, ^{238}U, ^{235}U, and ^{232}Th). This study consists in the recognition of shallow mineralized reliquary zones in a waste rock pile of Osamu Utsumi mine, through the geophysical method of gamma-ray spectrometry, allowing its correlation with AMD generation and the radionuclides mobilization. In addition, the comprehension of the superficial drainage infiltration in the waste rock pile and the recognition of main zones of radioactive response will allow the establishment of a suitable management plan to the study area.

Materials and Methods

Study site

In 1982, uranium ore exploration began in Brazil with Poços de Caldas Industrial Mining Complex (CIPC) with a 15 km^2 facility in the municipality of Caldas, Minas Gerais State. The CIPC is considered the first installation for uranium ore mining, processing and chemical treatment in the country, based on the exploration of the Osamu Utsumi mine (OUM). In 1995, after producing 1,030 tons of uranium, which corresponds to 24% of the dimensioned potential,OUM was closed due to economic unfeasibility and the decommissioning activity persists until nowadays (Cipriani, 2002). The environment impacts mitigation is a huge dispendious challenge and concern to INB, once the decommissioning plan includes the inactive open pit mine, ore treatment unit, waste rock piles and tailings dam.

The study site is in one of CIPC's waste rock piles known as BF-04, which is characterized by a predominantly flat area bounded to the north by the by-pass channel of Consulta creek and to the south by the slopes of the upper level of the waste rock pile (Figure 1).

Despite of INB efforts to bypass the Consulta Creek and to dispose a layer of clay as a waterproof barrier, it was necessary to build a catchment basin, the BNF, at the base of BF-04 slope to prevent the contamination of the River Verde hydrographic basin (Casagrande, 2019)

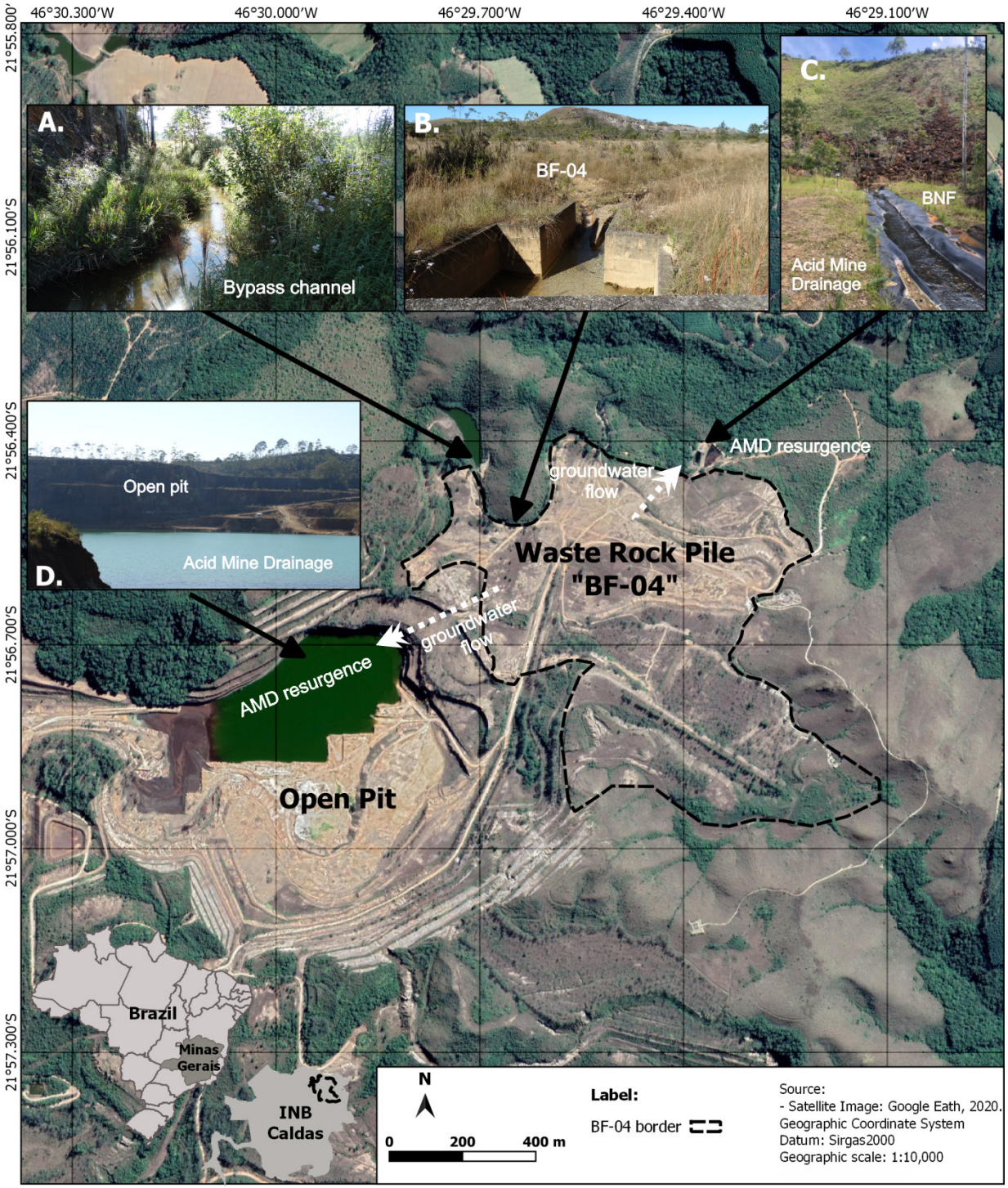

Figure 1. Osamu Utsumi mine location in the INB, Caldas (MG), and delimitation of BF-04 waste-rock pile (A) Bypass channel of Consulta Creek; (B) surface water drainage channel from BF-04 to the Consulta Creek; (C) Nestor Figueiredo Basin (BNF) – catchment of waters affected by acid mine drainage.

The Poços de Caldas Plateau is characterized by its relatively high altitude, which varies from 1300 m to 1600 m, and the tropical climate with two well-defined seasons. The average rainfall index is 1700 mm/year, having the period between October and March as the months with highest levels of precipitation and milder temperatures are registered, whereas the period from April to September is characterized by strong drought and low temperatures. Rustic grasses form the landscape along with small arboreal patches in the high fields and shrubs along the slopes (Holmes *et al.*, 1992; Cipriani, 2002).

Uranium Deposit Genesis and Waste Rock Pile BF-04 composition

The Alkaline Complex of Poços de Caldas initially suffered regional postmagmatic deuteric and incipient hydrothermal alteration, when occurred potassium metasomatism and zeolitization, with minor argillation under oxidizing conditions and no mobilization/concentration of uranium, thorium or rare earth elements (REEs) (Schorscher and Shea, 1992). In the OUM, mineralized rocks were modified by hydrothermal fluid/rock interaction of local extent, the primary mineralizing event, which led to pyritization, strong potassic metasomatism and to the formation of several radioactive anomalies. Along with subsequent evolutive stages, low-temperature processes formed descending redox fronts associated with supergene uranium remobilization and precipitation (Schorsche and Shea, 1992; Biondi, 2015).

Three different types of ore were explored in the OUM, named "A", or fluidization breccia, "B" and "E". With about 60% of uranium reserves, mineralized zone "B" was formed by the hydrothermal alteration in breccias, phonolite and tinguaites lavas. The minerals uraninite, zircon and molybdenum are associated with clay minerals including kaolinite, pyrite and minerals remaining from hydrothermal rocks (Magno Júnior, 1985; Biondi, 2015).

Waste materials from the stripping phase and screening from ore were disposed in the Consulta's creek and Cercado's creek valleys without previous waterproofing, forming the waste rock piles BF-04 and BF-08, respectively. BF-04, the focus of this study, has an area of 56.9 hectares and volume of 12,400,000 m^3, with waste rock from stripping and screening from ore "B". After the beginning of OUM operations, one by-pass channel for the Consulta Creek was built with no appropriate waterproof structure (Amaral *et al.*, 1988; Fernandes *et al.*, 1995; Cipriani, 2002; Nóbrega, Lima and Leite, 2008).

BF-04 was built according to the end-dumping method and disposed on the top of a fractured aquifer system. Local potassic rocks, clay and blocks provided by uranium explorations composes the waste rock pile, the main mineralogical composition consists of K-feldspar (50%), Kaolinite (20%), Muscovite (20%) and Pirite (2%), between others (Franklin, 2007; Casagrande *et al.*, 2020).

Even though BF-04 configures an artificial structure, the material works as a phreatic aquifer, vulnerable to local climate conditions. In addition, it is notable the evidence of particles segregation along the pile caused by the construction method based on gravitational process. Thus, the presence of compacted layers and fine-grain material accumulation tend to create saturated zones, once hydraulic conductivity is proportional to the average grain size of the material that composes the hydrogeological system (Casagrande *et al.*, 2020). The waste rock pile structure allows water infiltration and storage at the base of the pile, improving sulfide and water interaction due to high hydraulic conductivity generated by the accumulation of large particles. This context comprises a good environment for DAM formation and spreading (Nóbrega, Lima and Leite, 2008).

Groundwater historical chemical analysis collected in the open pit and in the AMD resurgence shows K-Fe-SO^4 as chemical components, acid pH and saline effluents (Table 1). Iron and sulfate high concentrations associated with acid effluents collected in subsurface wells indicates pyrite oxidation by meteoric water. AMD is responsible for mineral leaching, such as fluorite and uraninite, that explains fluorine, iron, uranium and sulfate in the groundwater. Zinc associated with fluorite and low pH are related with sphalerite oxidation associated with mineralized ore combined with pyrite. Divergent sulfate concentrations in underground flow are correlated with a complex patter of AMD generation in sulfide mineralized zones (Nordstorm *et al.*, 1992; Campos *et al.*, 2011).

Table 1. Groundwater chemical analysis

	Open Pit		AMD resurgence
Parameter	**Nordstrom *et al.* (1992)**	**Campos *et al.* (2011)**	**Campos *et al.* (2011)**
pH	3,37/3,29(3)	3,37 ± 0,40	3,47 ± 0,11
E_h (mV)	627	525,10 ± 53,39	466,98 ± 18,55
K (mg/L)	37,7	...	...
Fe(II) (mg/L)	50,5	0,25 ± 0,24	1,89 ± 3,74
Fe (total) (mg/L)	53,5	5,18 ± 3,55	1,43 ± 0,91
Al (mg/L)	98	...	...
Mn (mg/L)	46	88,42 ± 16,31	89,63 ± 34,23
Zn (mg/L)	12,8	12,65 ± 4,78	14,47 ± 6,73
SO_4 (mg/L)	1200	1410 ± 241,87 6035,17	778,68 ± 661,91
F (mg/L)	14,9	25,73 ±7,55	33,60 ± 19,50
U	-	4,02 ± 1,97	8,11 ± 4,24
Th	-	0,19 ± 0,07	0,19 ± 0,13

Gamma-ray spectrometry

Gamma-ray spectrometry is a radiometric geophysical passive method which quantifies occurrence of radioactivity through emission of gamma rays of several naturally occurring or artificial radionuclides. Among the group of natural occurrences are those of cosmogenic origin (^{14}C, ^{3}H, ^{36}Cl, etc.) and the ones associated to the geological environment (^{40}K, ^{235}U, ^{238}U, e ^{232}Th), both groups widely known by the acronym NORM (Naturally Occurring Radioactive Materials).

Spectrometry has a distinctive advantage which is the capacity to provide information about the geochemical nature of the radioactive source (Dentith and Mudge, 2014). Spectrometers are sensible to the energies of the radioelements of geological interest, once it can be chosen K, U and Th energy windows to detect energetic ɣ-rays emitted from relevant elements in parts of the energy spectrum where emissions from other elements are weak or rare.

Important in several areas in Geosciences as petrology, hydrochemistry and environment geology (Dentith and Mudge, 2014; Gilmore, 2008; Milson, 2003), ^{235}U, ^{238}U, e ^{232}Th are the first terms of long decay chains, developing several radionuclides until a stable isotope of Pb. On the opposite direction, ^{40}K decays directly to one of his two stable isotopes: ^{40}Ca and ^{40}Ar, this last one through electronic capture with emission of associated gamma-ray of 1461 keV (Chu *et al.*, 1999).

The use of photopics generated by daughter nuclides is a very common approach in gamma-ray spectrometry to determinate the respective primordial parent radionuclide. Thus, the photopeaks of

1765 keV (^{214}Bi) and 2615 keV (^{208}Tl) accounted to estimate concentrations of U and Th, respectively (Erdi-Krausz *et al.*, 2003). When measurement infers indirectly the concentration of the parent, by relating the emission products from daughter element, the concentration of the ɣ-emitting element must be in proportion to the concentration of its radioactive source, meaning the decay series must be in equilibrium (Dentith and Mudge, 2014).

The method can be used through portable or airbone detection systems or profiling probes (Telford, 1990; Ferronsky, 2015). Regarding portable systems, gamma-ray spectrometry, internal memories can store a large quantity of data acquired, which are generally restricted to measurements in the K, U and Th energy windows, and the total (Dentith and Mudge, 2014). Nevertheless, it has some limitations associated with the equipment and environmental conditions: spectral of the detection crystal (scintillometer), topographical irregularities, soil moisture and soil/rock density (Musset and Khan, 2000; Milson, 2003; Beamish, 2015). Thereby, depth of acquisition is an important factor for both planning and analysis procedures because, according to Taylor *et al.* (2002), approximately 90% of gamma rays observed on surface are generated only in the superficial 30 cm depth in a relatively dry soil of 1.6 g/cm^3.

Gamma-ray spectrometry presents a high applicability in determination of environmental gamma radiation levels, especially for its potential correlation with anthropogenic contamination sources (Dentith and Mudge, 2014; Gilmore, 2008).

Data acquisition and processing

Geophysical acquisition was performed through 281 individual points covering the BF-04 most affected area. The system used was the portable RS-332 Multipurpose Gamma-Ray Spectormeter System from Radiation Solutions INC, presenting high sensibility, thermic protection, easy handling, internal GPS, and a collimator associated to the BGO crystal. This equipment enables registration of energetic intermissions from 30 keV to 3,000 keV, an appropriate energy interval for the recognition of daughters radionuclides of series of ^{232}Th, ^{238}U, and the decay of ^{40}K. Finally, the system automatically converts the unit counting-per-second (cps) in concentrations expressed in parts per million (ppm) for U e Th and percentage (%) for K. The generated data for uranium and thorium are given by the term "equivalent" (eU and eTh) due to indirect estimates base on daughter radionuclides (IAEA, 2003).

The portable RS-332 Multipurpose Gamma-Ray Spectormeter enables gamma acquisition time sets in 120, 180, 240 and 300 seconds. This is a very relevant factor because it is inversely proportional to the associated reading error (Hendriks *et al.*, 2001) and, according to Løvborg and Mose (1987), in situ gamma acquisitions have used reading periods varying from 1 to 20 minutes. Comparatively, Nardy et al (2014) defined a reading time of 60 seconds for acquisitions also using a bismuth germanate (BGO) scintillometer detector, applied in the analysis of gamma-ray signature in volcanic rocks of Paraná Basin.

With the purpose to understand the correlation of different acquisition times and the variance of measured concentration by a portable gamma-ray spectrometer, four experimental data acquisition in the same spot in the study area were collected. Standard deviation and the coefficient of variation were calculated to be determined the optimal time of data acquisition. Results of coefficient of variation were 1.59% for K and Th, 0.92% for U and 0.56% for dose rate. Minimal variations,

such as the measured, permitted the time sets in 120 seconds without changing the consistency and representativeness of the data.

Approximately 28.16 ha of the BF-04 were screened by the individual gamma-ray readings, which were made in direct contact with the surface of the waste rock exposed, without any vegetal cover or soil. The acquisition was concentrated on the average altitude of 1378 m, comprising many portions of BF-04, such as the margins of the Consulta Creek, north border and central region of the waste rock pile. Collecting points were disposed approximately along parallel lines according to NE-SW direction, with average spacing of 30 m (Figure 2).

After acquisition of radiometric data, a processing procedure was performed for generation of maps that reflect radiometric distribution and signature of BF-04 regarding eU, eTh and K.

The 281 collected data points were submitted to an interpolation routine at Oasis Montai platform (Geosoft) in order to generate a bidimensional section of thorium, potassium and uranium concentration values in terms of distance. Due to natural mitigation of gamma rays and receptor capability to recognize energy emitted next to surface, the radiometric data were not deeply processed.

Interpolation is represented through data mitigation from mathematical method of least squares approximation and mitigates de differences of values calculated by the software and values measured on field. Software's routine consists of automatic creation of a theoretical bidimensional model through division of subsurface in rectangular blocks. Distribution and size of the blocks are automatically created by the program, through distribution of de data points as approximated guidance (Targa, 2020 apud Loke, 2003). Concentrations are calculated by the program from blocks' model were comparison between measured and patterned values is made. Parameters of the blocks are interactively adjusted until calculated apparent value is accordant to values measured on field.

After processing, maps with color-scale or grey-scale are created, representing quantitative contents of elements K (in %), eU and eTh (both in ppm) (Ulbrich *et al*., 2007). With the processed geophysical data, maps for analysis of radioisotopes are individually prepared.

Results and discussion

The interpretation of radiometric data presumes that anomalous concentrations of one or more radioelements may potentially indicate mineralizing environments (Dentith and Mudge, 2014). However, the possibility of disequilibrium must be a primary consideration. Inferred amount of eU, or eTh concentrations may be too high or too low when disequilibrium occurs, depending on the removal or accumulation of the mobile component of the relevant decay series, and, through the solubility of Ra and mobility of Rn, which can produce ^{214}Bi in locations remote from the parent ^{238}U. The disequilibrium for uranium exploration is most likely to occur on groundwater discharge areas, reducing environments such swamps and situations with increased porosity by physical weathering (Dentith and Mudge, 2014 apud Levinson and Coetzee 1978). Nevertheless, the structure of waste rock pile of the Osamu Utsumi mine allows infiltration and storage at the base of the pile, due to its construction method based on gravitational process (Casagrande *et al.*, 2020). For this reason, the environmental complexity of the BF-04's superficial recharging zone is entirely distinct from areas where radiometric disequilibrium occurs.

Geophysical data interpolation allows the acknowledgement of radiometric anomalies on the BF-04 surface. The radioelements uranium, thorium and potassium mobility were described, as well as the radiometric characteristics of the waste rock pile BF-04 from the Osamu Utsumi mine.

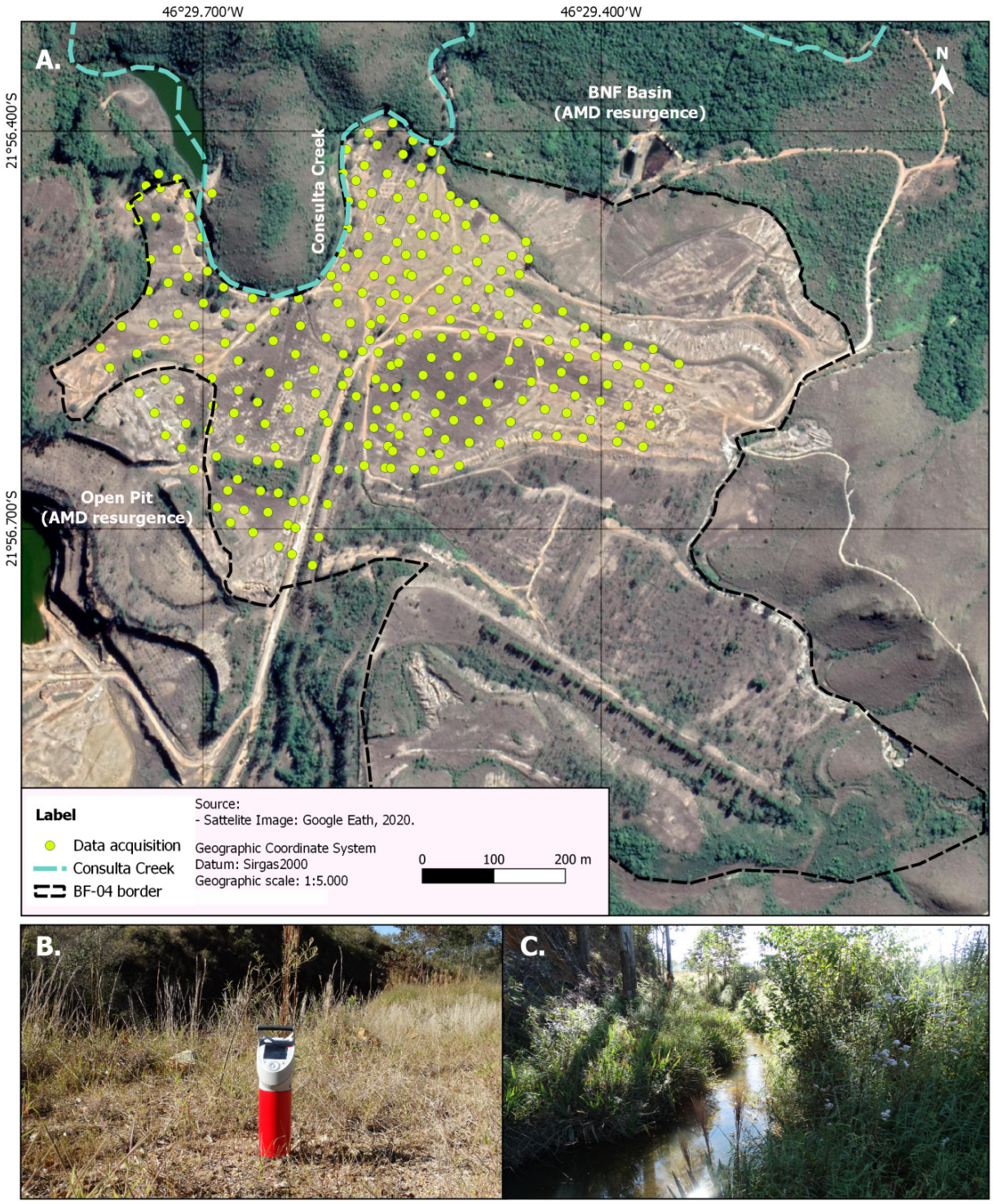

Figure 2. Disposal of geophysical acquisition along the lower level of BF-04. (A) Data acquisition points; (B) RS-332 Multipurpose Gamma-Ray Spectrometer System (Radiation Solutions INC); (C) Consulta Creek.

In distinct environment conditions, potassium has a high mobility and geochemistry solubility. In tropical and subtropical climate zones the decomposition of many potassium minerals due to weathering can be clearly observed (Dentith and Mudge, 2014). The elevated annual pluviosity at Poços de Caldas plateau is the main responsible factor for weathering processes, mainly in superficial and exposed potassic rocks, as identified in the BF-04.

Regarding potassium radiometric response, high concentrations can be associated with the following factors: unchanged potassic rocks, potassium precipitation in wetlands and/or adsorption by clay minerals. On the other hand, low concentrations suggest depletion and element mobility due to weathering (Dentith and Mudge, 2014).

Potassium anomaly zones (Figure 3) are observed in north and southeast areas of BF-04, with values between 5.68% and 13.39% (warm colors), while in the central portion is characterized by lower concentrations varying between 1.002% and 4.72% (cold colors).

The most important processes associated with uranium and thorium decay are removal, transport, and sedimentation. Uranium (U^{6+}) mobilization occurs in weathering environments and its solubi-

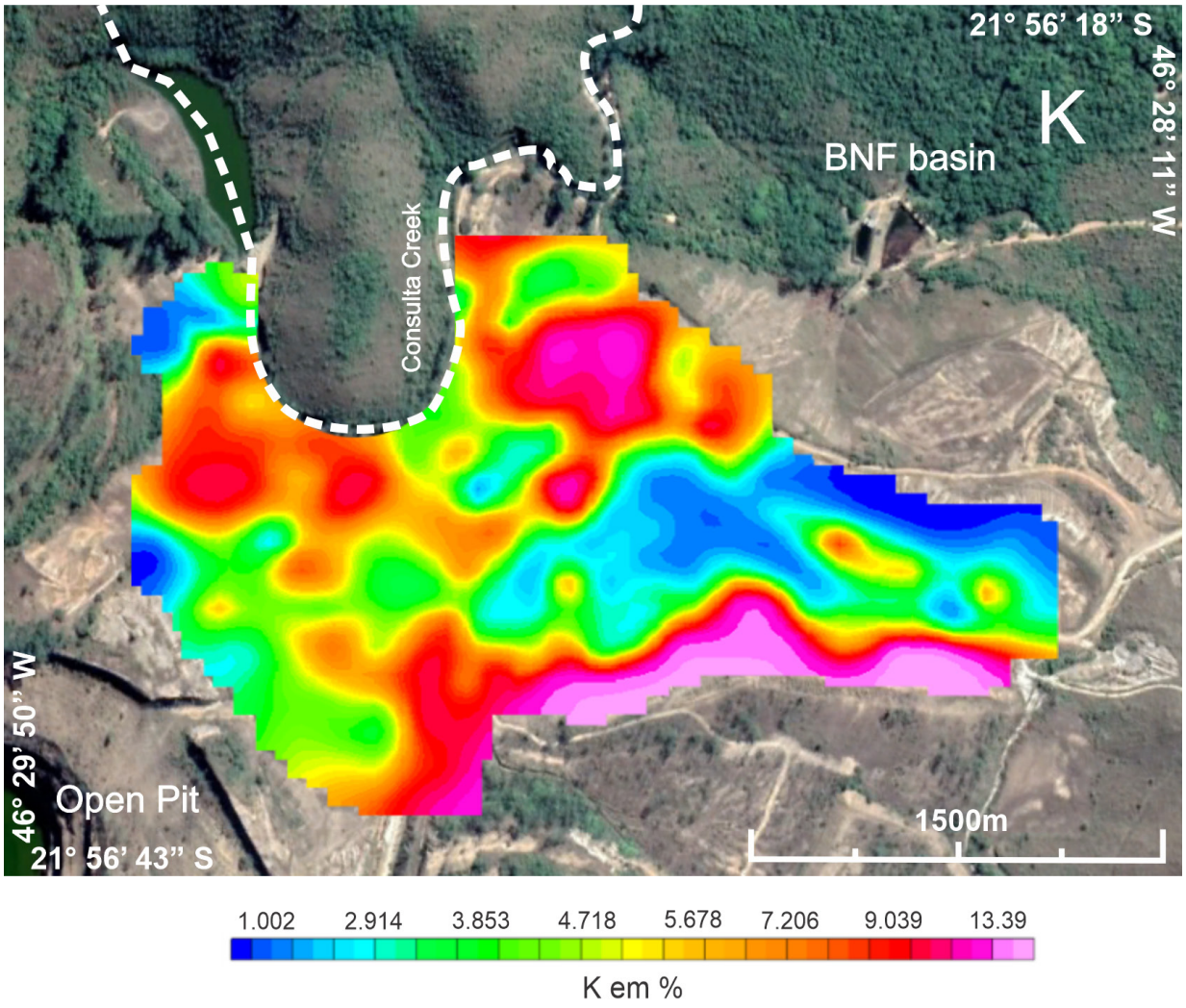

Figure 3. 2D interpolation map of potassium concentration over BF-04.

lization is intensified in oxidizing environments due to the formation of the hexavalent uranyl ion (UO_2^{2+}) (Dentith and Mudge, 2014). The main differences between uranium and thorium radioelements mobilization comprise the uranium leaching capacity and thorium detention on organic and inorganic pedogenic substances.

Figure 4 presents a 2D interpolation map of eU and Figure 5 shows the same product for eTh. It is possible to observe similar results in the potassium distribution map, where the highest concentrations of eU and eTh can be found in north and southeast, with eU ranging from 87.76 ppm to 312.61 ppm and eTh between 113.90 ppm and 221.14 ppm.

Casagrande *et al.* (2020) performed a geophysical investigation through DC resistivity measurements for the same study site, recognizing underground saline flows associated with AMD. Those results were compared to high chargeability anomalies generated by induced polarization method (IP method), that were considered as sulfides accumulation associated with resistive minerals from the rock basement, given its proximity to the open pit area, and, consequently, to reliquary mineralized bodies. The acknowledge of oxidized and reduced zones associated with the generation of acid

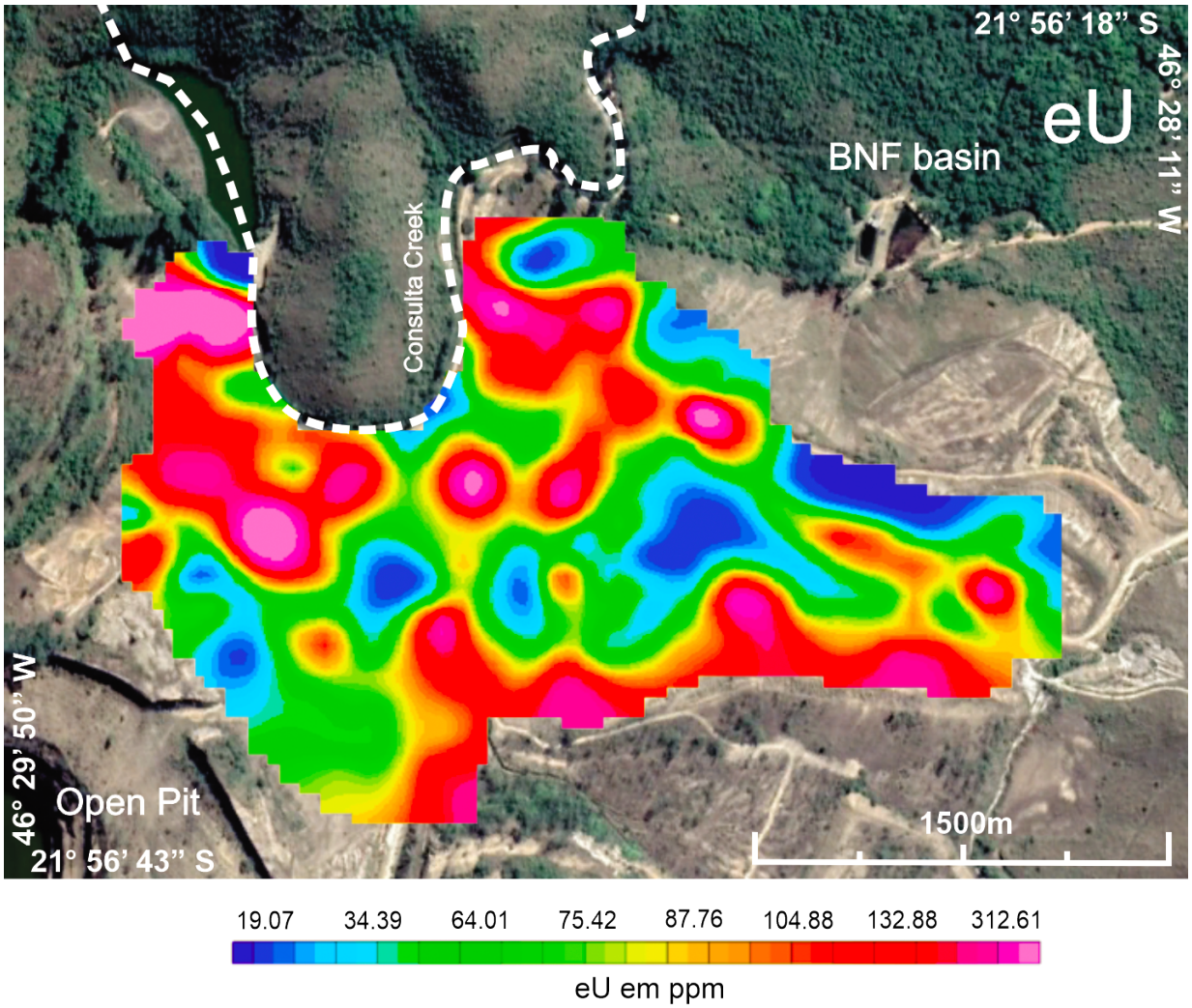

Figure 4. 2D interpolation map of uranium concentration over BF-04.

drainage due to pyrite oxidation were also correlated with previous hydrochemical analysis which present radionuclides and solubilized metals.

Nascimento *et al.* (2022) presents water infiltration from non-impermeable by-pass channel of the Consulta creek as one of the main key processes that generate AMD in the waste rock pile BF-04, due to chemical interaction between water and sulfide minerals. High concentrations of uranium next to the channel is recognized in this study, making possible the assumption of high uranium radioactivity, due to oxidizing zone, as a radioactive marker of acid drainage.

Figure 6 presents the by-pass channel of the Consulta creek, the most probable responsible for water infiltration in the waste rock pile BF-04 and the generation of acid mine drainage in the north region of the BF-04, with a remnant sulfide rock testimony correlated to a high uranium anomaly.

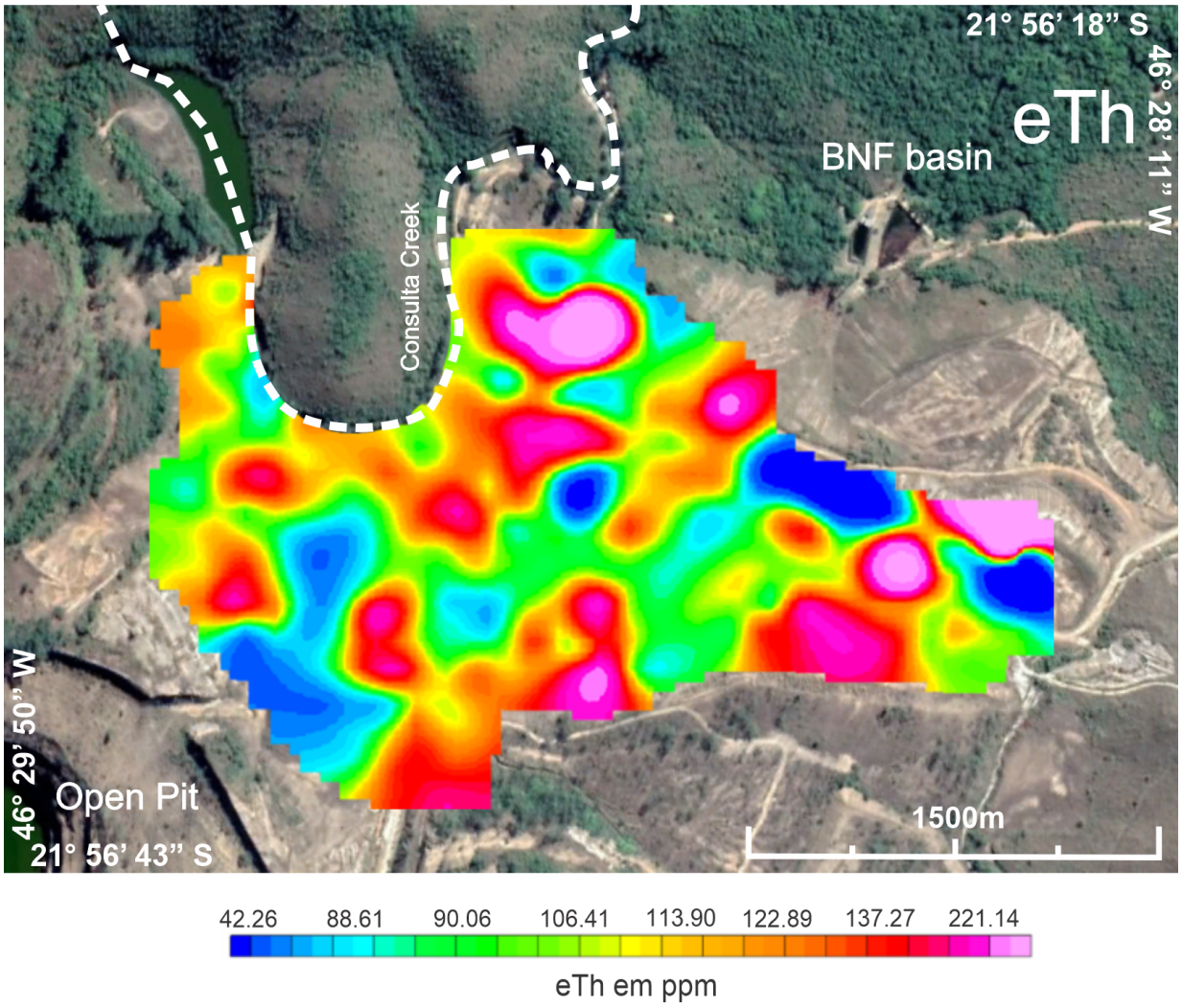

Figure 5. 2D interpolation map of potassium concentration over BF-04.

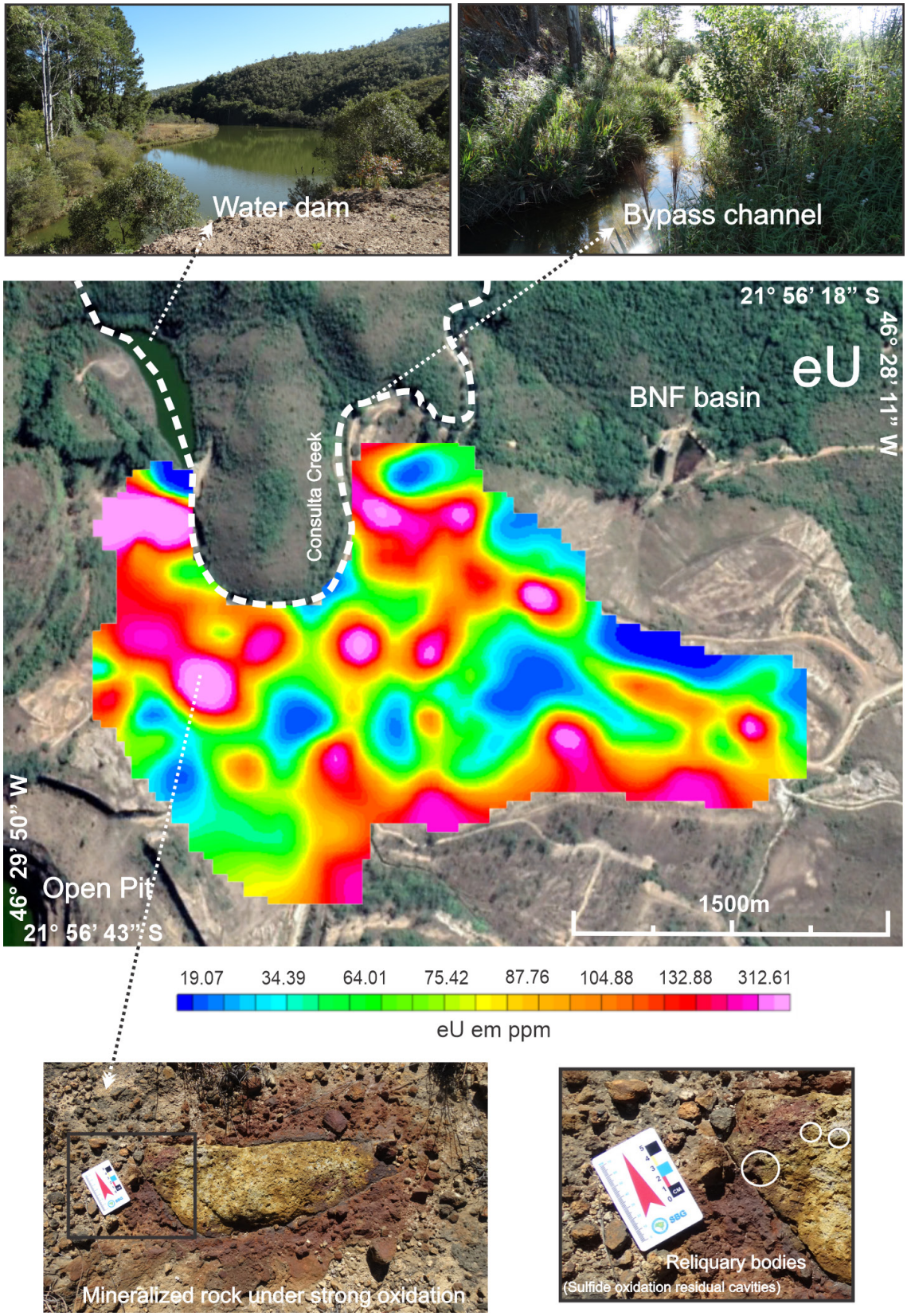

Figure 6. By-pass channel of the Consulta creek associated with the generation of AMD and high uranium concentration.

Conclusions

The loss of biodiversity and natural resources, soil and water contamination, socio-environmental impacts are some of the results of unplanned mining installation and operation. Regarding contamination, AMD associated with mobilized metals and radioelements comprises a specific long-term environmental impact with high technical complexity. Gamma-ray spectrometry, a passive and local investigation, proved to be a relevant contributor for studies of planning and remediation of degraded areas.

Geophysical investigations have an elevated potential for application in environmental studies, so that the radiometric results provided a very useful shallow analysis of contamination caused by AMD in a waste rock pile. The recognition of anomalies characterized by high concentrations of radioactive elements in parallel to sulfide-rich zones and acid drainage generation provided a better understanding and characterization of BF-04.

The mineralized uranium ore includes sulfides that are rapidly destroyed by surface hydration conditions and are responsible for generating acid mine drainage. In this sense, superficial zones in the waste rock pile with high levels of eU and eTh are areas exposed to oxidation and hydration of sulfides, and, therefore, their recognition and neutralization can contribute to decrease AMD generation in the study site and areas with similar characteristics, even indirectly by gamma-ray spectrometry.

The results obtained can be used as support for decisions involving the applicability of in situ remediation solutions with focus to prevent the generation and continuity of contaminated groundwater flows. Correlated to the generation of acid mine drainage by chemical action of surface drainage with sulfide zones, waterproofing actions on the BF-04 surface and installation of an efficient rainwater drainage system are deeply recommended.

Another critical necessity is a waterproof system along Consulta creek channel in order to extinguish or diminish the water infiltration into the waste rock pile. Those combined actions should significantly reduce the generation of AMD captured in the BNF, once the source of water is controlled.

This study complements a series of geophysical investigations that demonstrate the versatility of passive methods in the acknowledgement of environmental impact complexity, in addition to support the planning of sustainable remediation and decommissioning actions in the mining project studied, serving as a model for similar areas.

Acknowledgments

This work was funded by the FAPESP - Fundação de Amparo à Pesquisa do Estado de São Paulo (Process n° 2020/03207-9 – "Sustainable decommissioning: analysis of hydrogeological behavior in rock massifs and their influence on geotechnical stability in open pit mine slopes and acid mine drainage generation"). We also would like to thank National Council for Scientific and Technological Development (Conselho Nacional de Desenvolvimento Científico e Tecnológico) for the financial support and the Brazilian Nuclear Industries (Indústrias Nucleares do Brasil-INB) for the provided access to the study site.

References

Akcil, A., Koldas, S. Acid Mine Drainage (Amd): Causes, Treatment And Case Studies. Journal Of Cleaner Production, V. 14, N. 12, P.1139-1145, 2006.

Amaral, E.c.s., Godoy, J.m., Rochedo, E.r.r., Vasconcellos, L.m.h., Pires Do Rio Ma (1988) The Environmental Impact Of The Uranium Industry: Is The Waste Rock A Significant Contributor? Radiat Prot Dosim 22:165–171.

Beamish, D. (2015). Relationships Between Gamma-Ray Attenuation And Soils In Sw England. Geoderma 259–260 (2015) 174–186

Biondi, J. C. Processos Metalogenéticos E Os Depósitos Minerais Brasileiros. 2ª Edição Revisada E Atualizada. Oficina De Textos. São Paulo. 552p. 2015

Brasil, 2017. National Report Of Brazil 2017. For The 6th Review Meeting Of Joint Convention On The Saety Of Spent Fuel Management And On The Safety Of Radioactive Waste Management. República Federativa Do Brasil. Available In: Https://Www.iaea.org/Sites/Default/Files/National_report_of_brazil_for_the_6th_review_meeting_-_English.pdf. Access In July 2021.

Campos, M. B.; Azevedo, H.; Nascimento, M. R. L.; Roque, C. V.; Rodgher, S. Environmental Assessment Of Water From A Uranium Mine (Caldas, Minas Gerais State, Brazil)In A Decomissioning Operation. Environmental EarTH SCIENCE (2011) 62:857-863. DOI 10.1007/S12665-010-0572-9.

CASAGRANDE, M.F.S., MOREIRA, C.A., TARGA, D.A. Study Of Generation And Underground Flow Of Acid Mine Drainage In Waste Rock Pile In An Uranium Mine Using Electrical Resistivity Tomography- Pure And Applied Geophysics, 2020.

Chu, S.y.f., Ekström, L.p., Firestone, R.b. 1999. The Lund/Lbnl Nuclear Data Search. (Http://Nucleardata.nuclear.lu.se/Nucleardata/Toi/Index.asp).

Cipriani, M. Mitigação Dos Impactos Sociais E Ambientais Decorrentes Do Fechamento Definitivo De Minas De Urânio. 2002, 332 P. Tese De Doutorado - Universidade Estadual De Campinas - Instituto De Geociências, Campinas, 2002.

Dentith, M.; Mudge, S.t. Geophysics For Th*e Mineral Exploration Geoscientist*. 2014. 438 P. Cambridge University Press.

Erdi-Krausz G, Matolin M, Minty B, Nicolet Jp, Reford Ws, Schetselaar Em. Guidelines For Radioelement Mapping Using Gamma-Ray Spectrometry Data: Also *As Open Access E-Book. Internation*al Atomic Energy Agency (Iaea). 2003.

Fernandes, H.m., Veiga L.h.s., Franklin, M.r., Prado, V.c.s., Taddei, J.f. (1995). Environmental Impact Assessment Of Uranium Mining And Milling Facilities: A Study Case At The Poços De Caldas Uranium Mining And Milling Site, Brazil. J Geochem Explor 52:161–173

Ferronsky, V I. Nuclear Geophysics: Applications In Hydrology, Hydrogeology, Engineering Geology, Agriculture And Environmental Science. Springer, Moscow. 2015.

Franklin, M. R. (2007). Modelagem Numérica Do Escoamento Hidrológico E Dos Processos Geoquímicos Aplicados À Previsão Da Drenagem Ácida Em Uma Pilha De Estéril Da Mina De Urânio De Poços De Caldas, Mg. Ph.d. Thesis, Universidade Federal Do Rio De Janeiro, Rio De Janeiro, P. 358.

Gilmore, G. R. Practical Gamma-Ray Spectrometry. 2008. 2º Edição. 387 P. John Wiley & Sons Ltda.

Hendriks, P.h.g.m., Limburg, J., Meijer., R.j. (2201). Full-Spectrum Analysis Of Natural G -Ray Spectra. Journal Of Environmental Radioactivity 53 (2001) 365±380

Holmes, D. C.; Pitty, A. E.; Noy, D. J. Geomorphological And Hydrogeological Features Of The Poços De Caldas Caldera And The Osamu Utsumi Mine And Morro Do Ferro

Hudson, T. L.; Fox, F. D.; Plumlee, G.s. Metal Mining And The Environment. Agi Environmental Awareness Series, 3. American Geological Institute. Virginia (Eua). 63 P. 1999.

Instituto BrasIleiro De Mineração (Ibram). 2019. Relatório Anual De Atividades. Janeiro A Dezembro De 2019.

International Atomic Energy Agency (Iaea). Guidelines For Radioelement Mapping Using Gamma Ray Spectrometry Data. 2003. 172p. Viena, AUSTRIA.

Jain, K. R.; Cui, Z.c.; DOMEN, J. K. Environmental Impact Of Mining And Mineral Processing. Management, Monitoring, And Auditing Strategies. Elsevier. Oxford, Reino Unido. 309p. 2016.

Løvborg, L. And Mose, E. (1987), "Counting Statistics In Radioelement Assaying With A Portable Spectrometer," Geophysics 52: 555-563.

Magno Júnior, L. B. Osamu Utsumi Mine, Geologic Presentation. In: Relatório Interno Nuclebrás. Rio De Janeiro, Rj, 1985.

Mussett, A. E.; Khan, M. A. (2000) Looking Into The Earth: An Introduction To Geological Geophysics. Nova Iorque: Cambridge University Press, 470 P.

Nardy, A.j.r, Moreira, C.a., Machado, F.b, Luchetti, A.c.f., Hansen, M.a.f., Rossini, A.r., Barbosa Jr, V. 2014. Gamma-Ray Spectrometry Signature Of Paraná Volcanic Rocks: Preliminary Results. São Paulo, Unesp, Geociências, V. 33, N. 2, P.216-227, 2014

Nordstorm, D. K.; Mcnutt, R.; Puigdomenech, I.; Smellie, J. A. T.; Wolf, M. Groundwater Chemistry And Geochemical Modeling Of Water-Rock Interactions At The Osamu Utsumi Mine And The Morro Do Ferro. Journal Of Geochemical Exploration. V. 45. 249-287p. 1992.

Nóbrega, F.a.; Lima, H.m.; Leite, A.l. Análise De Múltiplas Variáveis No Fechamento De Mina - Estudo De Caso Da Pilha De Estéril Bf-4, Mina Osamu Utsumi, Inb Caldas, Minas Gerais. Ouro Preto, Revista Escola De Minas, V. 61, N. 2, P. 197-202, 2008.

Schorscher, H. D.; Shea, *M. E. The Region*al Geology Of The Poços De Caldas Alkaline Complex: Mineralogy And Geochemistry Of Selected Nepheline Syenites And Phonolites. Journal Of Geochemical Exploration. V. 45. 25-51 P. Elsevier Science Publishers B.v., Amsterdam. 1992.

Taylor, M.j., Smettem, K., Pracilio, G. Verboom, W. Relationships Between Soil Properties And Highresolution Radiometrics, Central Eastern Wheatbelt, Western Australia. Exploration Geophysics, 33, 95–102. 2002.

Telford, W.m., Geldart, L.p. And Sheriff, R.e. (199*0) Resistivity Methods. In: Applied Geophy*sics, 2nd Edition, Cambridge Univ. Press, Cambridge, Uk, 353-358.

United States Environmental Protection Agency (Usepa). Abandoned Mine Site Characterization And Cleanup Handbook. 2000. 129p. Seattle, Wa, Eua.

United States Environmental Protection Agency (Usepa). Technical Document. Acid Mine Drainage Prediction. 1994. 48p. Washington, Dc, Eua.